applied mechanics

MDPI

Article

Modeling and Simulation of the Aging Behavior of a Zinc Die Casting Alloy

Maria Angeles Martinez Page and Stefan Hartmann *

Institute of Applied Mechanics, Clausthal University of Technology, 38678 Clausthal-Zellerfeld, Germany
* Correspondence: stefan.hartmann@tu-clausthal.de

Abstract: While zinc die-casting alloy Zamak is widely used in vehicles and machines, its solidified state has yet to be thoroughly investigated experimentally or mathematically modeled. The material behavior is characterized by temperature and rate sensitivity, aging, and long-term influences under external loads. Thus, we model the thermo-mechanical behavior of Zamak in the solid state for a temperature range from −40 °C to 85 °C, and the aging state up to one year. The finite strain thermo-viscoplasticity model is derived from an extensive experimental campaign. This campaign involved tension, compression, and torsion tests at various temperatures and aging states. Furthermore, the thermo-physical properties of temperature- and aging-dependent heat capacity and heat conductivity are considered. One significant challenge is related to the multiplicative decompositions of the deformation gradient, which affects strain and stress measures relative to different intermediate configurations. The entire model is implemented into an implicit finite element program and validation examples at more complex parts are provided so that the predicability for complex parts is available, which has not been possible so far. Validation experiments using digital image correlation confirm the accuracy of the thermo-mechanically consistent constitutive equations for complex geometrical shapes. Moroever, validation measures are introduced and applied for a complex geometrical shape of a zinc die casting specimen. This provides a measure of the deformation state for complex components under real operating conditions.

Keywords: zinc die casting alloy; thermo-viscoplasticity; aging; material modeling; finite strains

check for updates

Citation: Martinez Page, M.A.; Hartmann, S. Modeling and Simulation of the Aging Behavior of a Zinc Die Casting Alloy. *Appl. Mech.* **2024**, *5*, 646–695. https://doi.org/10.3390/applmech5040037

Received: 24 July 2024
Revised: 16 September 2024
Accepted: 23 September 2024
Published: 30 September 2024

Copyright: © 2024 by the authors. Licensee MDPI, Basel, Switzerland. This article is an open access article distributed under the terms and conditions of the Creative Commons Attribution (CC BY) license (https://creativecommons.org/licenses/by/4.0/).

1. Introduction

Zinc die casting alloys are commonly used in the production of components of cars and machines, as well as in the electronic, construction, and appliance industries, see [1,2]. They show an excellent castability along with low production costs. Their suitability for the hot chamber die casting process comes from their low melting point. However, the material implies three main disadvantages: a strong viscoplastic behavior in the temperature range of applications (for the automotive industry this lies approximately between −40 °C and 85 °C), a temperature-dependent mechanical response, see [3] and a change in the thermo-mechanical behavior due to aging of the material, see [4]. This has to be considered in the design process requiring a suitable model.

In comparison to other materials such as steel or aluminum alloys, zinc die casting alloys have not been sufficiently investigated so far. One can find several investigations from the point of view of Material Science, in which the microstructure is characterized for different zinc die casting alloys under different thermal conditions. The microstructural changes of zinc-aluminum alloys became subject of investigations in the last century. Refs. [5–7] characterized the micro-structure, phase transformations, and volume changes of the zinc-aluminum and zinc-aluminum-copper alloys over time. Moreover, the reduction of dimensions (shrinkage) in zinc die casting alloys over the course of time is described in [8]. Murray [9] investigated the equilibrium phase diagram of zinc-aluminum alloys as well as their different crystal structures. In [10] the analyses of the influence of the alloying

elements on the mechanical properties, studies focusing on other aspects such as the creep behavior, aging, the consequent volume changes, as well as inter-crystalline corrosion can be found. Although in the nineties, the interest in zinc die casting alloys reduced, new investigations in this field started to appear in the past years. At the beginning of the 21st century, phase transformations and precipitation of several Zn-Al alloys were extensively characterized in [11–16]. Leis and Kallien [2] show the characterization of the influence of temperature, natural, and artificial aging, the thickness-dependence of the specimen, and die casting conditions on several mechanical parameters such as the Young's modulus, yield strength, or tensile strength. Further characterizations of the effect of alloying components on the microstructure, phase decomposition, or mechanical characterizations in zinc die casting alloys can be found in the works of Jareño et al. [17], Liu et al. [18], Savaskan and Pasa Hekimoglu [19], Pola et al. [20], and Wu et al. [21].

There are very few proposals for modeling the mechanical behavior of zinc die casting alloys in the literature. Some of them consider the die casting process itself, see [22,23], or investigations from the point of view of Material Sciences, see [2,13–24]. A wide amount of models have been proposed for aluminum alloys and steel. One can find several proposals for other alloys, such as titanium, magnesium, nickel or copper alloys, see [25–29]. Most of these alloys are exposed to some kind of mechanical treatment before they are modeled or their behavior differs strongly from zinc alloys. Finally, from the author's side, a model of thermo-viscoplasticity for small deformations of Zamak 5 is proposed in [3], which was extended to natural aging at room temperature in [4]. Moreover, in [30], the thickness dependence was modeled considering the porosity for a purely elastic material behavior.

One major issue of this work is the modeling of aging effects in zinc die casting alloys and its extension to large strains. This provides a new prediction tool that—for the first time—makes it possible to predict the thermomechanical behavior of a zinc die cast material at different aging states.

In the field of theory of materials in a continuum mechanical framework, Krempl [31] defines aging as a modification of the micro-structure, in such a way that the same loading process, performed in the same environment at different times (or ages of the material), will lead to different mechanical responses. The origin of these modifications lies in the microstructure of the material. The cause of aging is different for polymers and alloys. Chaboche [32] distinguishes three different types of aging in alloys: *Dynamic strain aging* is caused by "dragging" of the dislocations of the atoms in solution and is associated with the "Portevin-Le Chatelier effect". *Static strain aging* implies a growth in material strength with time, which is observed as a reverse effect of static recovery. In the literature, there are several suggestions on how to model these two kinds of aging types in aluminum alloys and steel, but in the present study of Zamak, none of these types of aging was observed. Finally, *aging due to phase changes* is a consequence of dissolutions, precipitations, and phase transformations in alloys, which fits with the observations made in [33]. In the case of polymers, aging is related to physical and chemical changes, which limits their application period, see [34]. From a macroscopic point of view, the effect of aging can be introduced into the model with an internal variable, see [35,36] and in the area of polymers see [34,37–40]. In the literature one can find several proposals for modeling aging. Marquis and Lemaitre [35] proposed a model coupling elasto-plasticity, damage and aging for small deformations. Additionally, a model for plasticity and aging is suggested in Marquis and Costa Mattos [41]. In these models, the effect of aging is included with a new internal variable. In [42], chemical aging is included in a model for adhesive bonds in a polymer using an additional field variable to describe the diffusive processes. Moreover, in [38], a model for small deformations with aging as an internal variable is developed. In [34,37,39], a chemo-thermomechanical and a chemical aging model for elastomers for small deformations is suggested, and Dippel et al. [40] offers a solution for polymer bonds at large deformations. A further area of interest of aging effects can be found on non-metallic construction materials such as concrete, see [43–45], which are less appropriate for metals. In general, volume changes due to aging are not considered in the mentioned models.

The thermo-mechanical coupled problem has been treated in a large amount of works. Thermodynamical consistent modeling proposals for thermo-viscoplastic material behavior can be found in, for example [36,46–48]. Moreover, the work of Chaboche [32] offers an extensive overview of small-strain viscoplasticity models considering the thermo-mechanical coupling. In the case of finite deformations, the introduction of different effects in the model can be performed through a multiplicative decomposition of the deformation gradient. Lion [49] proposes constitutive equations for finite thermo-viscoplasticity deduced from rheological models. In this work, an additional multiplicative split of the deformation gradient is proposed in order to consider each physical effect included in the model: aging, temperature and mechanical effects. The equivalence of the order of decomposition of the deformation gradient for thermoelasticity has been discussed in [50]. The works of [51–53] provide investigations in the field of thermo-elasticity and thermo-viscoelasticity. Moreover, in the works of [54,55] one can find an extensive literature review for the coupled thermo-mechanical problem for the case of thermo-viscoelasticity and viscoplasticity for polymers and steel respectively. In the literature one can find many different proposals for aluminum alloys and steel in the field of thermo-viscoplasticity of metals, although, to the author's best knowledge, there are no proposals for the quasi-static behavior of Zamak apart from the previously made proposals from the authors.

The goal of this work is, on the one hand, to extend the available information about the zinc die casting alloy Zamak 5 providing temperature and aging-dependent experimental results for its thermo-mechanical characterization, and, on the other hand, to offer a constitutive model of finite deformations which is able to reproduce this complex strain rate, temperature and aging-dependent behavior. On the one hand, significant deformations occur in conjunction with substantial rigid body movements, necessitating the objectivity of stress and strain measurements. Conversely, the determination of material parameters does not mitigate the inaccuracies associated with moderate strains. In light of these considerations, it becomes evident that there is a challenge in developing a thermodynamically consistent material model that fulfills the Clausius–Duhem inequality. This resulting model does not only address the interaction between thermal and mechanical influences but also, and more specifically, considers the aging state of the material. Thus, a highly complex coupling is treated. The model is based on several multiplicative decompositions of the deformation gradient, yielding various pure strain measures connected to the individual physical properties. These are considered in the proposal of a specific strain-energy function, where the evolution equations of particular strain quantities are proposed. Moreover, subsets of material parameters can be determined separately by particular experiments. Finally, the entire model, which is implemented into a finite element program, is validated using totally different specimens with complex geometries, where we try to study a validation metric to obtain insight into the predicability of the model. The investigations provided in this work are based on [56].

The following notation is used in this work: geometrical vectors are symbolized by $\vec{a}$ and second-order tensors $\mathbf{A}$ by bold-faced Roman letters. Matrices at so-called global levels of finite elements are written as bold-faced italic letters $\boldsymbol{A}$, and matrices on the local (element) level are represented using bold-faced Roman letters $\mathbf{A}$.

2. Experimental Work

In previous investigations published in [3], the thermo-mechanical behavior of Zamak 5 without aging has been characterized. It was found that the material shows a strong dependence on the strain rate and the temperature. Both factors affect the initial slope as well as the height of the stress-strain curve. In [4], the effect of aging at room temperature on the mechanical response of Zamak has been investigated. There, a decrease of the stiffness with the increasing aging time could be observed. Additionally, a shrinkage takes place over the course of time due to microstructural changes in the alloy. Moreover, in [33], it is shown that the thermal conductivity is also influenced by the aging time and the temperature, which is connected to the previously mentioned changes in the microstructure.

In this work, the effect of natural aging on the thermo-mechanical response of Zamak is characterized. To this end, thin-walled cylindrical specimens made of Zamak 5 (ZnAl4Cu1) and having the dimensions $R_i = 13$ mm of the inner radius, $d = 2$ mm of the wall thickness, and $L = 90$ mm of the length (region between the clamping areas) are tested at different natural aging times, see [3,4] as well. Tension and Torsion experiments were performed with specimens with 3, 6 and 12 months of aging at 19 °C (natural aging). Since in [3] it has been observed that the tension-compression asymmetry can be neglected for a typical application of the alloy, only the tension experiments are considered for the additional aging times. In order to consider strain-rate dependence, the experiments are performed for all aging times at four different strain rates each ($\dot{\gamma}_k = 3.2 \times 10^{-(k+3)}\mathrm{s}^{-1}$, $k = 1, 2, 3, 4$ for torsion and $\dot{\varepsilon}_k = 3.3 \times 10^{-(k+3)}\mathrm{s}^{-1}$, $k = 1, 2, 3, 4$ for tension). The additional temperatures of −40 °C, 60 °C, and 85 °C are used to investigate the temperature dependence since this is the typical application range of the temperature in the automotive industry. The equilibrium stress state—defining that stress state obtained for an infinitely slow loading, unloading, and reloading process—is characterized at the different aging times and temperatures with the help of multi-step relaxation tests. The results are compared to the previous observations made in [3,4], where the results at room temperature and without aging are available. Additionally, shrinkage at three different temperatures is measured. These shrinkage measurements are important for the identification of an internal aging variable in a similar way as in [4], since they directly connect the microstructural changes over the course of time with the aging process.

2.1. Influence of Aging on the Thermo-Mechanical Behavior

The results of the torsion tests for the four temperatures and aging times are shown in Figure 1, and for the case of tension in Figure 2.

Each figure represents the results at one temperature. The measures in the diagrams are defined as follows: $\gamma = (\tan \varphi R_m)/L \approx (\varphi R_m)/L$ defines the shear angle of applied to a thin-walled cylindrical specimen, where R_m and L are the middle radius and the length of the specimen. φ symbolizes the applied testing machine's rotation angle. $\tau = M_T/(2dA_m)$ represents the shear stress concerned, with the measured torque M_T, the thickness d of the specimen's wall, and the mean cross-sectional area of the circular region $A_m = \pi R_m^2$. Furthermore, $\varepsilon = (L_e - L_0)/L_0$ defines the axial strain, where $L_0 = 20$ mm and L_e are the initial and current length of an applied extensometer. $\sigma = F/A$ defines the axial stress, with the measured axial force F and the specimens cross-section A. Details can be found in [3,4].

In all figures, different strain rates are represented by different colors and for one strain rate, the four aging times are represented by different line styles. For the chosen aging times, the main influence of aging occurs at room temperature; see Figures 1b and 2b. A reduction of 15% in the stresses over the aging time can be observed at all strain rates. Furthermore, the decrement between the initial state and 3 months of aging is larger than the decrement between 3 and 6 months of aging. This can be explained by the aging kinetics, since the material is in the unaged state far from a microstructural equilibrium, and, thus, the diffusion processes are more pronounced in the beginning of the aging process and decrease over time. One can observe a reduction in the initial slope with increased aging as well, but the effects of the temperature and the strain rate are more pronounced for the initial slope. For higher temperatures and lower strain rates, the influence of aging declines, which indicates that the viscous effects are affected by aging, see Figures 1c,d and 2c,d. At lower strain rates, the aging dependence is reduced until it almost vanishes at 85 °C at the slowest strain rate.

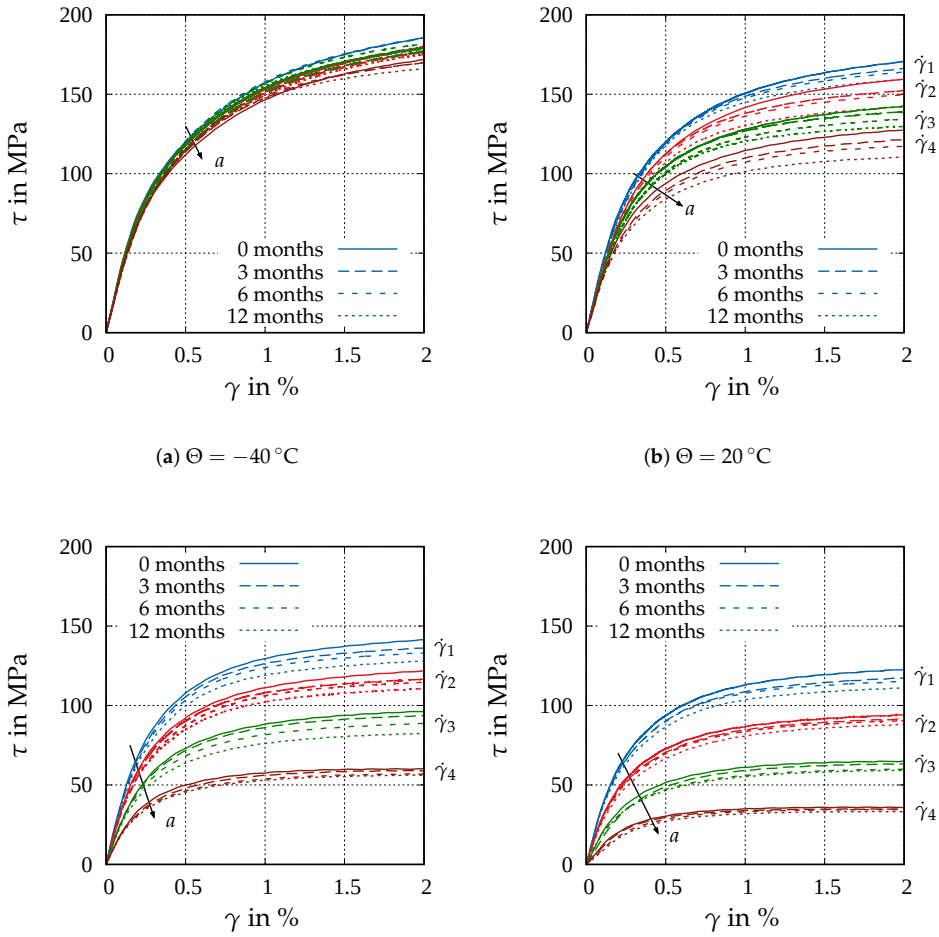

(**a**) $\Theta = -40\,^{\circ}\mathrm{C}$ (**b**) $\Theta = 20\,^{\circ}\mathrm{C}$

(**c**) $\Theta = 60\,^{\circ}\mathrm{C}$ (**d**) $\Theta = 85\,^{\circ}\mathrm{C}$

Figure 1. Effects of aging in torsion on the shear stress behavior at different shear strain rates and temperatures. Different strain rates represented by different colors. Different aging times are represented by different line styles. The arrow points in the direction of increasing aging time a.

At $-40\,^{\circ}\mathrm{C}$, the rate dependence is very small compared to the other temperatures. The effects of aging and rate dependence are almost overlapping. In the case of tension, see Figure 2a, it was not possible to perform all experiments up to the strain $\varepsilon = 1\%$ due to the brittleness of the material at this temperature. In relation to the equilibrium stress state, Figure 3 shows multi-step relaxation tests in torsion, and the estimated points of the equilibrium hysteresis for different aging times at four temperatures. Here, a slight dependence of the equilibrium stress state on the aging at room temperature can be observed. Again, this dependence is more pronounced at lower temperature and decreases with increasing temperatures until it becomes hardly perceptible at $85\,^{\circ}\mathrm{C}$. At higher temperatures, the viscous effects are predominant and the influence of aging in the equilibrium stress state is barely present.

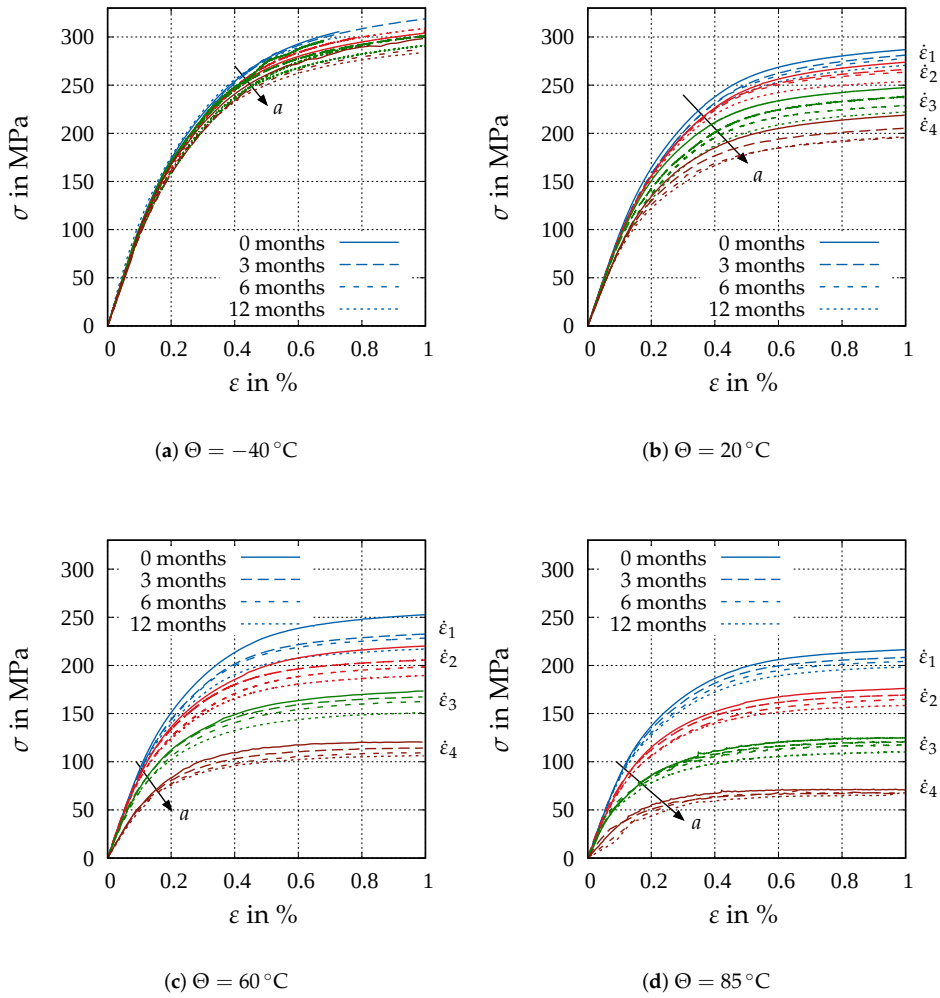

(**a**) $\Theta = -40\,^{\circ}\mathrm{C}$ (**b**) $\Theta = 20\,^{\circ}\mathrm{C}$

(**c**) $\Theta = 60\,^{\circ}\mathrm{C}$ (**d**) $\Theta = 85\,^{\circ}\mathrm{C}$

Figure 2. Effect of aging in tension at strain rates and different temperatures. Different strain rates are represented by different colors. Different aging times are represented by different line styles. The arrow points in the direction of increasing aging time a.

The previous observations have to be summarized: aging has the greatest influence on the material behavior at room temperature. Its influence is less pronounced at higher—in the sense of the temperatures applied here—temperatures. It has a stronger effect on the viscous behavior of the material than on the internal equilibrium stress state, see, for the terminology [48] and the literature cited therein. Moreover, the influence of natural aging is moderate compared to the effect of temperature or the strain rate. Nonetheless, the influence due to aging has to be considered for certain application areas. Additionally, it has to be pointed out that the 12 months of natural aging do not represent the final state of aging in the sense that the micro-structure reaches an equilibrium state. The natural aging investigations up to one year were chosen based on the results of the investigations in ([57] p. 62). However, in our studies it has been found that the final state of a fully aged material is approximately five years for applications at room temperature, see Section 2.2. This is also in agreement with the observations made in [8]. Therefore, a further reduction in the initial slope and the maximum stresses is to be expected for longer aging times than 12 months. Furthermore, aging influences other mechanical properties as well, for example those that are not treated in this work, for instance elongation at fracture, see [2].

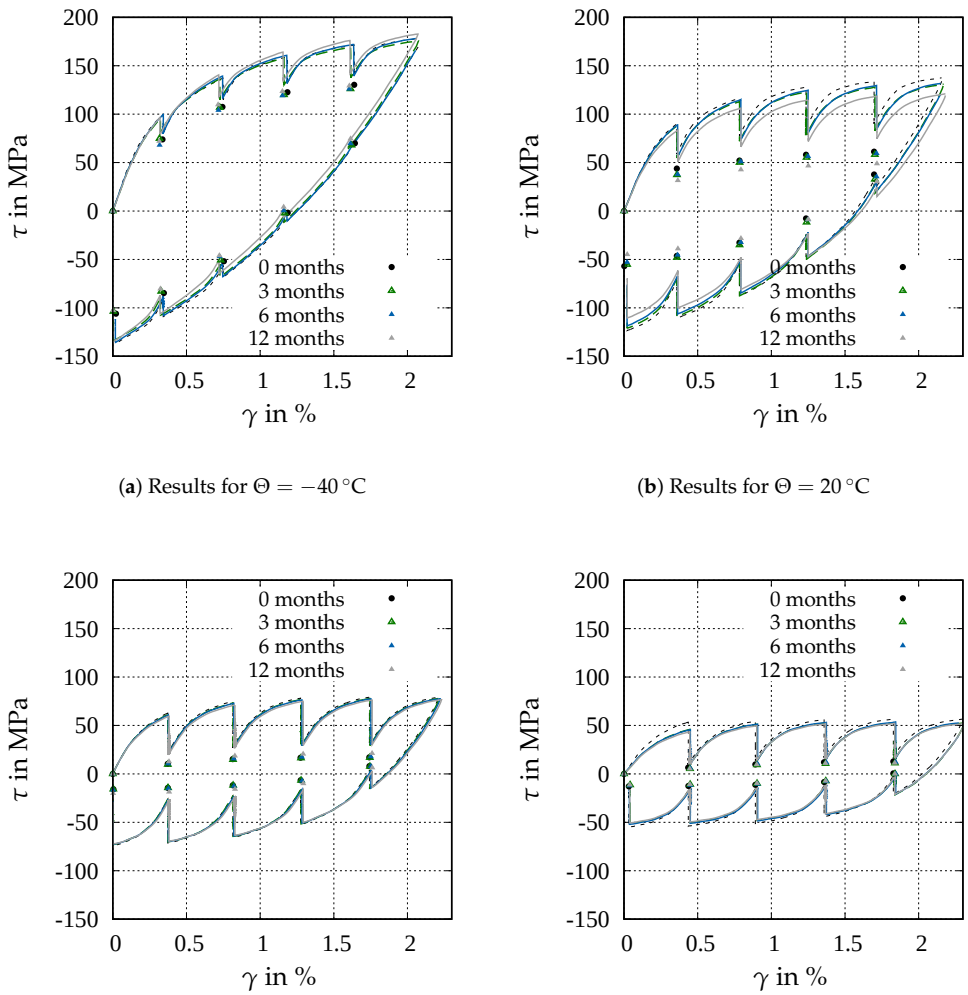

(**a**) Results for $\Theta = -40\,^{\circ}\mathrm{C}$

(**b**) Results for $\Theta = 20\,^{\circ}\mathrm{C}$

(**c**) Results for $\Theta = 60\,^{\circ}\mathrm{C}$

(**d**) Results for $\Theta = 85\,^{\circ}\mathrm{C}$

Figure 3. Influence of aging and temperature on the equilibrium stress state in torsion. Multi-step relaxation tests represented by lines and termination points of the relaxation by points.

2.2. Shrinkage

As exposed in [33] and the literature cited therein, the changes in the mechanical response with the course of time originate in microstructural changes such as diffusion, precipitation and decomposition of several phases of the alloy. One of the effects of aging is a reduction in the dimension or shrinkage of the material. In the next section, an internal variable will be used to model the effect of aging on the mechanical response. The measurements of the shrinkage are of particular interest for the definition of the aging variable, since they directly connect the aging process with the measured quantities. The results of the experiments in Figures 1 and 2 show a change in the mechanical response of the alloy in dependence of the aging time, but it is not possible to obtain a unique expression for the development of an aging variable from them. The works [8,57] mention a connection of the shrinkage in Zamak to a change in the crystallization system from fcc (face-centered cubic) to hcp (hexagonal close-packed), as well as to changes in the lattice parameter of some phases of the alloy. The deformation caused by these phase transformations associated to aging is purely volumetric. The measurements for specimens at room temperature from [8] show a maximum value of the shrinkage of about $-0.1\,\%$. Measurements of the shrinkage are an appropriate option to identify an internal process variable for aging in a unique manner, since this volume change is only connected to the microstructural changes, which occur during the aging process. The process is temperature-

activated due to the fact that the microstructural changes during the aging process are related to diffusion and precipitation of several alloying elements. At higher temperatures there is a faster development of the shrinkage. Since it takes more than one year to reach the completely aged stage at room temperature, the measurements of the shrinkage have been performed at higher temperatures, so that the aging takes place in a reasonable period of time.

In the measurements, the specimen is heated up to the temperature Θ_{exp}. The heating rate is chosen to be fast enough so that shrinkage caused by the aging can be neglected during the heating phase and it is equal to $10\,\text{K}\,\text{min}^{-1}$. The temperature is then kept constant over the time. The specimen has an initial length L_0 and it shrinks over time until the length reaches a saturation value L_∞, see Figure 4.

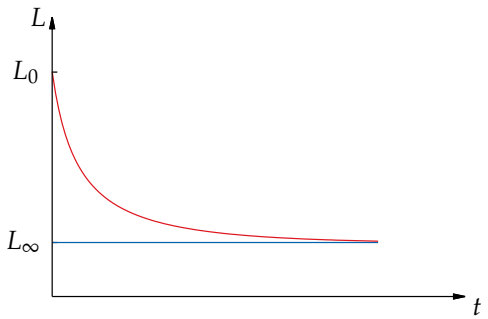

Figure 4. Concept of the shrinkage measurement.

As a measure of the aging development, the current longitudinal deformation $\varepsilon_{\text{exp}} = (L - L_0)/L_0$ is used.

The measurements of the shrinkage were carried out with a Mettler Toledo (TMA 841^e; performed at the Institute of Mechanics of the Bundeswehr University Munich). Figure 5 displays the results of the measurements, which were carried out at a temperatures of 85 °C, 105 °C, and 125 °C. Figure 5a—measurements over the time in logarithmic scale—is used to compare the shrinkage measurements at 20 °C with results in [8] for the same alloy. We can observe a faster deformation rate at higher temperatures. The measurement at 125 °C reaches a saturation value after approximately 18 h. The measurement at 105 °C is still far away from the final saturation state after 24 h. The saturation value observed in the measurement at 125 °C is approximately −0.14 %, and larger than the one of the measurement from [8], which was reached after approximately 5 years at 20 °C.

We notice a deviation between the results from Figure 5 and [57] for Zamak 5 as well. In [57], the alloy reaches the final stage at 120 °C after 0.4 days. This deviation can be observed as well comparing the measurement from [8] and the results from [57]. In [8] the specimens reach the final state after approximately five years at 20 °C and in [57] only after one year of natural aging. Thus, additional tests of the mechanical behavior were performed in order to determine whether the specimens with 12 months of natural aging represent the completely aged state. A torsion test at room temperature and the fastest strain rate $\dot{\gamma}_1$ was performed with further specimens which were artificially aged at temperatures of 80 °C for 24 h, 100 °C for 24 h, and 120 °C for 44 h. According to the investigations in [33] and the results in Figure 5a, the specimen with thermal treatment at 120 °C for 44 h reaches a completely aged state. The results of these new measurements are compared with the natural aged specimens in Figure 5b. Here, one can see that the material with one year of natural aging still does not correspond to the final aged state. The deviation from the results from [57] indicates further dependencies of the development of aging not only on the composition of the alloy, but also on other parameters of the die casting process which were not considered in this work. It is possible as well that the final microstructural state reached after a long heating process does not correspond completely to the same microstructural equilibrium state at lower temperatures. Since a more detailed investigation of this effect is out of the scope of this work, these dependencies are not

investigated further. Nevertheless, it is taken into account that 12 months of natural aging does not correspond to the completely aged state.

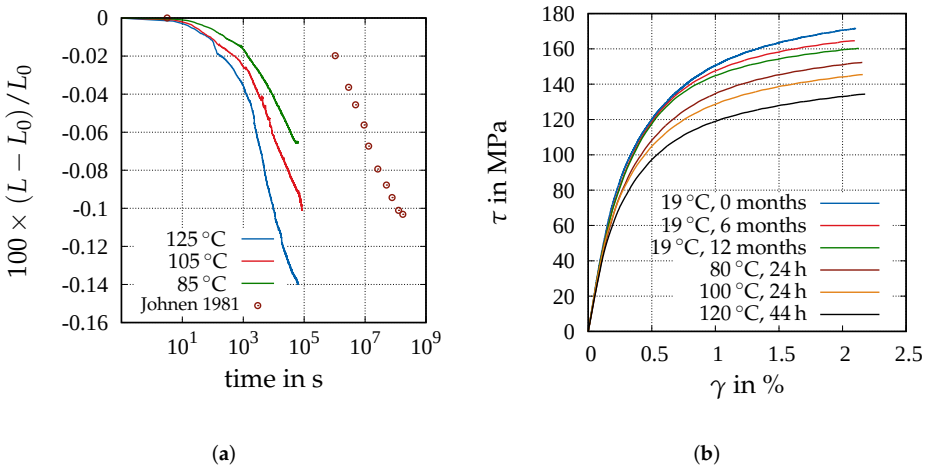

(**a**) (**b**)

Figure 5. Shrinkage measurements and mechanical response of artificially aged material. (**a**) Shrinkage of Zamak 5 at temperatures of 85 °C, 105 °C, and 125 °C over the course of time in logarithmic scale and measurements published in [8] at 20 °C. (**b**) Comparison of torsion tests at 20 °C of specimens with natural aging and specimens with artificial aging close to the completely aged stage.

3. Constitutive Model of Large Deformations for Zamak 5

In the following, we develop a phenomenological constitutive model under the assumption of large strains. Since the possible strains exceed 1 % and applications require models for large displacements, a geometrical non-linear theory is necessary. Here, we draw on an overstress-type modeling concept, see, for example [58–61], where the total stress state is decomposed into a rate-independent equilibrium stress state, and a rate-dependent overstress part. The equilibrium stress part can be either obtained by an infinitely slow loading process, what is not feasible from a practical point of view, or by a multi-step relaxation path, where the termination points of relaxation—or some estimated points—determine the internal equilibrium state. Considering the experimental results, the material shows a strong viscoplastic material response, where the viscous effects are influenced by the temperature and the aging state. The equilibrium stress state is mostly influenced by the temperature. Moreover, a volume change due to aging (shrinkage) and due to temperature changes was observed, see [33]. The proposed constitutive model is based on the experience and knowledge of the small deformations model of [3]. In this case, the model structure is motivated by a rheological model, see Figure 6.

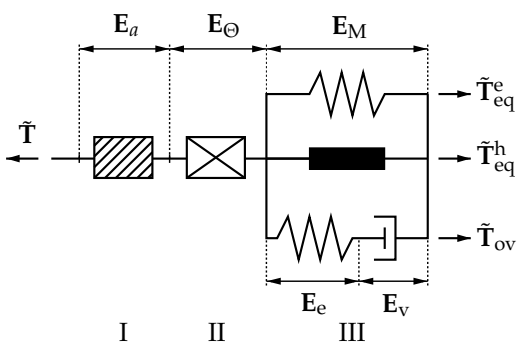

Figure 6. Rheological Model.

There are three main elements connected in series: an element describing the shrinkage due to aging (I), a thermal element (II) corresponding to the thermal expansion, and a mechanical element (III). In the mechanical element, the total stress $\tilde{\mathbf{T}}$ is decomposed into

an equilibrium stress part $\tilde{\mathbf{T}}_{\mathrm{eq}}$ and an overstress part $\tilde{\mathbf{T}}_{\mathrm{ov}}$. $\tilde{\mathbf{T}} = (\det \mathbf{F})\mathbf{F}^{-1}\mathbf{T}\mathbf{F}^{-\mathrm{T}}$ defines the 2nd Piola-Kirchhoff stress tensor, $\mathbf{T}$ the Cauchy stress tensor, and $\mathbf{F} = \mathrm{Grad}\,\vec{\chi}_{\mathrm{R}}(\vec{X}, t)$the deformation gradient. $\vec{x} = \vec{\chi}_{\mathrm{R}}(\vec{X}, t)$ represents the motion of the material point $\vec{X}$ occupying the point $\vec{x}$ at time t in the current configuration. The equilibrium stress part $\tilde{\mathbf{T}}_{\mathrm{eq}}$ represents the equilibrium hysteresis and is composed of an elastic stress part related to the spring $\tilde{\mathbf{T}}^{\mathrm{e}}_{\mathrm{eq}}$ and a plastic component related to the plastic element $\tilde{\mathbf{T}}^{\mathrm{h}}_{\mathrm{eq}}$. The overstress $\tilde{\mathbf{T}}_{\mathrm{ov}}$ is modeled with a Maxwell-element, which is responsible for the rate-dependent response. Thus, the total stress is expressed by

$$\tilde{\mathbf{T}} = \tilde{\mathbf{T}}_{\mathrm{eq}} + \tilde{\mathbf{T}}_{\mathrm{ov}} = \tilde{\mathbf{T}}^{\mathrm{e}}_{\mathrm{eq}} + \tilde{\mathbf{T}}^{\mathrm{h}}_{\mathrm{eq}} + \tilde{\mathbf{T}}_{\mathrm{ov}}. \tag{1}$$

The decomposition of the stress into equilibrium stresses and overstresses shows advantages in the parameter identification procedure, since the parameters of the equilibrium stress part $\tilde{\mathbf{T}}_{\mathrm{eq}}$ can independently be identified of the parameters of the overstress $\tilde{\mathbf{T}}_{\mathrm{ov}}$. In the following, the rate-independent hysteretic part $\tilde{\mathbf{T}}^{\mathrm{h}}_{\mathrm{eq}}$ is called plastic part.

In order to consider the different physical effects, the deformation gradient is decomposed into an aging $\mathbf{F}_a$, a thermal $\mathbf{F}_\Theta$, and a mechanical part $\mathbf{F}_{\mathrm{M}}$,

$$\mathbf{F} = \mathbf{F}_a \mathbf{F}_\Theta \mathbf{F}_{\mathrm{M}}. \tag{2}$$

The thermal and aging parts are assumed to behave purely volumetrical

$$\mathbf{F}_\Theta = \varphi_\Theta(\Theta)\mathbf{I}, \qquad \mathbf{F}_a = \varphi_a(a)\mathbf{I}, \tag{3}$$

where $\varphi_\Theta(\Theta)$ and $\varphi_a(a)$ are scalar functions of the temperature Θ and of the aging variable a

$$\varphi_\Theta(\Theta) = 1 + \alpha_\Theta(\Theta - \Theta_0), \tag{4}$$
$$\varphi_a(a) = 1 - \alpha_a a, \tag{5}$$

with $\alpha_\Theta, \alpha_a > 0$. As suggested by Flory [62], the mechanical deformation gradient $\mathbf{F}_{\mathrm{M}}$ is decomposed into a volumetric part $\hat{\mathbf{F}}_{\mathrm{M}}$ and an isochoric part $\bar{\mathbf{F}}_{\mathrm{M}}$

$$\mathbf{F}_{\mathrm{M}} = \hat{\mathbf{F}}_{\mathrm{M}} \bar{\mathbf{F}}_{\mathrm{M}}, \tag{6}$$

with

$$\hat{\mathbf{F}}_{\mathrm{M}} = (\det \mathbf{F}_{\mathrm{M}})^{1/3}\mathbf{I}, \qquad \det \hat{\mathbf{F}}_{\mathrm{M}} = \det \mathbf{F}_{\mathrm{M}}, \tag{7}$$
$$\bar{\mathbf{F}}_{\mathrm{M}} = (\det \mathbf{F}_{\mathrm{M}})^{-1/3}\mathbf{F}_{\mathrm{M}}, \qquad \det \bar{\mathbf{F}}_{\mathrm{M}} = 1. \tag{8}$$

The Maxwell-element in the rheological model is considered with the decomposition of the mechanical part of the deformation gradient into an elastic part $\mathbf{F}_{\mathrm{e}}$ and an isochoric viscous part $\bar{\mathbf{F}}_{\mathrm{v}}$,

$$\mathbf{F}_{\mathrm{M}} = \mathbf{F}_{\mathrm{e}} \bar{\mathbf{F}}_{\mathrm{v}} = \hat{\mathbf{F}}_{\mathrm{e}} \bar{\mathbf{F}}_{\mathrm{e}} \bar{\mathbf{F}}_{\mathrm{v}}. \tag{9}$$

Moreover, the mechanical deformation gradient is decomposed in a similar way as in [49,63], into an elastic (kinematic hardening part) $\mathbf{F}_{\mathrm{k}}$ and a plastic component $\bar{\mathbf{F}}_{\mathrm{p}}$ to model the plastic element,

$$\mathbf{F}_{\mathrm{M}} = \mathbf{F}_{\mathrm{k}} \bar{\mathbf{F}}_{\mathrm{p}} = \hat{\mathbf{F}}_{\mathrm{k}} \bar{\mathbf{F}}_{\mathrm{k}} \bar{\mathbf{F}}_{\mathrm{p}}. \tag{10}$$

Due to the fact that there is no distinction between an elastic and a plastic range, such as it is the case in yield function based models, the interpretation of the components differs from [49,63]. The hysteretic response of the equilibrium stress is assigned to the term $\mathbf{F}_{\mathrm{k}}$, which corresponds to the strain-like variable $\mathbf{Y}$ in the small deformations case, see [3]. The

condition of inelastic incompressibility is considered with the components $\bar{\mathbf{F}}_\mathrm{v}$ and $\bar{\mathbf{F}}_\mathrm{p}$ being purely isochoric. The decomposition of the deformation gradient is shown in Figure 7.

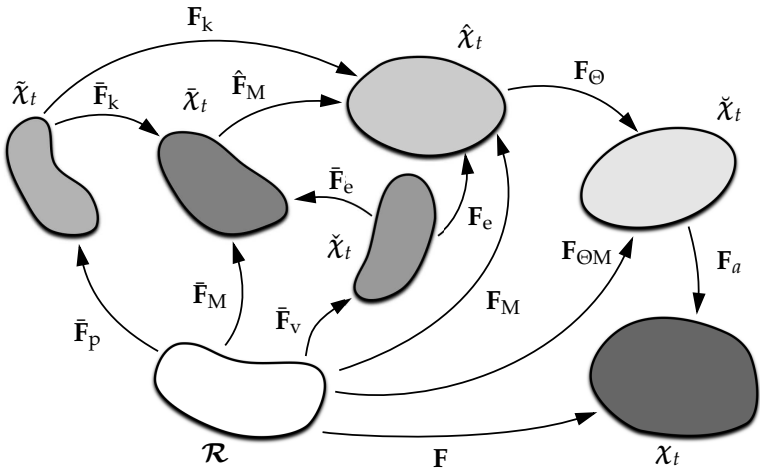

Figure 7. Multiplicative split of the deformation gradient.

There $\check{\chi}_t$, $\bar{\chi}_t$, $\hat{\chi}_t$, $\check{\chi}_t$, and $\tilde{\chi}_t$ represent the intermediate configurations caused by the decomposition of $\mathbf{F}$.

The split of the deformation gradient allows the definition of a number of strain measures, which are formulated relative to particular configurations. Considering the right Cauchy-Green tensor $\mathbf{C} = \mathbf{F}^\mathrm{T}\mathbf{F}$, the Green strain tensor can be decomposed as well,

$$\mathbf{E} = \frac{1}{2}(\mathbf{C} - \mathbf{I}) = \frac{1}{2}(\mathbf{C} - \mathbf{C}_{\Theta\mathrm{M}}) + \frac{1}{2}(\mathbf{C}_{\Theta\mathrm{M}} - \mathbf{C}_\mathrm{M}) + \frac{1}{2}(\mathbf{C}_\mathrm{M} - \mathbf{I}). \tag{11}$$

Using $\mathbf{F}_{\Theta\mathrm{M}} = \mathbf{F}_\Theta\mathbf{F}_\mathrm{M} = \varphi_\Theta\mathbf{F}_\mathrm{M}$ and $\mathbf{F} = \varphi_a\varphi_\Theta\mathbf{F}_\mathrm{M}$, the components right Cauchy-Green type tensors $\mathbf{C}_\mathrm{M}$, $\mathbf{C}_{\Theta\mathrm{M}}$ and $\mathbf{C}$ are defined by

$$\mathbf{C}_\mathrm{M} = \mathbf{F}_\mathrm{M}^\mathrm{T}\mathbf{F}_\mathrm{M}, \tag{12}$$

$$\mathbf{C}_{\Theta\mathrm{M}} = \mathbf{F}_{\Theta\mathrm{M}}^\mathrm{T}\mathbf{F}_{\Theta\mathrm{M}} = \varphi_\Theta^2\mathbf{F}_\mathrm{M}^\mathrm{T}\mathbf{F}_\mathrm{M}, \tag{13}$$

$$\mathbf{C} = \mathbf{F}^\mathrm{T}\mathbf{F} = \varphi_a^2\varphi_\Theta^2\mathbf{F}_\mathrm{M}^\mathrm{T}\mathbf{F}_\mathrm{M}. \tag{14}$$

Inserting definitions (12)–(14) into Equation (11) results in

$$\mathbf{E} = \frac{1}{2}(\varphi_a^2 - 1)\varphi_\Theta^2\mathbf{C}_\mathrm{M} + \frac{1}{2}(\varphi_\Theta^2 - 1)\mathbf{C}_\mathrm{M} + \frac{1}{2}(\mathbf{C}_\mathrm{M} - \mathbf{I}) = \mathbf{E}_a + \mathbf{E}_\Theta + \mathbf{E}_\mathrm{M}. \tag{15}$$

Thus, the Green strain tensor decomposes into three different components: the aging strain $\mathbf{E}_a$, the thermal strain $\mathbf{E}_\Theta$, and the mechanical strain $\mathbf{E}_\mathrm{M}$,

$$\mathbf{E}_a = \frac{1}{2}(\varphi_a^2 - 1)\varphi_\Theta^2\mathbf{C}_\mathrm{M}, \quad \mathbf{E}_\Theta = \frac{1}{2}(\varphi_\Theta^2 - 1)\mathbf{C}_\mathrm{M}, \quad \mathbf{E}_\mathrm{M} = \frac{1}{2}(\mathbf{C}_\mathrm{M} - \mathbf{I}). \tag{16}$$

The mechanical strain tensor $\mathbf{E}_\mathrm{M}$ is assigned both to the Maxwell-element as well as the rate-independent endochronic element, see Figure 6,

$$\mathbf{E}_\mathrm{M} = \frac{1}{2}(\mathbf{C}_\mathrm{M} - \mathbf{I}) = \frac{1}{2}(\mathbf{C}_\mathrm{M} - \bar{\mathbf{C}}_\mathrm{v}) + \frac{1}{2}(\bar{\mathbf{C}}_\mathrm{v} - \mathbf{I}) = \mathbf{E}_\mathrm{e} + \mathbf{E}_\mathrm{v}, \tag{17}$$

$$\mathbf{E}_\mathrm{M} = \frac{1}{2}(\mathbf{C}_\mathrm{M} - \mathbf{I}) = \frac{1}{2}(\mathbf{C}_\mathrm{M} - \bar{\mathbf{C}}_\mathrm{p}) + \frac{1}{2}(\bar{\mathbf{C}}_\mathrm{p} - \mathbf{I}) = \mathbf{E}_\mathrm{k} + \mathbf{E}_\mathrm{p}, \tag{18}$$

with $\bar{\mathbf{C}}_\mathrm{v} = \bar{\mathbf{F}}_\mathrm{v}^\mathrm{T}\bar{\mathbf{F}}_\mathrm{v}$ and $\bar{\mathbf{C}}_\mathrm{p} = \bar{\mathbf{F}}_\mathrm{p}^\mathrm{T}\bar{\mathbf{F}}_\mathrm{p}$. $\bar{\mathbf{C}}_\mathrm{v} = (\det\mathbf{C}_\mathrm{v})^{-1/3}\mathbf{C}_\mathrm{v}$ and $\bar{\mathbf{C}}_\mathrm{p} = (\det\mathbf{C}_\mathrm{p})^{-1/3}\mathbf{C}_\mathrm{p}$ are unimodular tensors, which we anticipate here due to the later choice of the evolutionary equations. In other words, the mechanical strain decomposes into an elastic and a viscous

part (Maxwell-element) $\mathbf{E}_\mathrm{M} = \mathbf{E}_\mathrm{e} + \mathbf{E}_\mathrm{v}$, or an elastic and plastic part $\mathbf{E}_\mathrm{M} = \mathbf{E}_\mathrm{k} + \mathbf{E}_\mathrm{p}$ (rate-independent plastic element),

$$\mathbf{E}_\mathrm{e} = \frac{1}{2}(\mathbf{C}_\mathrm{M} - \bar{\mathbf{C}}_\mathrm{v}), \qquad \mathbf{E}_\mathrm{v} = \frac{1}{2}(\bar{\mathbf{C}}_\mathrm{v} - \mathbf{I}), \tag{19}$$

$$\mathbf{E}_\mathrm{k} = \frac{1}{2}(\mathbf{C}_\mathrm{M} - \bar{\mathbf{C}}_\mathrm{p}), \qquad \mathbf{E}_\mathrm{p} = \frac{1}{2}(\bar{\mathbf{C}}_\mathrm{p} - \mathbf{I}). \tag{20}$$

These strain measures can be formulated relative to different configurations. For example, the mechanical part of the strain tensor $\boldsymbol{\varepsilon}_\mathrm{M} = \frac{1}{2}(\mathbf{F}_\mathrm{e}^\mathrm{T}\mathbf{F}_\mathrm{e} - \bar{\mathbf{F}}_\mathrm{v}^{-\mathrm{T}}\bar{\mathbf{F}}_\mathrm{v}^{-1})$ relative to the elastic intermediate configuration $\check{\chi}_t$ can be decomposed in a purely elastic component $\boldsymbol{\varepsilon}_\mathrm{e}$ and a purely viscous part $\boldsymbol{\varepsilon}_\mathrm{v}$,

$$\boldsymbol{\varepsilon}_\mathrm{e} = \frac{1}{2}(\mathbf{F}_\mathrm{e}^\mathrm{T}\mathbf{F}_\mathrm{e} - \mathbf{I}), \qquad \boldsymbol{\varepsilon}_\mathrm{v} = \frac{1}{2}(\mathbf{I} - \bar{\mathbf{F}}_\mathrm{v}^{-\mathrm{T}}\bar{\mathbf{F}}_\mathrm{v}^{-1}), \tag{21}$$

see Figure A1. Furthermore, quantities relative to the plastic configuration $\tilde{\chi}_t$ can be defined. Namely the mechanical strain tensor $\tilde{\boldsymbol{\varepsilon}}_\mathrm{M} = \frac{1}{2}(\mathbf{F}_\mathrm{k}^\mathrm{T}\mathbf{F}_\mathrm{k} - \bar{\mathbf{F}}_\mathrm{p}^{-\mathrm{T}}\bar{\mathbf{F}}_\mathrm{p}^{-1})$, which can be decomposed into a component depending exclusively on $\mathbf{F}_\mathrm{k}$ and one depending only on $\bar{\mathbf{F}}_\mathrm{p}$

$$\tilde{\boldsymbol{\varepsilon}}_\mathrm{k} = \frac{1}{2}(\mathbf{F}_\mathrm{k}^\mathrm{T}\mathbf{F}_\mathrm{k} - \mathbf{I}), \qquad \tilde{\boldsymbol{\varepsilon}}_\mathrm{p} = \frac{1}{2}(\mathbf{I} - \bar{\mathbf{F}}_\mathrm{p}^{-\mathrm{T}}\bar{\mathbf{F}}_\mathrm{p}^{-1}). \tag{22}$$

Figure A1 of the Appendix A shows the transformations of the strain measures relative to the different configurations.

3.1. Resulting Stresses and Evolution Equations

The constitutive model has to satisfy the Clausius-Duhem inequality for fulfilling thermodynamical consistence. In order to minimize the presentation here, the proof is compiled in Appendix C. We assume a specific free energy, which is divided into an elastic $\psi_\mathrm{eq}^\mathrm{e}$ (spring element), a plastic $\psi_\mathrm{eq}^\mathrm{h}$ (rate-independent plastic component), an overstress ψ_ov (Maxwell-element), a thermal ψ_Θ, and an aging part ψ_a

$$\psi(\mathbf{E}_\mathrm{M}, \tilde{\boldsymbol{\varepsilon}}_\mathrm{k}, \boldsymbol{\varepsilon}_\mathrm{e}, k, a, \Theta) = \psi_\mathrm{eq}^\mathrm{e}(\mathbf{E}_\mathrm{M}) + \psi_\mathrm{eq}^\mathrm{h}(\tilde{\boldsymbol{\varepsilon}}_\mathrm{k}, \Theta) + \psi_\mathrm{ov}(\boldsymbol{\varepsilon}_\mathrm{e}, k) + \psi_\Theta(\Theta) + \psi_a(a). \tag{23}$$

The internal variable k represents a softening variable having the goal of considering a change of the initial slopes in loading and unloading. This was observed in the experiments, see [3]. For the elastic component $\psi_\mathrm{eq}^\mathrm{e}(\mathbf{E}_\mathrm{M})$ of the specific free energy, an expression of near-incompressibility is chosen. Here, the specific free energy is decomposed into a volumetric and an isochoric component

$$\rho_\mathrm{R}\psi_\mathrm{eq}^\mathrm{e}(\mathbf{E}_\mathrm{M}) = U(J_\mathrm{M}) + \bar{\omega}(\bar{\mathbf{C}}_\mathrm{M}), \tag{24}$$

ρ_R defines the density in the reference configuration. The volume changing part of the energy function $U(J_\mathrm{M})$ is chosen according to [64] depending on the determinant of the mechanical deformation gradient $J_\mathrm{M} := \det \mathbf{F}_\mathrm{M}$, see Equation (A47). For the isochoric part component a Neo-Hooke ansatz is chosen, see Equation (A48), depending on the unimodular mechanical right Cauchy-Green tensor $\bar{\mathbf{C}}_\mathrm{M}$. This term is equal to the total unimodular Cauchy-Green tensor $\bar{\mathbf{C}}_\mathrm{M} = \bar{\mathbf{C}} = (\det \mathbf{C}_\mathrm{M})^{-1/3}\mathbf{C}_\mathrm{M}$ (the aging and the thermal part are purely volumetric).

The plastic element and the Maxwell-element are both able to reproduce a hysteretic behavior, with the difference that the Maxwell-element is rate-dependent. The rate independence is included in the plastic element with definition (38) due to the proportionality of the strain rate $\overset{\triangle}{\tilde{\boldsymbol{\varepsilon}}}_\mathrm{p}$ to the rate of the arc-length $\dot{s}_\mathrm{M}$. For these elements, a Neo-Hookean ansatz

is chosen too, in which the parameters $\mu_{\mathrm{eq}}(\Theta)$ and $\mu_{\mathrm{ov}}(k)$ are affected by the temperature and the softening respectively

$$\rho_{\mathrm{R}}\psi^{\mathrm{h}}_{\mathrm{eq}}(\tilde{\varepsilon}_{\mathrm{k}},\Theta) = \mu_{\mathrm{eq}}(\Theta)(I_{\bar{\mathbf{C}}_{\mathrm{k}}} - 3), \qquad \bar{\mathbf{C}}_{\mathrm{k}} = (\det \mathbf{C}_{\mathrm{k}})^{-1/3}\mathbf{C}_{\mathrm{k}}, \tag{25}$$

$$\rho_{\mathrm{R}}\psi_{\mathrm{ov}}(\boldsymbol{\varepsilon}_{\mathrm{e}},k) = \mu_{\mathrm{ov}}(k)(I_{\bar{\mathbf{C}}_{\mathrm{e}}} - 3), \qquad \bar{\mathbf{C}}_{\mathrm{e}} = (\det \mathbf{C}_{\mathrm{e}})^{-1/3}\mathbf{C}_{\mathrm{e}}. \tag{26}$$

$\mathrm{I}_{\mathbf{A}} = \mathrm{tr}\,\mathbf{A} = \mathbf{A}\cdot\mathbf{I} = a^k_k$ defines the trace operator of a second-order tensor. For the aging part of the free energy, the expression

$$\rho_{\mathrm{R}}\psi_a(a) = C_1 - C_2 a, \tag{27}$$

is chosen and for the thermal part, the expression proposed by [65] is selected

$$\rho_{\mathrm{R}}\psi_{\Theta}(\Theta) = c_{\mathrm{p1}}\left((\Theta - \Theta_0) - \Theta \ln\frac{\Theta}{\Theta_0}(1 - c_{\mathrm{p2}}\Theta) - \frac{1}{2}(\Theta^2 - \Theta_0^2)\right). \tag{28}$$

With this function, the specific heat capacity obtains a linear dependence on the temperature, which corresponds to the experimental results shown in [33].

From considering the Clausius-Duhem inequality, see the Appendix C, and the chosen free energy functions, the following expressions arise for the components of the stress tensors

$$\mathbf{S}^{\mathrm{e}}_{\mathrm{Meq}} = \frac{\rho_{\mathrm{R}}}{\varphi^2_{\Theta}\varphi^2_a}\mathbf{F}_{\mathrm{M}}\frac{\partial\psi}{\partial\mathbf{E}_{\mathrm{M}}}\mathbf{F}^{\mathrm{T}}_{\mathrm{M}} = (\varphi_{\Theta}\varphi_a)^{-2}\frac{K}{10}(J^5_{\mathrm{M}} - J^{-5}_{\mathrm{M}})\mathbf{I} + (\varphi_{\Theta}\varphi_a)^{-2}2c_{10}\bar{\mathbf{B}}^{\mathrm{D}}_{\mathrm{M}}, \tag{29}$$

$$\check{\mathbf{S}}_{\mathrm{ov}} = \frac{\rho_{\mathrm{R}}}{\varphi^2_{\Theta}\varphi^2_a}\frac{\partial\psi}{\partial\boldsymbol{\varepsilon}_{\mathrm{e}}} = 2\mu_{\mathrm{eq}}(\varphi_{\Theta}\varphi_a)^{-2}\mathbf{C}^{-1}_{\mathrm{k}}\bar{\mathbf{C}}^{\mathrm{D}}_{\mathrm{k}}, \tag{30}$$

$$\tilde{\mathbf{S}}^{\mathrm{h}}_{\mathrm{eq}} = \frac{\rho_{\mathrm{R}}}{\varphi^2_{\Theta}\varphi^2_a}\frac{\partial\psi}{\partial\tilde{\varepsilon}_{\mathrm{k}}} = 2\mu_{\mathrm{ov}}(\varphi_{\Theta}\varphi_a)^{-2}\mathbf{C}^{-1}_{\mathrm{e}}\bar{\mathbf{C}}^{\mathrm{D}}_{\mathrm{e}}, \tag{31}$$

see Figure A3 for the different stress tensors. Here, the exponent D represents the deviator of a second-order tensor, $\mathbf{A}^D = \mathbf{A} - (\mathrm{tr}\,\mathbf{A})/3\mathbf{I}$. For the implementation of the model, the second Piola-Kirchhoff-type stresses relative to the reference configuration are of interest. Making use of the relations $\mathbf{F}_{\mathrm{M}} = (\varphi_a\varphi_{\Theta})^{-1}\mathbf{F}$, $J_{\mathrm{M}} = (\varphi_a\varphi_{\Theta})^{-3}J$, $J := \det\mathbf{F}$, one obtains

$$\tilde{\mathbf{T}}^{\mathrm{e}}_{\mathrm{eq}} = \mathbf{F}^{-1}_{\mathrm{M}}\mathbf{S}^{\mathrm{e}}_{\mathrm{Meq}}\mathbf{F}^{-\mathrm{T}}_{\mathrm{M}} = (\varphi_{\Theta}\varphi_a)^{-2}\left(\frac{K}{10}(J^5_{\mathrm{M}} - J^{-5}_{\mathrm{M}})\mathbf{C}^{-1}_{\mathrm{M}} + 2c_{10}J^{-2/3}_{\mathrm{M}}\mathbf{C}^{-1}_{\mathrm{M}}\mathbf{C}^{\mathrm{D}}_{\mathrm{M}}\right) \tag{32}$$

$$\tilde{\mathbf{T}}^{\mathrm{h}}_{\mathrm{eq}} = \bar{\mathbf{F}}^{-1}_{\mathrm{p}}\mathbf{S}^{\mathrm{h}}_{\mathrm{Meq}}\bar{\mathbf{F}}^{-\mathrm{T}}_{\mathrm{p}} = 2\mu_{\mathrm{eq}}J^{-2/3}\mathbf{C}^{-1}(\mathbf{C}\bar{\mathbf{C}}^{-1}_{\mathrm{p}})^{\mathrm{D}}, \tag{33}$$

$$\tilde{\mathbf{T}}_{\mathrm{ov}} = \bar{\mathbf{F}}^{-1}_{\mathrm{v}}\check{\mathbf{S}}_{\mathrm{ov}}\bar{\mathbf{F}}^{-\mathrm{T}}_{\mathrm{v}} = 2\mu_{\mathrm{ov}}J^{-2/3}\mathbf{C}^{-1}(\mathbf{C}\bar{\mathbf{C}}^{-1}_{\mathrm{v}})^{\mathrm{D}}. \tag{34}$$

Moreover, after a push-forward operation,

$$\mathbf{S}^{\mathrm{e}}_{\mathrm{eq}} = \mathbf{F}\tilde{\mathbf{T}}^{\mathrm{e}}_{\mathrm{eq}}\mathbf{F}^{\mathrm{T}} = \mathbf{S}^{\mathrm{e}}_{\mathrm{vol}} + \mathbf{S}^{\mathrm{e}}_{\mathrm{iso}} = \frac{K}{10}\left(J^5_{\mathrm{M}} - J^{-5}_{\mathrm{M}}\right)\mathbf{I} + 2c_{10}\bar{\mathbf{B}}^{\mathrm{D}}_{\mathrm{M}}. \tag{35}$$

$$\mathbf{S}^{\mathrm{h}}_{\mathrm{eq}} = \mathbf{F}\tilde{\mathbf{T}}^{\mathrm{h}}_{\mathrm{eq}}\mathbf{F}^{\mathrm{T}} = 2\mu_{\mathrm{eq}}\bar{\mathbf{B}}^{\mathrm{D}}_{\mathrm{k}}, \tag{36}$$

$$\mathbf{S}_{\mathrm{ov}} = \mathbf{F}\tilde{\mathbf{T}}_{\mathrm{ov}}\mathbf{F}^{\mathrm{T}} = 2\mu_{\mathrm{ov}}\bar{\mathbf{B}}^{\mathrm{D}}_{\mathrm{e}}, \tag{37}$$

one can see that the plastic stress part $\mathbf{S}^{\mathrm{h}}_{\mathrm{eq}}$ and the overstress $\mathbf{S}_{\mathrm{ov}}$ in the current configuration are purely deviatoric. $\mathbf{S}^{\mathrm{e}}_{\mathrm{vol}}$ is the only volumetric stress contribution and represents the only part connected to elastic volumetric processes, see Equation (A59).

Additionally, expressions for the evolution equations have to be found. The following relations ensure the thermodynamical consistence of the model

$$\overset{\triangle}{\tilde{\varepsilon}}_{\mathrm{p}} = \beta_{\mathbf{Y}} \dot{s}_{\mathrm{M}} \mathbf{C}_{\mathrm{k}} \tilde{\mathbf{S}}^{\mathrm{h}}_{\mathrm{eq}}, \qquad \beta_{\mathbf{Y}}, \dot{s}_{\mathrm{M}} > 0, \tag{38}$$

$$\overset{\triangle}{\tilde{\varepsilon}}_{\mathrm{v}} = \frac{1}{\hat{\eta}} \mathbf{C}_{\mathrm{e}} \check{\mathbf{S}}_{\mathrm{ov}}, \qquad \hat{\eta} > 0, \tag{39}$$

$$\dot{k} \geq 0, \qquad \frac{\partial \psi}{\partial k} \leq 0, \tag{40}$$

$$\dot{a} = \beta_g \left(\varphi_a \frac{\partial \varphi_a}{\partial a} (\operatorname{tr} \check{\mathbf{S}}) - \frac{\partial \psi}{\partial a} \right), \qquad \beta_g > 0, \tag{41}$$

$$\vec{q}_R = -\boldsymbol{\kappa}^{\mathrm{R}}_{\Theta} \operatorname{Grad} \Theta, \qquad \text{and} \qquad \vec{g}_R = \operatorname{Grad} \Theta. \tag{42}$$

Here, $\overset{\triangle}{\tilde{\varepsilon}}_{\mathrm{p}}$ and $\overset{\triangle}{\tilde{\varepsilon}}_{\mathrm{v}}$ are the covariant Oldroyd rates of the plastic and viscous strains, respectively. In the Maxwell-element, the parameter $\hat{\eta}$ represents the viscosity, which is modeled later on. The plastic element has the goal to describe a rate-independent process. To this end, the term $\overset{\triangle}{\tilde{\varepsilon}}_{\mathrm{p}}$ is defined to be proportional to the rate of the mechanical arc-length $\dot{s}_{\mathrm{M}}$

$$\dot{s}_{\mathrm{M}} = \sqrt{\overset{\triangle}{\bar{\tilde{\varepsilon}}}_{\mathrm{M}} \cdot \overset{\triangle}{\bar{\tilde{\varepsilon}}}_{\mathrm{M}}}, \tag{43}$$

with $\tilde{\varepsilon}_{\mathrm{M}} = \frac{1}{2}(\mathbf{F}_{\mathrm{k}}^{\mathrm{T}} \mathbf{F}_{\mathrm{k}} - \bar{\mathbf{F}}_{\mathrm{p}}^{-\mathrm{T}} \bar{\mathbf{F}}_{\mathrm{p}}^{-1})$ the mechanical strain expressed with quantities of the intermediate configuration $\tilde{\chi}_t$, and $\bar{\tilde{\varepsilon}}_{\mathrm{M}}$ as its isochoric part. The parameter $\beta_{\mathbf{Y}}$ from Equation (38) is defined by

$$\beta_{\mathbf{Y}} = \frac{\hat{b}}{\mu_{\mathrm{eq}}(\Theta)}, \tag{44}$$

where $\hat{b}$ is a material parameter and $\mu_{\mathrm{eq}}(\Theta)$ a function of the temperature. The derived stresses from Equation (31) and Equation (30) are inserted into Equations (38) and (39), which leads to

$$\overset{\triangle}{\tilde{\varepsilon}}_{\mathrm{p}} = 2\mu_{\mathrm{eq}} \beta_{\mathbf{Y}} (\varphi_{\Theta} \varphi_a)^{-2} \dot{s}_{\mathrm{M}} \bar{\mathbf{C}}_{\mathrm{k}}^{\mathrm{D}}, \tag{45}$$

$$\overset{\triangle}{\tilde{\varepsilon}}_{\mathrm{v}} = \frac{2\mu_{\mathrm{ov}}}{\hat{\eta}} (\varphi_{\Theta} \varphi_a)^{-2} \bar{\mathbf{C}}_{\mathrm{e}}^{\mathrm{D}}. \tag{46}$$

With a pull-back operation and considering the relations $\mathbf{F}_{\mathrm{M}} = \mathbf{F}_{\mathrm{e}} \bar{\mathbf{F}}_{\mathrm{v}} = \mathbf{F}_{\mathrm{k}} \bar{\mathbf{F}}_{\mathrm{p}}$ and $\bar{\mathbf{C}}_{\mathrm{M}} = \bar{\mathbf{C}} = J^{-2/3} \mathbf{C}$, these equations can be expressed with quantities relative to the reference configuration

$$\dot{\mathbf{C}}_{\mathrm{p}} = 4(\varphi_a \varphi_{\Theta})^{-2} J^{-2/3} \beta_{\mathbf{Y}} \mu_{\mathrm{eq}} \dot{s}_{\mathrm{M}} \bar{\mathbf{C}}_{\mathrm{p}} (\bar{\mathbf{C}}_{\mathrm{p}}^{-1} \mathbf{C})^{\mathrm{D}}, \tag{47}$$

$$\dot{\mathbf{C}}_{\mathrm{v}} = \frac{4\mu_{\mathrm{ov}}}{\hat{\eta}} (\varphi_a \varphi_{\Theta})^{-2} J^{-2/3} \bar{\mathbf{C}}_{\mathrm{v}} (\bar{\mathbf{C}}_{\mathrm{v}}^{-1} \mathbf{C})^{\mathrm{D}}. \tag{48}$$

The tensors $\bar{\mathbf{C}}_{\mathrm{p}} (\bar{\mathbf{C}}_{\mathrm{p}}^{-1} \mathbf{C})^{\mathrm{D}}$ and $\bar{\mathbf{C}}_{\mathrm{v}} (\bar{\mathbf{C}}_{\mathrm{v}}^{-1} \mathbf{C})^{\mathrm{D}}$ are symmetric since they can be expressed by the sum of symmetric tensors

$$\bar{\mathbf{C}}_{\mathrm{p}} (\bar{\mathbf{C}}_{\mathrm{p}}^{-1} \mathbf{C})^{\mathrm{D}} = \bar{\mathbf{C}}_{\mathrm{p}} \left(\bar{\mathbf{C}}_{\mathrm{p}}^{-1} \mathbf{C} - \frac{1}{3} (\operatorname{tr} (\bar{\mathbf{C}}_{\mathrm{p}}^{-1} \mathbf{C}) \mathbf{I}) \right) = \mathbf{C} - \frac{1}{3} (\operatorname{tr} (\bar{\mathbf{C}}_{\mathrm{p}}^{-1} \mathbf{C})) \bar{\mathbf{C}}_{\mathrm{p}}, \tag{49}$$

$$\bar{\mathbf{C}}_{\mathrm{v}} (\bar{\mathbf{C}}_{\mathrm{v}}^{-1} \mathbf{C})^{\mathrm{D}} = \bar{\mathbf{C}}_{\mathrm{v}} \left(\bar{\mathbf{C}}_{\mathrm{v}}^{-1} \mathbf{C} - \frac{1}{3} (\operatorname{tr} (\bar{\mathbf{C}}_{\mathrm{v}}^{-1} \mathbf{C}) \mathbf{I}) \right) = \mathbf{C} - \frac{1}{3} (\operatorname{tr} (\bar{\mathbf{C}}_{\mathrm{v}}^{-1} \mathbf{C})) \bar{\mathbf{C}}_{\mathrm{v}}. \tag{50}$$

To determine the rate of the arc-length $\dot{s}_{\mathrm{M}}$ in dependence of the variables of the reference configuration, the isochoric mechanical strain rate $\overset{\triangle}{\bar{\tilde{\varepsilon}}}_{\mathrm{M}}$ is considered first

$$\overset{\triangle}{\bar{\tilde{\varepsilon}}}_{\mathrm{M}} = \bar{\mathbf{F}}_{\mathrm{p}}^{-\mathrm{T}} \dot{\bar{\mathbf{E}}}_{\mathrm{M}} \bar{\mathbf{F}}_{\mathrm{p}}^{-1}. \tag{51}$$

The isochoric strain rate is equal to

$$\dot{\bar{\mathbf{E}}}_{\mathrm{M}} = \frac{J^{-2/3}}{2}\mathbf{C}(\mathbf{C}^{-1}\dot{\mathbf{C}})^{\mathrm{D}}. \tag{52}$$

Thus, considering Equation (52), the rate of the arc-length $\dot{s}_{\mathrm{M}}$ is given by

$$\dot{s}_{\mathrm{M}} = \sqrt{\overset{\triangle}{\bar{\bar{\boldsymbol{\varepsilon}}}}_{\mathrm{M}} \cdot \overset{\triangle}{\bar{\bar{\boldsymbol{\varepsilon}}}}_{\mathrm{M}}} = \frac{J^{-2/3}}{2}\sqrt{\bar{\mathbf{C}}_{\mathrm{p}}^{-1}\mathbf{C}(\mathbf{C}^{-1}\dot{\mathbf{C}})^{\mathrm{D}}\bar{\mathbf{C}}_{\mathrm{p}}^{-1} \cdot \mathbf{C}(\mathbf{C}^{-1}\dot{\mathbf{C}})^{\mathrm{D}}}. \tag{53}$$

The following evolution equation is chosen for the softening variable k similarly to the small deformations case, see [3],

$$\dot{k} = \alpha_k(1-k)\dot{s}_{\mathrm{M}}. \tag{54}$$

The softening is a growing rate-independent variable with values between 0 and 1. The value 0 correspond to the initial, undeformed state and 1 the state, in which the maximal softening is reached. Finally, an evolution equation for the aging variable a has to be found. From Equations (41) and (A68), one obtains

$$\dot{a} = \beta_a\left(C_2 + \varphi_a\varphi_\Theta^2\frac{\partial\varphi_a}{\partial a}(\mathrm{tr}\,\mathbf{S}_{\mathrm{M}})\right). \tag{55}$$

The aging rate is proportional to a parameter C_2 and a term depending on the trace of the stress $\mathbf{S}_{\mathrm{M}}$. The sign of $\mathrm{tr}\,\mathbf{S}_{\mathrm{M}}$ determines whether the aging process is accelerated or decelerated. A negative aging rate would correspond to a reversible aging process, which is physically unrealistic. Because of that, the term C_2 has to be larger than $\varphi_a\varphi_\Theta^2(\partial\varphi_a/\partial a)(\mathrm{tr}\,\mathbf{S}_{\mathrm{M}})$. At the moment, the literature offers no information that allows to quantify the influence of mechanical deformation or stresses on the aging process of die casting alloys. The microstructure of a ZnAl20.2Cu1.8 alloy after a tensile test was investigated with X-ray diffraction and SEM in [24]. Here, it was observed that the tensile stress was associated to microstructural changes such as phase transformations. Zhu [13] concluded that stresses accelerate the decomposition of metastable phases in tensile tests. Unfortunately, the studies were performed at temperatures over 100 °C and the microstructural changes were not quantified. There is also no information about the compression or torsion behavior. Moreover, Deschamps et al. [66] and Cerri and Leo [67] found an increase in the aging rate with the plastic deformation for aluminum alloys. Since aging takes place in a much larger timescale than the mechanical processes in the application range of the alloy and since there is no information at hand to characterize the influence of the stress on aging, we assume that the term C_2 is much larger than $\varphi_a\varphi_\Theta^2(\partial\varphi_a/\partial a)(\mathrm{tr}\,\mathbf{S}_{\mathrm{M}})$, analogously to the discussion in Lion et al. [68] for the field of curing or, more recently, in [4]. Thus, the following expression is considered

$$\dot{a} \approx \beta_a C_2. \tag{56}$$

In order to describe the aging state of the material, the aging variable is defined as a process variable with values between 0 an 1. The value 0 corresponds to the initial unaged stage, while 1 represents the completely aged material. In the measurements of Figure 5 one can see that the isothermal aging process is stronger at the beginning of the process and decelerates when approaching saturation and occurs faster at higher temperatures. In order to fulfill these criteria, the function

$$\beta_a(\Theta, a) = \frac{\beta_{a1}(\Theta)}{C_2}\frac{(1-a)}{(\beta_{a2}+a)}, \tag{57}$$

is proposed, see also [4]. The function $\beta_{a1}(\Theta)$ includes the temperature dependence in the development of the aging. An Arrhenius ansatz is chosen for this function, which

is a common approach for temperature-driven diffusion processes in metals. Thus, the evolution equation of the aging variable reads

$$\dot{a} = \beta_{a1}(\Theta)\frac{1-a}{\beta_{a2}+a}, \qquad \beta_{a1}(\Theta) = \beta_{a11}\exp(-\beta_{a12}/\Theta), \tag{58}$$

with $\beta_{a12} = E_a/R$, E_a is the activation energy and R the universal gas constant.

3.2. Functions for the Material Parameters

Based on the developed functions for the small deformation case, see [3,4], the functions $\mu_{\mathrm{eq}}(\Theta)$, $\eta(\dot{\mathbf{C}}, \mathbf{C}, \Theta, \bar{\mathbf{C}}_{\mathrm{p}}, a)$, and $\mu_{\mathrm{ov}}(k)$ are adapted. The change in the initial slope of the plastic equilibrium stress is modeled by the parameter $\mu_{\mathrm{eq}}(\Theta)$, analogously to the parameter $c(\Theta)$ in the small deformation model in [3]

$$\mu_{\mathrm{eq}}(\Theta) = \hat{c}_1(\hat{c}_2 - \tanh(\hat{c}_3(\Theta - \hat{\Theta}_c))). \tag{59}$$

The following expression is chosen for the shear modulus of the overstress μ_{ov} depending on the softening variable k

$$\mu_{\mathrm{ov}}(k) = \hat{G}_0((1-k)^{\hat{n}_{\mathrm{ov}}} + \hat{\alpha}_{\mathrm{ov}}). \tag{60}$$

The viscosity is modeled by

$$\hat{\eta}(\dot{\mathbf{C}}, \mathbf{C}, \Theta, \bar{\mathbf{C}}_{\mathrm{p}}, a) = \hat{\eta}_0(\Theta, a)\left(\left(\frac{1}{s_\eta}\dot{s}_{\mathrm{M}}(\dot{\mathbf{C}}, \mathbf{C}, \Theta, \bar{\mathbf{C}}_{\mathrm{p}}, a) + \hat{\alpha}_\eta(\Theta)\right)^{-\hat{r}_\eta(\Theta)} + 1\right), \tag{61}$$

and depends on the right Cauchy-Green tensor $\mathbf{C}$, the plastic right Cauchy-Green tensor $\bar{\mathbf{C}}_{\mathrm{p}}$, the aging a, and the temperature Θ considering the dependencies of the variable $\dot{s}_{\mathrm{M}}(\dot{\mathbf{C}}, \mathbf{C}, \Theta, \bar{\mathbf{C}}_{\mathrm{p}}, a)$. The temperature and aging-dependent functions were modeled during the identification step

$$\hat{\eta}_0(\Theta, a) = (\hat{\eta}_{01} - \hat{\eta}_{02}\exp(\hat{\eta}_{03}a))(1 + \tanh(\hat{n}_\eta(\Theta - \hat{\Theta}_\eta))), \tag{62}$$

$$\hat{r}_\eta(\Theta) = \hat{r}_{\eta 1}(1 - \tanh(\hat{n}_\eta(\Theta - \hat{\Theta}_r))), \tag{63}$$

$$\hat{\alpha}_\eta(\Theta) = \hat{\alpha}_{\eta 1}\exp(\hat{\alpha}_{\eta 2}\Theta). \tag{64}$$

A summary of the entire model is presented in Table 1.

Table 1. Summary of the constitutive model (the equation numbers are related to the specified equations).

Kinematic	
$\mathbf{F} = \mathbf{F}_a\mathbf{F}_\Theta\mathbf{F}_{\mathrm{M}} = \mathbf{F}_a\mathbf{F}_\Theta\mathbf{F}_{\mathrm{k}}\bar{\mathbf{F}}_{\mathrm{p}} = \mathbf{F}_a\mathbf{F}_\Theta\mathbf{F}_{\mathrm{e}}\bar{\mathbf{F}}_{\mathrm{v}}, \quad J = \det\mathbf{F}$	(2),(9),(10)
$\mathbf{F}_\Theta = \varphi_\Theta(\Theta)\mathbf{I}, \quad \mathbf{F}_a = \varphi_a(a)\mathbf{I}, \quad J_{\mathrm{M}} = (\varphi_a(a)\varphi_\Theta(\Theta))^{-3}J$	(3)
2nd Piola-Kirchhoff stresses in the reference configuration	
$\tilde{\mathbf{T}} = \tilde{\mathbf{T}}_{\mathrm{eq}} + \tilde{\mathbf{T}}_{\mathrm{ov}} = \tilde{\mathbf{T}}^{\mathrm{e}}_{\mathrm{eq}} + \tilde{\mathbf{T}}^{\mathrm{h}}_{\mathrm{eq}} + \tilde{\mathbf{T}}_{\mathrm{ov}}$	(1)
$\tilde{\mathbf{T}}^{\mathrm{e}}_{\mathrm{eq}} = \frac{K}{10}\left(J_{\mathrm{M}}^5 - J_{\mathrm{M}}^{-5}\right)\mathbf{C}^{-1} + 2c_{10}J^{-2/3}\mathbf{C}^{-1}\mathbf{C}^{\mathrm{D}}$	(A57),(A58)
$\tilde{\mathbf{T}}^{\mathrm{h}}_{\mathrm{eq}} = 2\mu_{\mathrm{eq}}(\Theta)J^{-2/3}\mathbf{C}^{-1}(\mathbf{C}\bar{\mathbf{C}}_{\mathrm{p}}^{-1})^{\mathrm{D}}$	(A64)
$\tilde{\mathbf{T}}_{\mathrm{ov}} = 2\mu_{\mathrm{ov}}(k)J^{-2/3}\mathbf{C}^{-1}(\mathbf{C}\bar{\mathbf{C}}_{\mathrm{v}}^{-1})^{\mathrm{D}}$	(A65)

Table 1. *Cont.*

Kirchhoff stresses in the current configuration	
$\mathbf{S} = \mathbf{S}^{\mathrm{e}}_{\mathrm{vol}} + \mathbf{S}^{\mathrm{e}}_{\mathrm{iso}} + \mathbf{S}^{\mathrm{h}}_{\mathrm{eq}} + \mathbf{S}_{\mathrm{ov}}$	
$\mathbf{S}^{\mathrm{e}}_{\mathrm{vol}} = \frac{K}{10}\left(J_{\mathrm{M}}^{5} - J_{\mathrm{M}}^{-5}\right)\mathbf{I}, \quad \mathbf{S}^{\mathrm{e}}_{\mathrm{iso}} = 2c_{10}\bar{\mathbf{B}}^{\mathrm{D}}_{\mathrm{M}}$	(A59),(A60)
$\mathbf{S}^{\mathrm{h}}_{\mathrm{eq}} = 2\mu_{\mathrm{eq}}(\Theta)\bar{\mathbf{B}}^{\mathrm{D}}_{\mathrm{k}}$	(A66)
$\mathbf{S}_{\mathrm{ov}} = 2\mu_{\mathrm{ov}}(k)\bar{\mathbf{B}}^{\mathrm{D}}_{\mathrm{e}}$	(A67)
Evolution equations in the reference configuration	
$\dot{\mathbf{C}}_{\mathrm{p}} = 4(\varphi_a(a)\varphi_\Theta(\Theta))^{-2}J^{-2/3}\,\hat{b}\,\dot{s}_{\mathrm{M}}\bar{\mathbf{C}}_{\mathrm{p}}(\bar{\mathbf{C}}_{\mathrm{p}}^{-1}\mathbf{C})^{\mathrm{D}}$	(49)
$\dot{\mathbf{C}}_{\mathrm{v}} = \frac{4\mu_{\mathrm{ov}}(k)}{\hat{\eta}(\dot{\mathbf{C}},\mathbf{C},\Theta,\bar{\mathbf{C}}_{\mathrm{p}},a)}(\varphi_a(a)\varphi_\Theta(\Theta))^{-2}J^{-2/3}\bar{\mathbf{C}}_{\mathrm{v}}(\bar{\mathbf{C}}_{\mathrm{v}}^{-1}\mathbf{C})^{\mathrm{D}}$	(50)
$\dot{a} = \beta_{a1}(\Theta)\frac{1-a}{\beta_{a2}+a}$	(58)
$\dot{k} = \alpha_k(1-k)\dot{s}_{\mathrm{M}}$	(54)
$\dot{s}_{\mathrm{M}} = J^{-2/3}/2\sqrt{\bar{\mathbf{C}}_{\mathrm{p}}^{-1}\mathbf{C}(\mathbf{C}^{-1}\dot{\mathbf{C}})^{\mathrm{D}}\bar{\mathbf{C}}_{\mathrm{p}}^{-1}\cdot\mathbf{C}(\mathbf{C}^{-1}\dot{\mathbf{C}})^{\mathrm{D}}}$	(53)
Temperature, softening and aging-dependent functions	
$\beta_{a1}(\Theta) = \beta_{a11}\exp(-\beta_{a12}/\Theta)$	(58)
$\mu_{\mathrm{eq}}(\Theta) = \hat{c}_1(\hat{c}_2 - \tanh(\hat{c}_3(\Theta - \hat{\Theta}_c)))$	(59)
$\mu_{\mathrm{ov}}(k) = \hat{G}_0((1-k)^{\hat{n}_{\mathrm{ov}}} + \hat{\alpha}_{\mathrm{ov}})$	(60)
$\hat{\eta}(\dot{\mathbf{C}},\mathbf{C},\Theta,\bar{\mathbf{C}}_{\mathrm{p}},a) = \hat{\eta}_0(\Theta,a)\left(\left(\frac{\dot{s}_{\mathrm{M}}}{s_\eta} + \hat{\alpha}_\eta(\Theta)\right)^{-\hat{r}_\eta(\Theta)} + 1\right)$	(61)
$\hat{\eta}_0(\Theta,a) = (\hat{\eta}_{01} - \hat{\eta}_{02}\exp(\hat{\eta}_{03}a))(1 + \tanh(\hat{n}_\eta(\Theta - \hat{\Theta}_\eta)))$	(62)
$\hat{r}_\eta(\Theta) = \hat{r}_{\eta1}(1 - \tanh(\hat{n}_\eta(\Theta - \hat{\Theta}_r)), \quad \hat{\alpha}_\eta(\Theta) = \hat{\alpha}_{\eta1}\exp(\hat{\alpha}_{\eta2}\Theta)$	(63),(64)
$\varphi_\Theta(\Theta) = 1 + \alpha_\Theta(\Theta - \Theta_0), \quad \varphi_a(a) = 1 - \alpha_a$	(4),(5)

3.3. Modeling of the Thermo-Physical Properties

For the computation of coupled thermo-mechanical problems, expressions for the specific heat capacity c_{p} and thermal conductivity κ_Θ are necessary. For the development of these functions for Zamak 5, the measurements from [33] are taken into account. The linear thermal expansion α_Θ was already defined in Equation (4), with the selection of the thermal part of the deformation gradient $\mathbf{F}_\Theta$.

3.3.1. Specific Heat Capacity

From the considerations in the Clausius-Duhem inequality, see Appendix C, there is a relationship between the specific heat capacity and the specific free energy. Equation (28) results in a linear behavior over the temperature for the specific heat c_{p}

$$c_{\mathrm{p}}(\Theta) = c_{\mathrm{p1}}(1 + c_{\mathrm{p2}}(\Theta - \Theta_0)). \tag{65}$$

Here, c_{p1} and c_{p2} are material parameters, and Θ_0 is the reference temperature.

3.3.2. Thermal Diffusivity

Considering the measurements of the thermal diffusivity in [33], it can be seen that the thermal diffusivity depends on the temperature and the aging variable. In order to model this behavior, a weighting between the initial unaged stage $\hat{\lambda}_0(\Theta)$ and the final stage $\hat{\lambda}_\infty(\Theta)$ is carried out with the help of a weighting function $f_{\hat{\lambda}}(\Theta,a)$

$$\hat{\lambda}(\Theta,a) = \hat{\lambda}_\infty(\Theta)f_{\hat{\lambda}}(\Theta,a) + \hat{\lambda}_0(\Theta)(1 - f_{\hat{\lambda}}(\Theta,a)). \tag{66}$$

A linear behavior over the temperature is observed for the completely aged state, see Figure 15,

$$\hat{\lambda}_\infty(\Theta) = \hat{\lambda}_{\infty 1} - \hat{\lambda}_{\infty 2}\Theta. \tag{67}$$

As one can see in Figure 15, the initial state shows a constant behavior up to the temperature of $\Theta_0 = 293.15\,\mathrm{K}$. After that, an approximately linear reduction is observed. In order to model this behavior, the following function is chosen

$$\hat{\lambda}_0(\Theta) = \hat{\lambda}_{01} - \hat{\lambda}_{02}(1 + \tanh(\Theta - \Theta_0))(\Theta - \Theta_0). \tag{68}$$

For the weighting factor $f_{\hat{\lambda}}$ from Equation (66) we chose a function of the aging and temperature, which has a growing behavior with the aging. It has values between 0 and 1, where 0 corresponds to the unaged state and 1 to the completely aged state

$$f_{\hat{\lambda}}(\Theta, a) = a - \alpha_{\hat{\lambda}}(\Theta)(1-a)a^2, \qquad \alpha_{\hat{\lambda}}(\Theta) = \alpha_{\hat{\lambda}1}\exp(-\alpha_{\hat{\lambda}2}\Theta). \tag{69}$$

This expression was chosen during the identification.

3.3.3. Thermal Conductivity

The thermal conductivity can be obtained from the relation

$$\kappa_\Theta(\Theta, a) = \rho\hat{\lambda}(\Theta, a)c_\mathrm{p}(\Theta). \tag{70}$$

With the proposed expressions for the thermal diffusivity and the specific heat capacity, the thermal conductivity is equal to

$$\kappa_\Theta(\Theta, a) = \rho c_{\mathrm{p}1}(1 + c_{\mathrm{p}2}(\Theta - \Theta_0))(\hat{\lambda}_\infty(\Theta)f_{\hat{\lambda}}(\Theta, a) + \hat{\lambda}_0(\Theta)(1 - f_{\hat{\lambda}}(\Theta, a))), \tag{71}$$

with the functions $\hat{\lambda}_\infty$, $\hat{\lambda}_0$ and $f_{\hat{\lambda}}$ from Equations (67)–(69).

4. Parameter Identification

The parameter identification in performed in several steps, where each phase considers a different phenomenon. First, the aging variable is considered using the shrinkage measurements. Second, the identification of the mechanical part of the model is performed in a partitioned way. The parameters of the equilibrium stress state are identified first using the termination points of the relaxation. Once these parameters are known, the parameters of the overstress part are identified with the help of the experiments at different strain rates. In the final step, the thermo-physical properties are identified.

4.1. Identification of the Aging Variable

The material parameters related to the aging variable can be identified with the measurements of the shrinkage considering the evolution Equation (58) and the relation of the stretch due to aging $\lambda_a = \varphi_a = 1 - \alpha_a a = L/L_0$. Here, the parameter α_a corresponds to the maximum shrinkage reached by the material. The parameters responsible for the development of the aging over time are β_{a11}, β_{a12} and β_{a2}, see Equation (58). In a first identification step, the parameters α_a, β_{a2} and β^i_{a1}, are identified, with β^i_{a1}, $i = 1, 2, 3$, changing for every temperature $\Theta_1 = 85\,^\circ\mathrm{C}$, $\Theta_2 = 105\,^\circ\mathrm{C}$, $\Theta_3 = 125\,^\circ\mathrm{C}$. The results of this first identification are used in a subsequent second identification step. Here, the parameters of the Arrhenius equation, β_{a11} and β_{a12}, are identified. To this end, we consider the natural logarithm of Equation (57)

$$\ln\beta_{a1}(\Theta) = \ln(\beta_{a11}) - \beta_{a12}\frac{1}{\Theta}. \tag{72}$$

Equation (72) corresponds to a linear equation $y(x) = y_0 - mx$, with $y(x) = \ln\beta_{a1}$ in dependence of $x = 1/\Theta$. The parameters $y_0 = \ln(\beta_{a11})$ and $m = \beta_{a12}$ were found with the

help of the points β^i_{a1} obtained in the previous identification step. The results of the second identification are shown in Figure 8 and Table 2. In Figure 8b one can see the prediction of the model (brown line) at the temperature of 20 °C compared to the measurement from [8] (points). The black line represents the response of the model at 20 °C with the identified parameters but with a change in the saturation value α_a, where the value identified in [4] is used, since it is clear that the saturation value in the measurement shown in [8] is different. Here, one can see that—although their saturation value α_a is different—the process for the evolution of the aging variable represented by the parameters β_{a2}, β_{a11}, and β_{a12} corresponds to the measurements of [8].

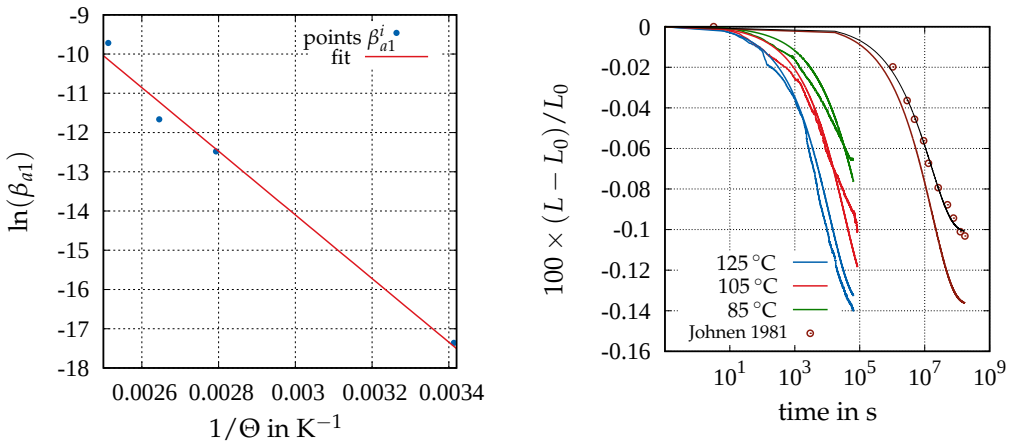

(**a**) (**b**)

Figure 8. Results of the identification of the aging variable. (**a**) Identification of the parameter $\beta_{a1}(\Theta)$. (**b**) Identification results of the shrinkage experiments and prediction of the model at room temperature. Comparison with the measurement from [8].

Table 2. Parameter identification of the Arrhenius equation.

Parameter	α_a —	$\ln(\beta_{a11})$ —	β_{a12} K
initial value	10^{-3}	10^{-3}	1
final value	1.37×10^{-3}	10.24	8113
conf. interval	10^{-7}	0.787	2748

In Figure 8, it is shown that the model can reproduce the main behavior of the experiments. The small values of the function β_{a1} for temperatures below 80 °C indicate that the aging process happens quite slowly.

4.2. Identification of the Mechanical Response

Contrarily to the small deformations model from [3,4], the case of torsion is not purely deviatoric for finite deformation, since there is a reaction force in longitudinal direction. Thus, the uniaxial tension/compression experiments are used in the identification with the help of the procedure exposed in [69]. The modular structure of the model is drawn on for material parameter identification. First, the parameters of the equilibrium stress state are identified with the equilibrium hysteresis and after that, the overstress with the experiments at different strain rates and multi-step relaxation tests are determined.

4.2.1. Elastic Part of the Equilibrium Stress State

The two parameters K and c_{10} of the elastic equilibrium stress state, see Equations (A59) and (A60), are not influenced by aging or temperature and are taken from the small defor-

mations case in [3] to prevent a correlation between the parameters during the identification process

$$K = K_{\mathrm{eq}} = 49.5\,\mathrm{GPa}, \qquad c_{10} = G_{\mathrm{eq}}/2 = 0.05\,\mathrm{GPa}. \tag{73}$$

The parameter c_{10} corresponds to the shear modulus of the elastic equilibrium stress state and it is proportional to G_{eq}, see [3].

4.2.2. Hysteretic Part of the Equilibrium Stress State

The material parameters of the hysteretic part of the equilibrium stress state $\boldsymbol{\kappa} = \{\hat{b}, \hat{c}_1, \hat{c}_2, \hat{c}_3, \hat{\Theta}_c\}$ from Equation (59), are identified at the termination points of relaxation of multi-step relaxation processes in tension and compression at different temperatures. Table 3 and Figure 9 display the results of the identification. Here, the axial component of 1st Piola-Kirchhoff tensor (axial force per cross section in the undeformed state) is represented by σ_R and the axial stretch by λ. The initial values for the non-linear optimizer are given by the model for small strains. The confidence intervals are sufficiently small for all material parameters.

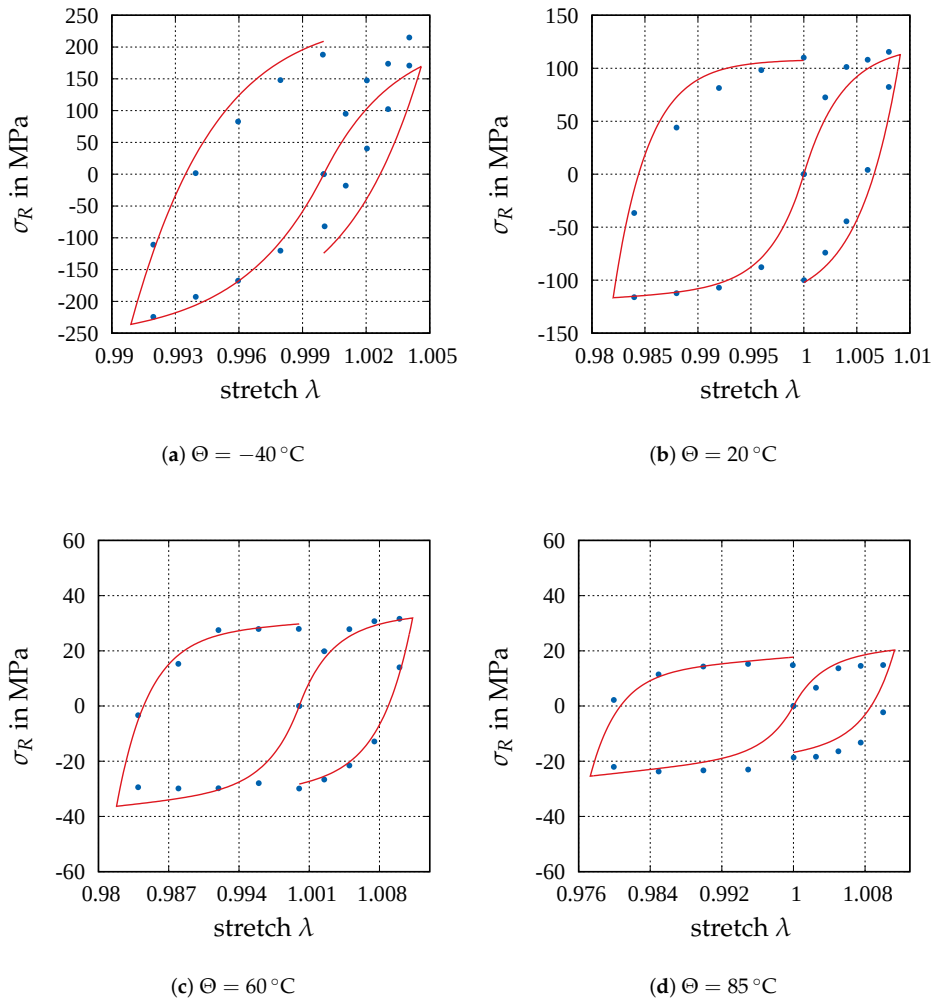

(**a**) $\Theta = -40\,^{\circ}\mathrm{C}$ (**b**) $\Theta = 20\,^{\circ}\mathrm{C}$

(**c**) $\Theta = 60\,^{\circ}\mathrm{C}$ (**d**) $\Theta = 85\,^{\circ}\mathrm{C}$

Figure 9. Identification results in tension/compression for the equilibrium stress state for the different temperatures. The experiments are represented by points and the model with lines.

Table 3. Identified parameters of the equilibrium stress part in tension/compression.

Parameter	$\hat{b}$ –	$\hat{c}_1$ MPa	$\hat{c}_2$ MPa	$\hat{c}_3$ –	$\hat{\Theta}_c$ K
initial values	54.77	5793.5	1.1	0.24	283.44
final values	58.94	5924.8	1.12	0.0279	288.03
conf. intervals	4.14	541.5	0.02	0.0019	3.77

4.2.3. Overstress Part

The identification of the overstress part (A67), i.e., the shear modulus (60), is performed in two steps. The parameters of the shear modulus μ_{ov} and the parameters of the viscosity $\hat{\eta}$ in Equation (61) are identified first for a constant aging time considering the experiments without aging. The feature of interest here is temperature dependence. In this identification step there are 40 experimental curves in total: four different strain rates plus the multi-step relaxation test at four different temperatures and for tension and compression. In the second step, the parameters considering aging dependence are found with the experiments at different aging times. In this second identification, the temperature-dependent parameters are known.

1st Step: Shear Modulus

There are three parameters that have to be identified for the identification of the shear modulus (60), namely $\boldsymbol{\kappa} = \{\hat{G}_0, \hat{\alpha}_{\text{ov}}, \hat{n}_{\text{ov}}\}$. The parameter of the softening is set to $\alpha_k = 350$, so that it reaches the value 1 at the end of the loading process for a strain equal to 1 %. During this identification step, the value of the viscosity is identified independently for each strain rate and temperature for the material without aging.The results of the identification are shown in Table 4.

Table 4. Results of the parameter identification for μ_{ov}, see Equation (60).

Parameter	$\hat{G}_0$ MPa	$\hat{\alpha}_{\text{ov}}$ –	$\hat{n}_{\text{ov}}$ –
initial value	1.604×10^4	2×10^{-1}	3.5×10^{-1}
final value	1.424×10^4	2.531×10^{-1}	3.349×10^{-1}
conf. interval	15.3	5.71×10^{-4}	6.8×10^{-4}

2nd Step: Viscosity

The parameters of the shear modulus are assumed to be fixed for the subsequent identification step, see Table 4. The material parameters $\boldsymbol{\kappa} = \{\hat{\Theta}_\eta, \hat{r}_{\eta 1}, \hat{\Theta}_r, \hat{n}_\eta, \hat{\alpha}_{\eta 1}, \hat{\alpha}_{\eta 2}\}$ in Equations (61) and (62) have to be identified next. They are related to the temperature and rate dependence. A value for the function $\hat{\eta}_0(a = 0) = \hat{\eta}_{01} - \hat{\eta}_{02}$ of Equation (62) is identified, which is used later on in the identification of the aging dependence. The results of the identification are shown in Table 5 showing that the confidence intervals are less than one order, and appear to be sufficiently accurate considering the complexity of the model.

Table 5. Results of the parameter identification for the temperature-dependence of the viscosity.

Parameter	$\hat{\Theta}_\eta$ K	$\hat{r}_{\eta 1}$ –	$\hat{\Theta}_r$ K	$\hat{n}_\eta$ K^{-1}	$\hat{\alpha}_{\eta 1}$ –	$\hat{\alpha}_{\eta 2}$ K^{-1}
initial value	373.6	0.480	426.3	0.0115	1.26×10^{-9}	0.0135
final value	375.2	0.479	428.2	0.0117	3.47×10^{-10}	0.0173
conf. interval	0.837	2.8×10^{-4}	0.192	9.7×10^{-6}	4.80×10^{-11}	4.1×10^{-4}

The correlation matrix is equal to

$$\mathbf{R} = \begin{bmatrix} & \hat{\Theta}_\eta & \hat{r}_{\eta 1} & \hat{\Theta}_r & \hat{n}_\eta & \hat{\alpha}_{\eta 1} & \hat{\alpha}_{\eta 2} \\ \hat{\Theta}_\eta & 1 & 0.916 & -0.876 & -0.645 & 0.394 & -0.391 \\ \hat{r}_{\eta 1} & & 1 & -0.826 & -0.539 & 0.405 & -0.386 \\ \hat{\Theta}_r & & & 1 & 0.222 & -0.452 & 0.452 \\ \hat{n}_\eta & & & & 1 & -0.136 & 0.134 \\ \hat{\alpha}_{\eta 1} & & & & & 1 & -0.997 \\ \hat{\alpha}_{\eta 2} & & & & & & 1 \end{bmatrix} \tag{74}$$

showing a strong correlation between the parameters $\hat{\Theta}_\eta$, $\hat{r}_{\eta 1}$, and $\hat{\Theta}_r$, which consider the temperature dependence of the functions $\hat{\eta}_0$ and $\hat{r}_\eta$, and also between the parameters $\hat{\alpha}_{\eta 1}$ and $\hat{\alpha}_{\eta 2}$ from the function $\hat{\alpha}_\eta(\Theta)$. The latter is known for exponential functions, see [70].

The parameters of the aging dependence are identified in the last identification step. Here, the identification for the value $\hat{\eta}_0(a)$ is performed separately for each aging time. After that, the function of the aging dependence $\hat{\eta}_0(a) = \hat{\eta}_{01} - \hat{\eta}_{02}\exp(\hat{\eta}_{03}a)$ is fitted with the identified points using Matlab. Table 6 and Figure 10 show the results of this identification step.

Table 6. Results of the parameter identification for the viscosity function $\hat{\eta}_0(a)$ of Equation (62).

Parameter	$\hat{\eta}_{01}$ MPa s	$\hat{\eta}_{02}$ MPa s	$\hat{\eta}_{03}$ —
initial value	0.265	0.068	0.305
final value	1612	81.93	1.862
conf. interval	285.75	9.6	0.78

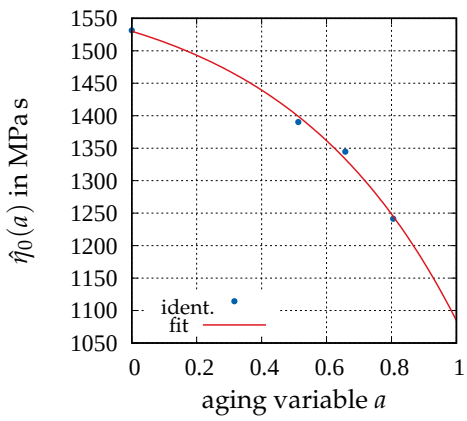

Figure 10. Identification of the aging-dependence of the viscosity function $\hat{\eta}_0(a)$.

The complete results of the identification of the temperature and the aging dependence are shown in Figures 11 and 12.

One can observe a very good agreement between the experiments and the fit for the tensile tests, and a good agreement for compression. The difference originates in the tension/compression asymmetry, which is not considered in the model. In Table 7, a summary of the identified parameters is given.

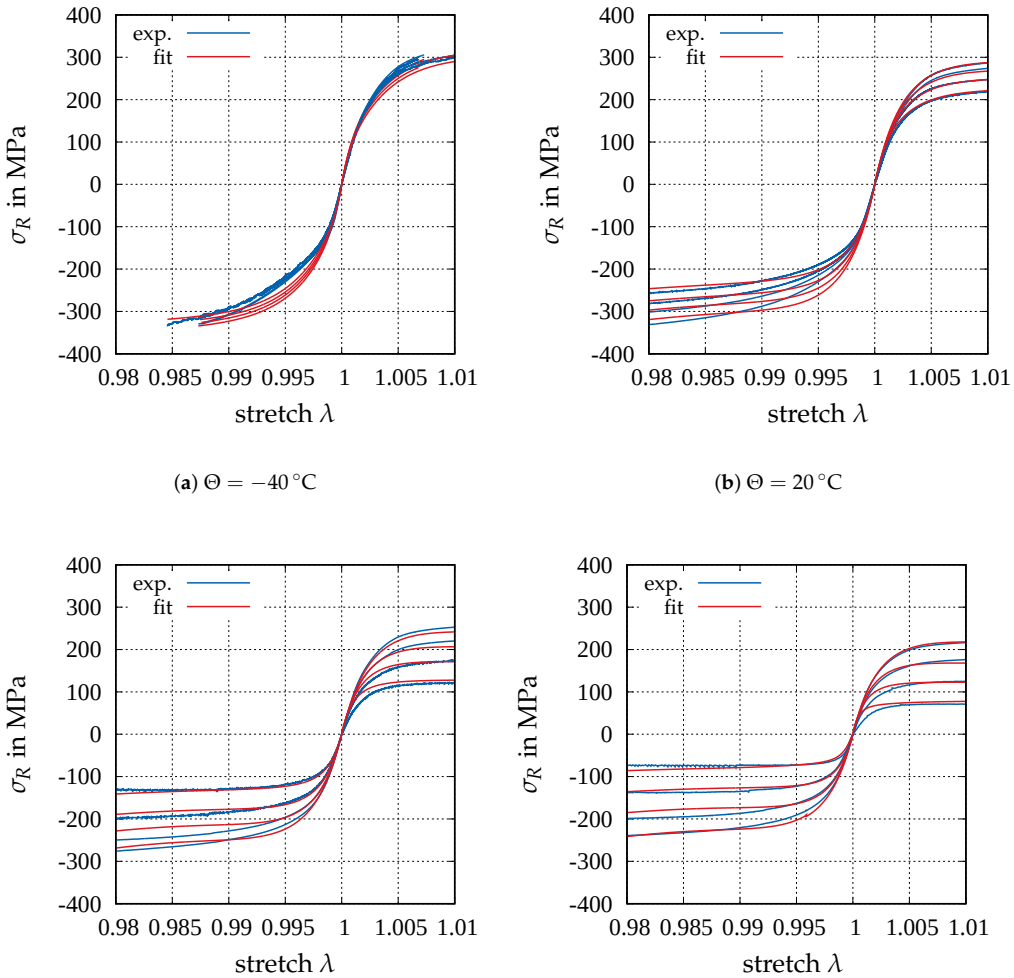

(**a**) $\Theta = -40\,^{\circ}\mathrm{C}$ (**b**) $\Theta = 20\,^{\circ}\mathrm{C}$

(**c**) $\Theta = 60\,^{\circ}\mathrm{C}$ (**d**) $\Theta = 85\,^{\circ}\mathrm{C}$

Figure 11. Identification results in tension/compression for the overstress for the different temperatures (experiments and fit without aging). Four strain rates at each constant temperature.

Table 7. Summary of the identification.

Equilibrium Stress							
parameter	K	c_{10}	$\hat{b}$	$\hat{c}_1$	$\hat{c}_2$	$\hat{c}_3$	$\hat{\Theta}_c$
value	4.95×10^4	50	58.94	5.925×10^3	1.12	0.028	288.03
dimension	MPa	MPa	–	MPa	MPa	K^{-1}	K

Shear Modulus Overstress				
parameter	$\hat{\alpha}_k$	$\hat{G}_0$	$\hat{\alpha}_{\mathrm{ov}}$	$\hat{n}_{\mathrm{ov}}$
value	350	1.424×10^4	0.253	0.335
dimension	–	MPa	–	–

Viscosity									
parameter	$\hat{\eta}_{01}$	$\hat{\eta}_{02}$	$\hat{\eta}_{03}$	$\hat{\Theta}_\eta$	$\hat{r}_{\eta 1}$	$\hat{\Theta}_r$	$\hat{n}_\eta$	$\hat{\alpha}_{\eta 1}$	$\hat{\alpha}_{\eta 2}$
value	1612	81.93	1.862	375.2	0.479	428.2	0.012	3.47×10^{-10}	0.0173
dimension	MPa s	MPa s	–	K	–	K	K^{-1}	–	K^{-1}

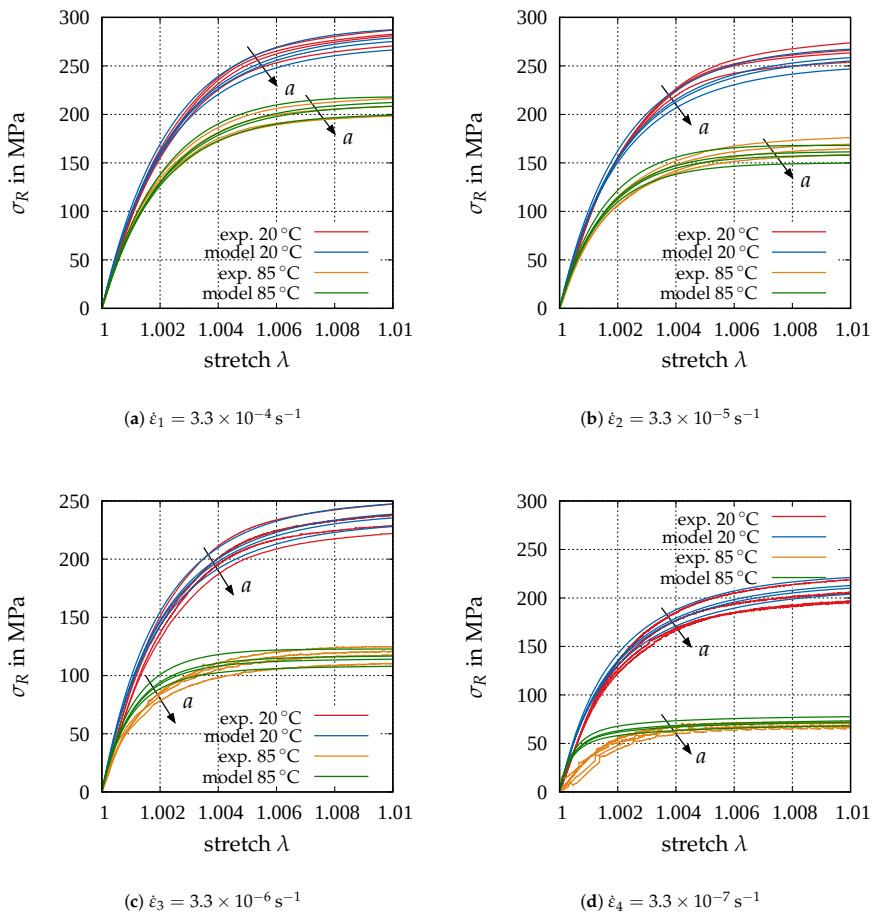

(**a**) $\dot{\varepsilon}_1 = 3.3 \times 10^{-4}\,\mathrm{s}^{-1}$ (**b**) $\dot{\varepsilon}_2 = 3.3 \times 10^{-5}\,\mathrm{s}^{-1}$

(**c**) $\dot{\varepsilon}_3 = 3.3 \times 10^{-6}\,\mathrm{s}^{-1}$ (**d**) $\dot{\varepsilon}_4 = 3.3 \times 10^{-7}\,\mathrm{s}^{-1}$

Figure 12. Identification results for the aging dependence. Experiments and fit at two different temperatures for all strain rates and aging times. The arrow points in the direction of growing aging times.

4.3. Identification of the Thermo-Physical Properties

4.3.1. Thermal Expansion

The thermal expansion coefficient was identified in [3] equal to $\alpha_\Theta = 2.8109 \times 10^{-5}\,\mathrm{K}^{-1}$, with the reference temperature $\Theta_0 = 20\,°\mathrm{C}/293.15\,\mathrm{K}$, see Figure 13a.

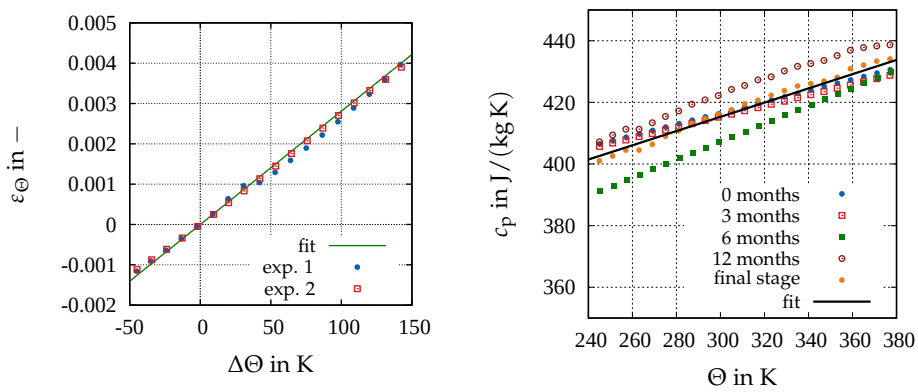

(**a**) (**b**)

Figure 13. Results of the identification for the thermal expansion and the specific hear capacity. (**a**) Thermal expansion, $\Theta_0 = 20\,°\mathrm{C}/293.15\,\mathrm{K}$. (**b**) Specific heat capacity over the temperature for different aging times.

4.3.2. Specific Heat Capacity

The parameters of the specific heat capacity of Equation (65) are identified with the measurements of [33]. The identified parameters are $c_{p1} = 413.724\,\mathrm{J\,kg^{-1}K^{-1}}$ and $c_{p2} = 5.581 \times 10^{-4}\,\mathrm{K^{-1}}$, see Figure 13b.

4.3.3. Thermal Diffusivity

The identification of the thermal diffusivity is connected to the modeling and is carried out in two steps. In Equation (66), the thermal diffusivity is expressed as a weighting between the initial unaged stage $\hat{\lambda}_0(\Theta)$ and the final stage $\hat{\lambda}_\infty(\Theta)$ by means of a weighting factor $f_{\hat{\lambda}}(\Theta, a)$

The first step of the identification considers the initial and final state of the thermal diffusivity, for which the weighting factor is known (for the initial state $f_{\hat{\lambda}}(\Theta, a = 0) = 0$ and for the final state $f_{\hat{\lambda}}(\Theta, a = 1) = 1$). In the second step the weighting factor $f_{\hat{\lambda}}(\Theta, a)$ is unknown and has to be determined.

Thus, the functions $\hat{\lambda}_0(\Theta)$ and $\hat{\lambda}_\infty(\Theta)$ are considered first, which have a total number of four parameters to be identified $\boldsymbol{\kappa}^{\mathrm{T}} = \{\hat{\lambda}_{\infty 1}, \hat{\lambda}_{\infty 2}, \hat{\lambda}_{01}, \hat{\lambda}_{02}\}$. The parameter Θ_0 corresponds to the reference temperature and is set to $\Theta_0 = 293.15\,\mathrm{K}$,

The identification of these parameter is carried out with the measurements over the temperature for the unaged specimen ($f_{\hat{\lambda}}(\Theta, a = 0) = 0$) and the completely aged specimen ($f_{\hat{\lambda}}(\Theta, a = 1) = 1$). Table 8 and Figure 15 display the results of this identification. In Figure 15, the results correspond to the initial and final state (black and blue lines).

Table 8. Results of the parameter identification of the functions $\hat{\lambda}_0(\Theta)$ and $\hat{\lambda}_\infty(\Theta)$.

Parameter	$\hat{\lambda}_{\infty 1}$ $\mathrm{mm^2\,s^{-1}}$	$\hat{\lambda}_{\infty 2}$ $\mathrm{mm^2\,s^{-1}\,K^{-1}}$	$\hat{\lambda}_{01}$ $\mathrm{mm^2\,s^{-1}}$	$\hat{\lambda}_{02}$ $\mathrm{mm^2\,s^{-1}\,K^{-1}}$
initial value	1	1	42	5×10^{-3}
final value	55.07	2.92×10^{-2}	41.74	4.63×10^{-3}
conf. interval	0.345	0.12×10^{-2}	0.074	1.2×10^{-3}

In the second identification step, a function for the weighting factor $f_{\hat{\lambda}}(\Theta, a)$ is developed. To this end, an experimental value for $f_{\hat{\lambda}\mathrm{exp}}$ is calculated with the help of Equation (66) using the experimental points by

$$f_{\hat{\lambda}\mathrm{exp}}(\Theta_i, a_j) = \frac{\hat{\lambda}_{\mathrm{exp}}(\Theta_i, a_j) - \hat{\lambda}_{\mathrm{exp}}(\Theta_i, 0)}{\hat{\lambda}_{\mathrm{exp}}(\Theta_i, 1) - \hat{\lambda}_{\mathrm{exp}}(\Theta_i, 0)}, \tag{75}$$

where $\hat{\lambda}_{\mathrm{exp}}(\Theta_i, a_j)$ represents the measured point at the temperature Θ_i and the aging time a_j, $\hat{\lambda}_{\mathrm{exp}}(\Theta_i, 0)$ denotes the initial state ($a = 0$), and $\hat{\lambda}_{\mathrm{exp}}(\Theta_i, 1)$ is the final state ($a = 1$). The function $f_{\hat{\lambda}\mathrm{exp}}$ is determined for the temperatures from $-60\,^\circ\mathrm{C}$ to $20\,^\circ\mathrm{C}$, since one can assume that the aging does not evolve during the time of the experiments for these temperatures. These experimental points are used to develop the function for the weighting factor.

In the identification, the factor is determined independently for each temperature $f_{\hat{\lambda}}(\hat{\Theta} = \mathrm{const.}, a)$. Afterwards, the function $\alpha_{\hat{\lambda}}(\Theta)$ is fitted to the results of this pre-identification, obtaining the values $\alpha_{\hat{\lambda}1} = 7.093$ (conf. int. 1) and $\alpha_{\hat{\lambda}2} = 4.937 \times 10^{-3}\,\mathrm{K^{-1}}$ (conf. int. $2.301 \times 10^{-4}\,\mathrm{K^{-1}}$). The results are shown in Figure 14.

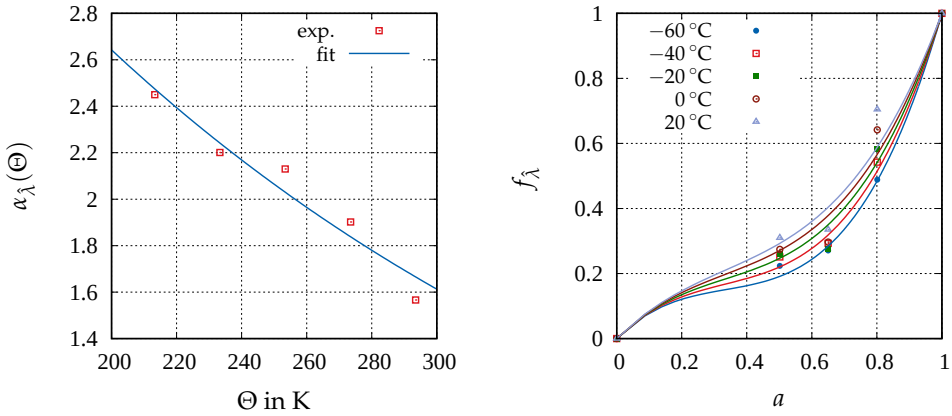

(**a**) (**b**)

Figure 14. Determination of the ponderation factor $f_{\hat{\lambda}}(\Theta, a)$. (**a**) Results of the identification of $\alpha_{\hat{\lambda}}(\Theta)$. (**b**) Experimentally determined ponderation factor $f_{\hat{\lambda}\text{exp}}(\Theta_i, a_j)$ (points) and model (lines) over the aging variable for constant values of the temperature.

The results of the entire identification of the thermal diffusivity are shown in Figure 15. One can see the small deviation between the simulation and the experiment for the 3 and 6 months old samples. However, the modeled function can reproduce the complex experimental behavior well.

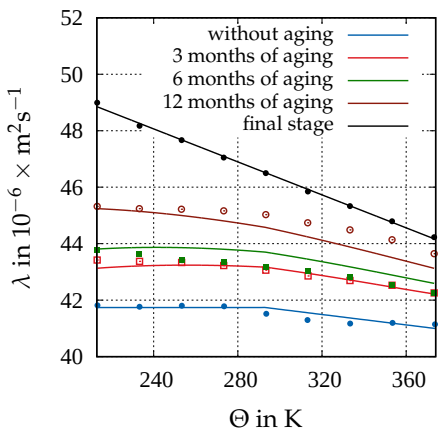

Figure 15. Results of the identification of the thermal diffusivity. Experimental values represented with points and model with lines.

4.3.4. Thermal Conductivity

With the identified values of the thermal diffusivity, the specific heat capacity, and the measured density, the parameter of the thermal conductivity can be determined with Equation (70). The thermal conductivity is shown in Figure 16, dependent on the temperature for different aging times.

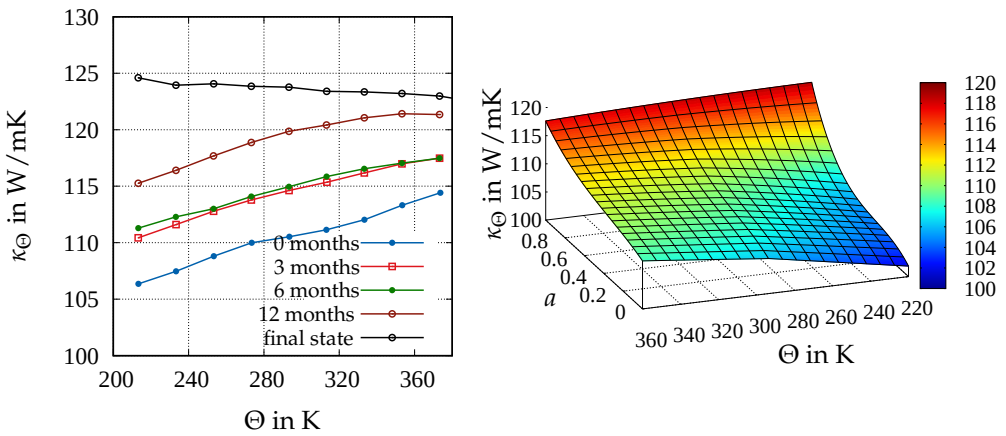

(**a**) (**b**)

Figure 16. Determined thermal conductivity with the identified parameters. (**a**) Thermal conductivity for different aging times over the temperature. (**b**) 3D-representation of the function $\kappa_\Theta(\Theta, a)$.

5. Stress Computation and Numerical Example

The constitutive model described in Table 1 along with the non-linear kinematics, the balance of linear momentum, the heat equation in connection with the initial and boundary conditions form a coupled system of partial and ordinary differential equations. A common approach is to apply the method of vertical lines, see [71,72]. In a first step, the spatial discretization is carried out yielding a system of differential-algebraic equations. The algebraic part stems from the weak form of the balance of linear momentum, and the ordinary differential parts is result of the weak form of the heat equation and the evolution equations of the constitutive model, see [73,74] for the concept in thermo-mechanical coupled situations, and for treating the non-linear equation [75]. In the subsequent considerations only low order finite elements and a time discretization using the Backward Euler method are applied. This leads in each point in time to a system of non-linear equations

$$\boldsymbol{G}_u(\boldsymbol{u}, \Theta, \boldsymbol{q}) := \boldsymbol{g}_u(t_{n+1}, \boldsymbol{u}_{n+1}, \Theta_{n+1}, \boldsymbol{q}_{n+1}) = \boldsymbol{0}, \tag{76}$$

$$\mathsf{G}_\Theta(\boldsymbol{u}, \Theta, \boldsymbol{q}) := \boldsymbol{C}_{\boldsymbol{p}_{n+1}} \frac{\Theta_{n+1} - \Theta_n}{\Delta t} - \boldsymbol{r}_\Theta(t_{n+1}, \boldsymbol{u}_{n+1}, \Theta_{n+1}, \boldsymbol{q}_{n+1}) = \boldsymbol{0}, \tag{77}$$

$$\boldsymbol{L}_q(\boldsymbol{u}, \Theta, \boldsymbol{q}) := \frac{\boldsymbol{q}_{n+1} - \boldsymbol{q}_n}{\Delta t} - \boldsymbol{r}_q(t_{n+1}, \boldsymbol{u}_{n+1}, \Theta_{n+1}, \boldsymbol{q}_{n+1}) = \boldsymbol{0}. \tag{78}$$

The solution of the non-linear system has to be done at each point in time t_{n+1} to obtain the unknown nodal displacements $\boldsymbol{u}_{n+1}$, the unknown nodal temperatures Θ_{n+1}, and internal variables $\boldsymbol{q}_{n+1}$, which are (formally) assembled from all Gauss-points of all elements into a large vector $\boldsymbol{q}_{n+1}$. Furthermore, we have to consider the initial conditions $\boldsymbol{u}(t = 0) = \boldsymbol{u}_0$, $\Theta(t = 0) = \Theta_0$, and $\boldsymbol{q}(t = 0) = \boldsymbol{0}$. Here, $\boldsymbol{G}_u$ represents the discretized form of the balance of linear momentum, $\boldsymbol{G}_\Theta$ the integration step of discretized weak form of the heat equation, and $\boldsymbol{L}_q$ the integration step of the discretized evolution equations of the internal variables, see Table 1. The computation of the Cauchy stress $\mathbf{T} \in \mathbb{R}^6$ (here, the Voigt notation is chosen instead of the tensor notation), the internal variables $\mathbf{q} \in \mathbb{R}^{6+6+3}$, and the consistent tangent $\mathbf{C}_t$ required for the global Multilevel-Newton algorithm—see, for details, Refs. [74,76] and the literature cited therein—are computed within the stress algorithm. Afterwards, the stress algorithm of the model is provided and the applicability of the model is demonstrated with two different validation examples.

5.1. Stress Algorithm

In the proposed model, the vector of internal variables $\mathbf{q}^\mathrm{T} = \{\mathbf{C}_\mathrm{p}^\mathrm{T}, \mathbf{C}_\mathrm{v}^\mathrm{T}, k, a\}$ has two vectorial components, $\mathbf{C}_\mathrm{p} \in \mathbb{R}^6$ and $\mathbf{C}_\mathrm{v} \in \mathbb{R}^6$, which are expressed in Voigt notation, and

two scalar components, k and a, as well as the arc-length s_{M}. By applying a Backward Euler step to the evolution equations of the internal variables at each Gauss point, see Table 1, one obtains

$$\mathbf{0} = \mathbf{C}_{\mathrm{p}n+1} - \mathbf{C}_{\mathrm{p}n} - \Delta t_n \left(4(\varphi_a \varphi_\Theta)^{-2} J^{-2/3} b \frac{\Delta s_{\mathrm{M}n}}{\Delta t_n} \mathbf{C}_{\mathrm{p}n+1} \mathbf{D}(\mathbf{C}_{\mathrm{p}n+1}^{-1} \mathbf{C}) \right), \tag{79}$$

$$\mathbf{0} = \mathbf{C}_{\mathrm{v}n+1} - \mathbf{C}_{\mathrm{v}n} - \Delta t_n \left(\frac{4\mu_{\mathrm{ov}}}{\eta} (\varphi_a \varphi_\Theta)^{-2} J^{-2/3} \mathbf{C}_{\mathrm{v}n+1} \mathbf{D}(\mathbf{C}_{\mathrm{v}n+1}^{-1} \mathbf{C}) \right), \tag{80}$$

$$0 = k_{n+1} - k_n - \Delta t_n \left(\alpha_k (1 - k_{n+1}) \frac{\Delta s_{\mathrm{M}n}}{\Delta t_n} \right), \tag{81}$$

$$0 = a_{n+1} - a_n - \Delta t_n \beta_{a1}(\Theta_{n+1}) \frac{1 - a_{n+1}}{\beta_{a2} + a_{n+1}}, \tag{82}$$

with the increment of the mechanical arc-length

$$\Delta s_{\mathrm{M}n} = s_{n+1} - s_n = \frac{J^{-2/3}}{2} \sqrt{\left(\mathbf{C}_{\mathrm{p}n+1}^{-1} \mathbf{C} \mathbf{D}(\mathbf{C}^{-1} \Delta \mathbf{C}) \mathbf{C}_{\mathrm{p}n+1}^{-1} \right)^{\mathrm{T}} \mathbf{M}^{-1} \left(\mathbf{C} \mathbf{D}(\mathbf{C}^{-1} \Delta \mathbf{C}) \right)}. \tag{83}$$

$\mathbf{C} := \mathbf{C}_{n+1} \in \mathbb{R}^6$ defines the vector containing the components of the right Cauchy-Green tensor in the current iteration of the Multilevel-Newton algorithm, and $\mathbf{D} \in \mathbb{R}^6 6$ represents the deviator operator (in matrix form). In other words, at each Gauss-point the non-linear system Equations (79)–(82) in the form of a system of non-linear equations

$$\mathbf{L}_{\mathrm{p}}(\mathbf{C}, \Theta, \mathbf{C}_{\mathrm{p}}, a) = \mathbf{0}, \tag{84}$$

$$\mathbf{L}_{\mathrm{v}}(\mathbf{C}, \Theta, \mathbf{C}_{\mathrm{p}}, \mathbf{C}_{\mathrm{v}}, k, a) = \mathbf{0}, \tag{85}$$

$$\mathrm{L}_k(\mathbf{C}, \Theta, \mathbf{C}_{\mathrm{p}}, k) = 0, \tag{86}$$

$$\mathrm{L}_a(\Theta, a) = 0 \tag{87}$$

has to be computed. After this step, the second Piola-Kirchhoff stress can be computed for the internal variables $\mathbf{q}^{\mathrm{T}} = \{\mathbf{C}_{\mathrm{p}n+1}^{\mathrm{T}}, \mathbf{C}_{\mathrm{v}n+1}^{\mathrm{T}}, k_{n+1}, a_{n+1}\}$,

$$\begin{aligned} \tilde{\mathbf{T}}_{n+1} &= \tilde{\mathbf{h}}(\mathbf{C}_{n+1}, \Theta_{n+1}, \mathbf{C}_{\mathrm{p}n+1}, \mathbf{C}_{\mathrm{v}n+1}, k_{n+1}, a_{n+1}) \\ &= \tilde{\mathbf{T}}^{\mathrm{e}}_{\mathrm{eq}n+1}(\mathbf{C}_{n+1}, \Theta_{n+1}, a_{n+1}) + \tilde{\mathbf{T}}^{\mathrm{h}}_{\mathrm{eq}n+1}(\mathbf{C}_{n+1}, \Theta_{n+1}, \mathbf{C}_{\mathrm{p}n+1}) \\ &+ \tilde{\mathbf{T}}_{\mathrm{ov}n+1}(\mathbf{C}_{n+1}, \Theta_{n+1}, \mathbf{C}_{\mathrm{v}n+1}). \end{aligned} \tag{88}$$

Here, the elastic equilibrium stress state is given by

$$\tilde{\mathbf{T}}^{\mathrm{e}}_{\mathrm{eq}n+1} = \frac{K}{10} \left(J_{\mathrm{M}}^5 - J_{\mathrm{M}}^{-5} \right) \mathbf{C}^{-1} + 2c_{10} J^{-2/3} \mathbf{C}^{-1} \mathbf{D} \mathbf{C}, \tag{89}$$

with $J_{\mathrm{M}} = ((1 - \alpha_a a)(1 + \alpha_\Theta(\Theta - \Theta_0)))^{-3} J$, and the current temperature $\Theta = \Theta_{n+1}$. The plastic equilibrium stress state is given by

$$\tilde{\mathbf{T}}^{\mathrm{h}}_{\mathrm{eq}n+1} = 2\mu_{\mathrm{eq}}(\Theta_{n+1}) J^{-2/3} \mathbf{C}^{-1} \mathbf{D}(\mathbf{C} \mathbf{C}_{\mathrm{p}n+1}^{-1}), \tag{90}$$

and the overstress reads

$$\tilde{\mathbf{T}}_{\mathrm{ov}n+1} = 2\mu_{\mathrm{ov}}(k_{n+1}) J^{-2/3} \mathbf{C}^{-1} \mathbf{D}(\mathbf{C} \mathbf{C}_{\mathrm{v}n+1}^{-1}). \tag{91}$$

The Multilevel-Newton algorithm, see [76,77], is applied to solve the non-linear system of equations Equations (76)–(78) for which a consistent linearization is required. To this end, the consistent tangent has to be determined

$$\mathbf{C}_t = \begin{bmatrix} \frac{\mathrm{d}\tilde{\mathbf{h}}}{\mathrm{d}\mathbf{C}} & \frac{\mathrm{d}\tilde{\mathbf{h}}}{\mathrm{d}\Theta} \end{bmatrix}, \tag{92}$$

with

$$\frac{\mathrm{d}\tilde{\mathbf{h}}}{\mathrm{d}\mathbf{C}} = \frac{\partial\tilde{\mathbf{h}}}{\partial\mathbf{C}} + \frac{\partial\tilde{\mathbf{h}}}{\partial\mathbf{q}}\frac{\mathrm{d}\mathbf{q}}{\mathrm{d}\mathbf{C}}, \tag{93}$$

$$\frac{\mathrm{d}\tilde{\mathbf{h}}}{\mathrm{d}\Theta} = \frac{\partial\tilde{\mathbf{h}}}{\partial\Theta} + \frac{\partial\tilde{\mathbf{h}}}{\partial\mathbf{q}}\frac{\mathrm{d}\mathbf{q}}{\mathrm{d}\Theta}. \tag{94}$$

In the present case, it was computed with the help of the software Acegen, see [78,79], which allows to compute the tangent using Mathematica, combining symbolic and algebraic operations, automatic code generation, automatic differentiation, and simultaneous optimization of expressions.

5.2. Computational Examples

The behavior of the model is shown with the help of two computational examples in which inhomogeneous strain and stress states dominate the structural response. In both cases, experimental results in real components are compared to simulations obtained with the developed material model. The first example includes the effect of the temperature, and the second example treats the effect of aging.

5.2.1. Influence of Temperature

In this first example, the component part shown in Figure 17 is used. The specimens were provided by the manufacturer and were already several years old when the experiments were performed (i.e., a totally different batch is chosen). Thus, the component part has already reached the completely aged state in the simulation, $a(t) = 1$. As shown in Figure 17a, the upper area of the component is fixed with a screw to the testing machine's fixture and the lower area is pulled with the help of an inserted oval bolt. There are four different isothermal experiments at three different temperatures equal to 20 °C, 50 °C, and 70 °C in total. Here, the load experienced by the component results from the measured relative displacement between upper region and bolt, which is shown in Figure 18 with the corresponding temperatures for each experiment. Since the experiments were performed at different time scales, the time axis in Figure 18 is normed to the end time of each experiment. For each experiment, the reaction force is measured with a force sensor as well as the surface deformation using a digital image correlation system.

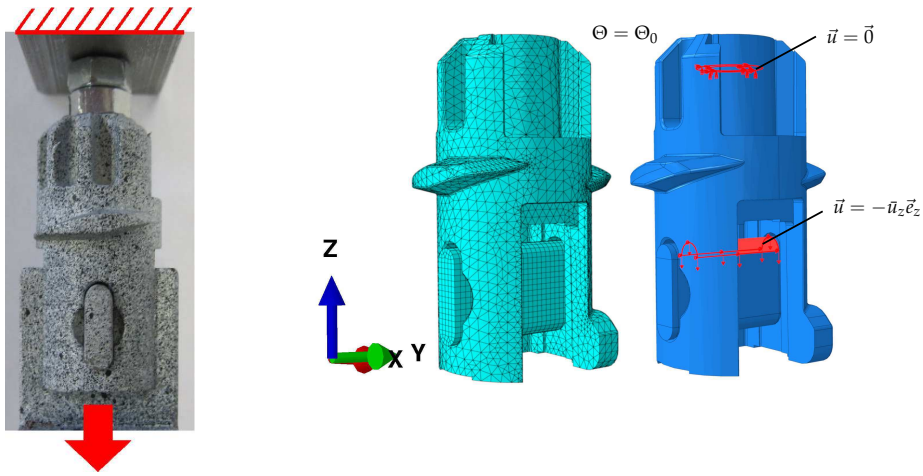

(**a**) Experiment (**b**) Geometry and boundary conditions

Figure 17. Component part used for the validation of the model for different temperatures.

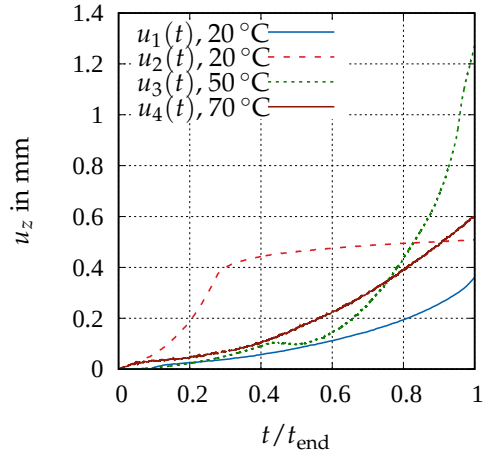

Figure 18. Prescribed displacement for the simulations over the normed time. Final values: $t_{\text{end1}} = 13.4\,\text{s}$, $t_{\text{end2}} = 9\,\text{h}$, $t_{\text{end3}} = 143\,\text{s}$, $t_{\text{end4}} = 140\,\text{h}$.

In the following, the experiment is modeled with the commercial finite element program Abaqus as shown in Figure 17b. The component part is meshed with quadratic tetrahedral elements (10 nodes per element) and the bolt with linear, eight-noded hexahedral elements. The problem has totally 54,078 elements and 85,569 nodes. The upper area of the geometry, which would be in contact with the screw, is fixed ($\vec{u} = \vec{0}$) and on the bolt a displacement $\vec{u} = -u_z\vec{e}_z$ is applied, see Figure 17b right. The values of Figure 18 are considered for the displacement u_z and temperature $\Theta = \text{const.}$ for each simulation. The contact formulation "node-to-surface" is chosen for the contact between the bolt and the component part. For the tangential behavior, a friction coefficient of 0.5 is assumed, see [80]. For the normal and tangential behavior, the standard options of Abaqus for the penalty method are chosen. The bolt is modeled as linear elastic steel (Young's modulus 210 MPa and Poisson's ratio 0.3) and the component part with the proposed material model. The initial value of the aging variable in each simulation is equal to $a(t = 0) = 1$, i.e., the completely aged state. The initial values for the remaining internal variables correspond to the state without previous deformation $\bar{\mathbf{C}}_\text{p}(0) = \mathbf{I}$, $\bar{\mathbf{C}}_\text{v}(0) = \mathbf{I}$, and $k(0) = 0$. The simulations are carried out with automatic load step control, which are different for each simulation since the time scale varies as well. The values of the initial minimum and maximum time step for the four simulations are shown in Table 9.

Table 9. Time step choices.

	Simulation 1	**Simulation 2**	**Simulation 3**	**Simulation 4**
Δt_0	0.1	100	1	1
Δt_{min}	10^{-3}	10^{-2}	10^{-3}	10^{-3}
Δt_{max}	0.1	210	1	1

The results of the simulations and experiments are shown in Figure 19. There, the reaction force over the prescribed displacement of the bolt is displayed. In Figure 20 the deformation on the surface of the component part for the third loading case ($\Theta_3 = 50\,°\text{C}$) is shown as an example, other results are similar here. Figure 20a displays the major strain at the final point in time of the experiment, and Figure 20b the simulation concerned. Values equal or higher than 5 % deformation are shown in red. Figure 20c displays the major strain for a chosen point on the surface over time for experiment and simulation. Since the experiments at room temperature ($\Theta = 20\,°\text{C}$) were performed at two different strain rates, see Figure 19a,b, we can observe that the model is able to reproduce the rate dependence, see Figure 18 with $t_{\text{end1}} = 13.4\,\text{s}$, $t_{\text{end2}} = 9\,\text{h}$, although it presents difficulties reproducing completely the relaxation behavior in Figure 19b. In more recent invesigations, see [81,82],

considering the Gaussian error propagation concept to estimate the uncertainty due to uncertain input data, it was shown that both the uncertain material parameters as well as the uncertain boundary conditions and geometrical data of the specimens have an essential influence on the simulation of real parts. Particularly, the totally unknown spatial and size distribution of micro-voids, see in this context [30], might have an essential effect for higher loads. This can be observed in all diagrams of Figure 19. However, the exact causes (contact problem with relaxation properties, micro-voids distribution with micro-crack initiation, ...) cannot exactly substantiated. The temperature dependence can be considered comparing Figure 19a,c,d. Here, one can see that in these three cases the starting point of the experiment is difficult to reproduce. The reason lies in the inaccuracy of the boundary conditions at these start times, which do not correspond completely to the simulation of the experiment (e.g., contact, position of the bolt). Moreover, the experiments at 50 °C and 70 °C were performed in a thermal chamber which introduces an inaccuracy in the measurement of the digital image correlation system due to the fact that the measurements have to be performed through glass windows of the chamber. Particularly, for the environmental temperature of 70 °C, the simulation shows a slightly more stiff response above a certain loading state. This can be seen at the identified state in Figure 19d. In the future, one might consider changing the temperature-dependence in the model.

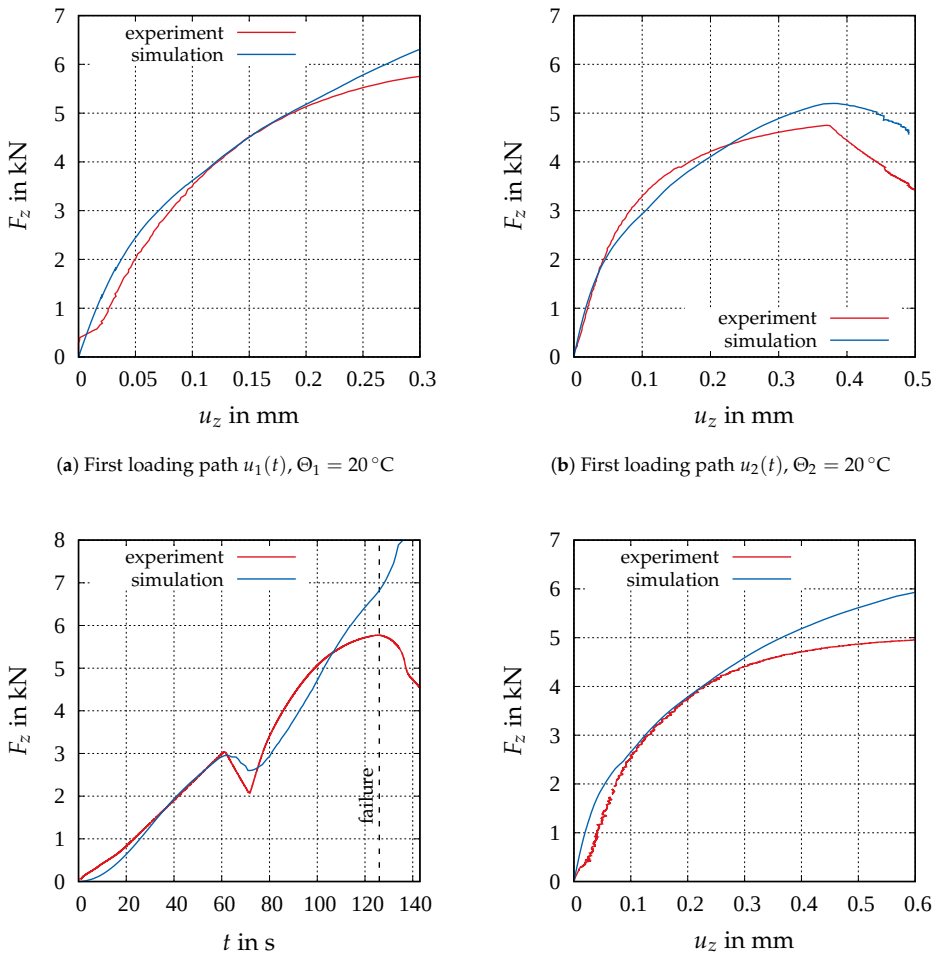

(**a**) First loading path $u_1(t)$, $\Theta_1 = 20\,°\mathrm{C}$

(**b**) First loading path $u_2(t)$, $\Theta_2 = 20\,°\mathrm{C}$

(**c**) First loading path $u_3(t)$, $\Theta_3 = 50\,°\mathrm{C}$

(**d**) Fourth loading path $u_4(t)$, $\Theta_4 = 70\,°\mathrm{C}$

Figure 19. Reaction force over time. Comparison between experiment (red) and simulation (blue).

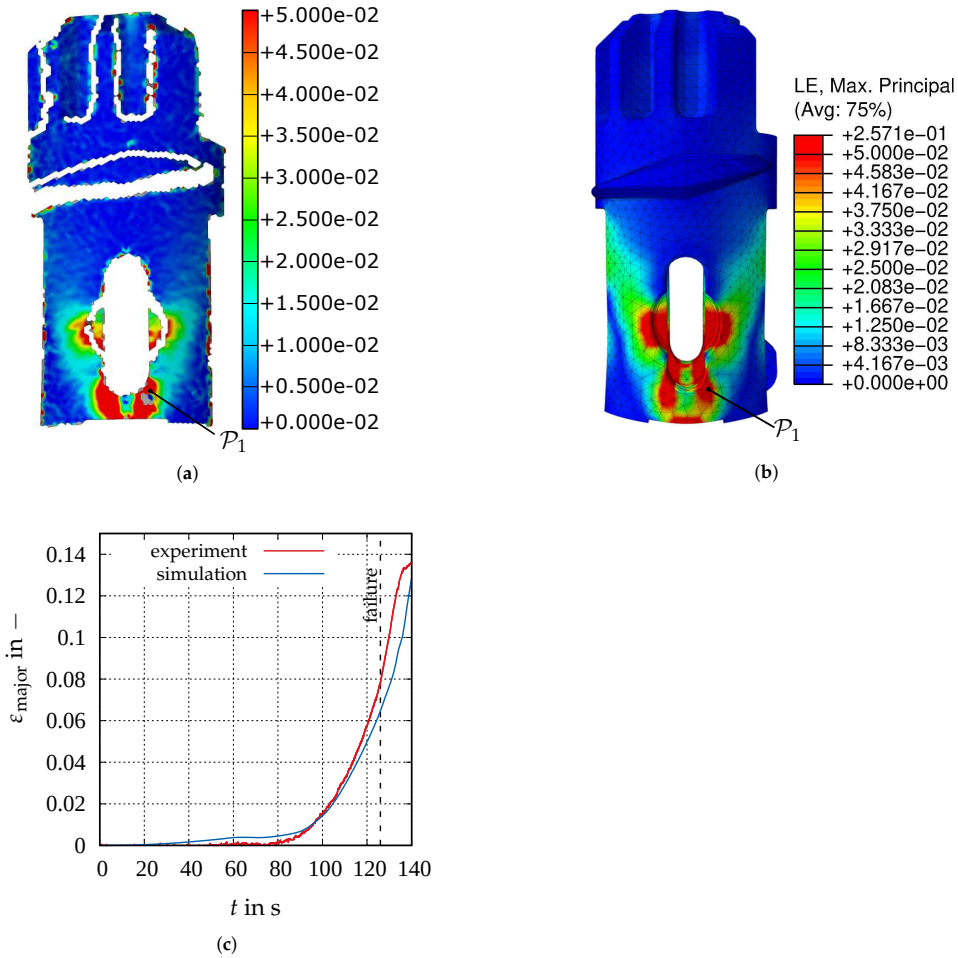

Figure 20. Results of experiment and simulation for the third loading case $\bar{u}_z(t) = u_3(t)$, $\Theta = 50\,°\text{C}$. Higher values than 5% are marked in red, also in (**a**,**b**). (**a**) Major strain in the experiment at $t = 127\,\text{s}$. (**b**) Major strain in the simulation for the last time step $t = 127\,\text{s}$. (**c**) Major strain over the time at the position $\mathcal{P}_1$, see (**b**).

5.2.2. Influence of Aging

The second example shows the ability of the model to reproduce the aging dependence. To this end, specimens with a known age are necessary. In this case, cylindrical tubes with a hole were used in torsion experiments for the validation as shown in Figure 21a.

One end of the specimens was fixed, and on the other end a rotation was applied as shown in Figure 21c. The experiments were performed at the constant temperature of 27 °C and with specimens with three different aging times: without aging, with twelve months natural aging and a completely (artificially) aged specimen. The reaction torque was measured over time with the help of the testing machine's torque sensor and the deformation of the specimens was measured on the surface with the digital image correlation system.

The specimen was modeled in Abaqus standard as shown in Figure 21b. It is meshed with 18,608 quadratic, 20-noded hexahedral elements and has 97,759 nodes. For the boundary conditions, the upper clamping area of the specimen is fixed ($\vec{u} = \vec{0}$) and on the lower clamping, the rotation $\vec{\varphi} = \bar{\varphi}_y \vec{e}_y$ as shown in Figure 21c is applied. The temperature is constant during the simulation and is equal to 27 °C. The proposed constitutive model is used assuming both a "young" specimens (initial aging variable $a(t = 0) = 0$ for the specimen without aging) as well as $a(t = 0) = 0.802$ for the specimen with twelve months natural aging (this value was determined solving the evolution equation of the aging variable at the constant temperature of 19 °C for 12 months), and, thirdly, $a(t = 0) = 1$ for the completely aged specimen. The initial values for the remaining internal variables

are $\bar{\mathbf{C}}_{\mathrm{p}}(0) = \mathbf{I}$, $\bar{\mathbf{C}}_{\mathrm{v}}(0) = \mathbf{I}$, and $k(0) = 0$. The results of the simulation and experiment are shown in Figures 22 and 23. Here, the reaction torque over time is displayed. One can observe a very good agreement between experiment and simulation. The completely aged specimen shows the higher difference between experiment and simulation. It is possible that the discrepancy between the observed and predicted results is due to the fact that no experiments with a completely aged material were used for the identification process. This would be a purely predictive outcome of the model. Figures 24 and 25 display the major strain at the final moment of the experiment and the simulation for the specimen with twelve months natural aging as an example result. The other cases are the same. Values larger than 4 % are shown in red. Figure 24 shows a very good reproducibility of the experimental results by the simulation.

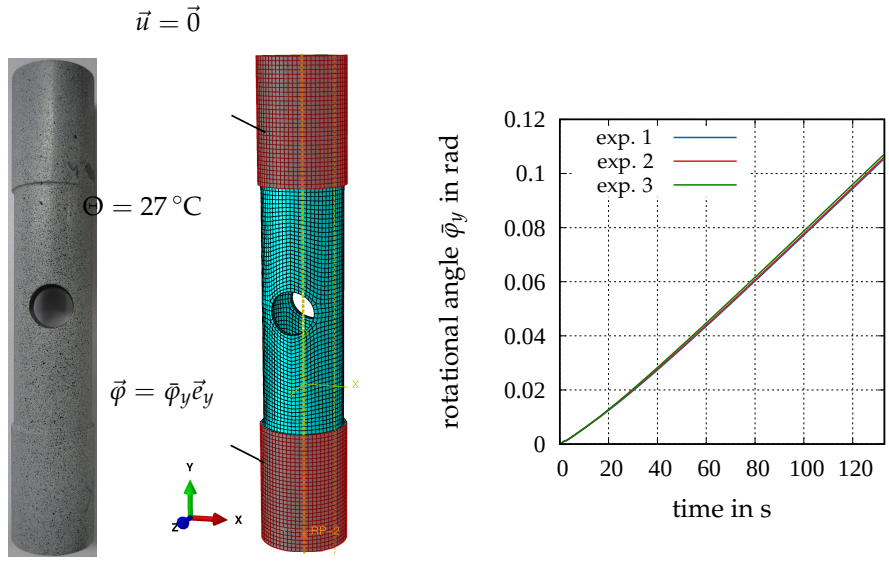

(**a**) Specimen (**b**) Mesh and boundary conditions (**c**) Measured rotational angle over time

Figure 21. Mesh and boundary conditions for the torsion experiments at different aging times.

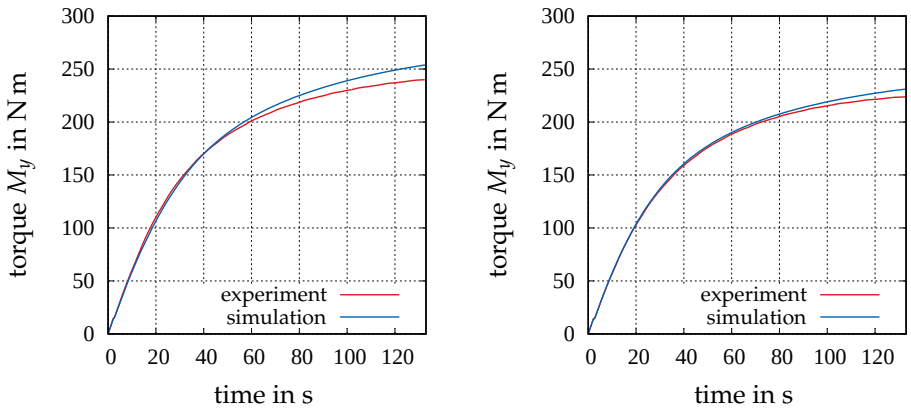

(**a**) Specimen without aging (**b**) Specimen with twelve months natural aging

Figure 22. Reaction torque over time.

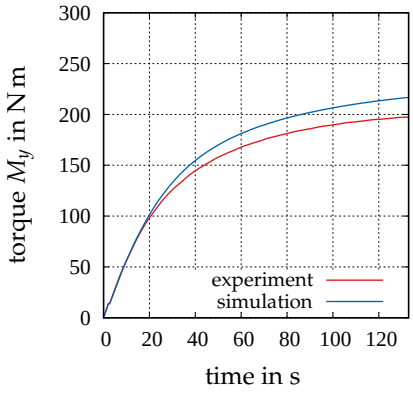

Figure 23. Reaction torque over the time for the completely aged specimen.

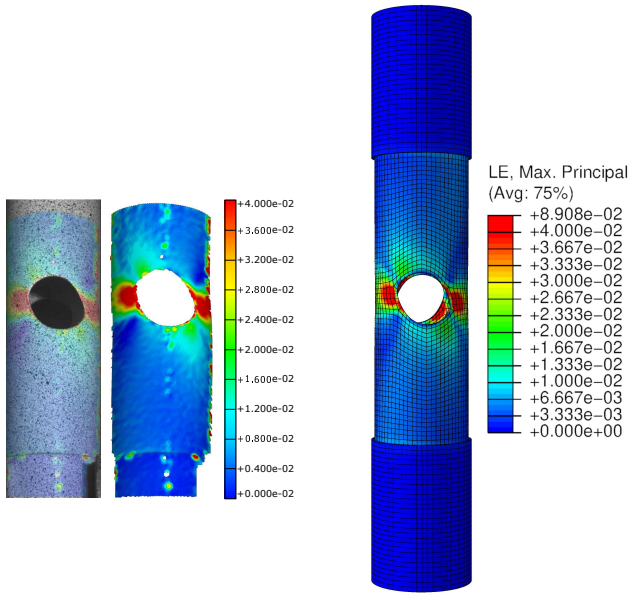

Figure 24. True major strain at the last time step $t = 133\,\mathrm{s}$ for experiment and simulation (12 months of natural aging). On the left the experiment and on the right the simulation.

The major strain over time is displayed in Figure 25 for different points at the surface of the specimen. Here, we can see the good agreement between experiment and simulation as well.

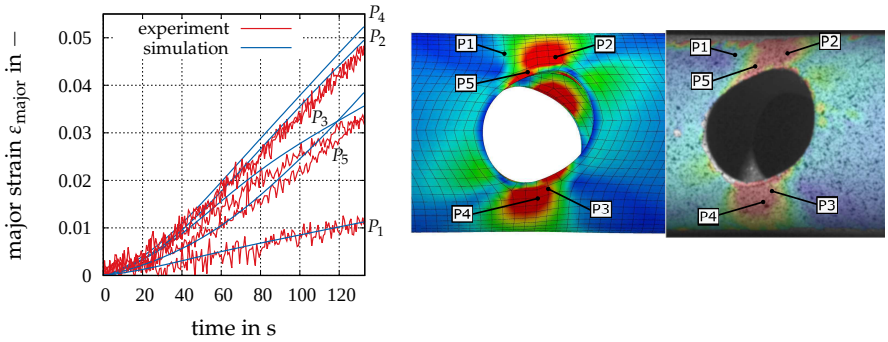

(**a**) (**b**)

Figure 25. Major strains for the 12 months old specimen (experiment and simulation). (**a**) Major strain over time for the points on the surface defined in (**b**). (**b**) Point position (simulation left and experiment right).

5.2.3. Validation of the Model

The evaluation of the agreement between experimental results and simulation is performed with certain numerical values. Thus, we are interested in the deviation of the simulation results with respect to the experimental measurement. First, the absolute error $\mathrm{err}_{F\mathrm{abs}}$ and relative error $\mathrm{err}_{F\mathrm{rel}}$ in the force of the evaluations of the complex geometry in Figure 19 are defined by

$$\mathrm{err}_{F\mathrm{abs}} = |F_{\mathrm{exp}} - F_{\mathrm{sim}}|, \tag{95}$$

$$\mathrm{err}_{F\mathrm{rel}} = 100 \times \frac{\mathrm{err}_{F\mathrm{abs}}}{|F_{\mathrm{exp}}|}. \tag{96}$$

Second, the torque quantities in the cylindrical tube with the hole of Figures 22 and 23 are defined as

$$\mathrm{err}_{M\mathrm{abs}} = |M_{\mathrm{exp}} - M_{\mathrm{sim}}|, \tag{97}$$

$$\mathrm{err}_{M\mathrm{rel}} = 100 \times \frac{\mathrm{err}_{M\mathrm{abs}}}{|M_{\mathrm{exp}}|}. \tag{98}$$

They are displayed in Figures 26 and 27. In Figures 26b and 27b we can see that the relative error is generally larger at the beginning than in the other course of the line. The two main reasons are (1) that the slope in the force-displacement diagram is larger for small displacements, and, because of that, small absolute errors are relatively large. (2) the measured force is approaching zero in certain time intervals at the beginning of the experiments, but not in the simulation, which causes high relative errors. Moreover, one can observe that the relative error is smaller for the torsion experiments at different aging times than for the complex geometry (since the specimens drawn on for the torsion experiments were produced in the same batch as the specimens used for the experimental material characterization). Since this is not the case for the component part, larger deviations are expected. The errors are also larger for the artificially aged specimen, see Figure 27. The model tends to overestimate the torque and force for a fully aged material since these values were not used in the identification process.

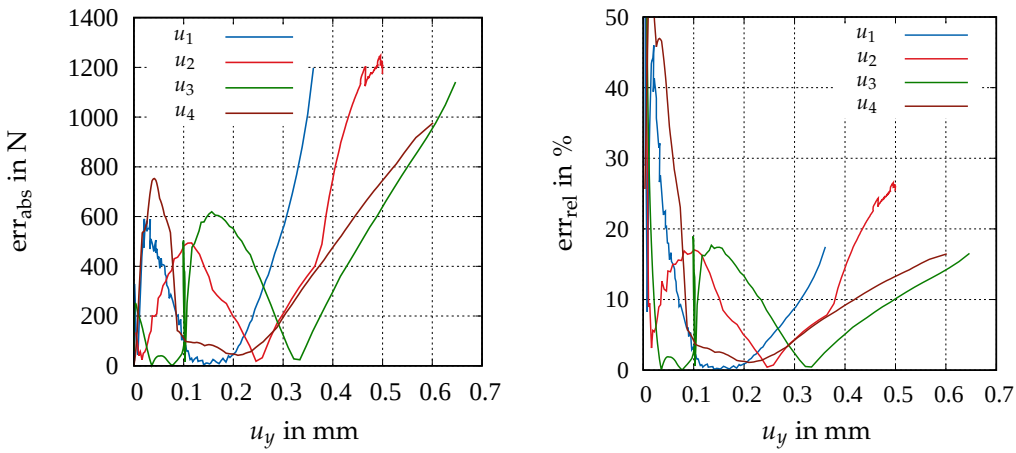

(**a**) Absolute error in the reaction force (**b**) Relative error of the reaction force

Figure 26. Absolute and relative error in the reaction force over time between experiment and simulation for the experiments at different temperatures and displacement paths.

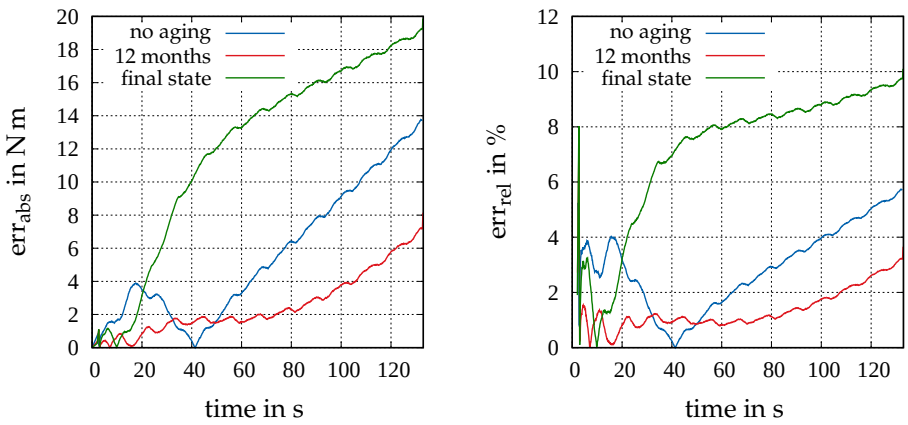

(**a**) Absolute error in the torque (**b**) Relative error in the torque

Figure 27. Absolute and relative error of the torque over time between experiment and simulation for the experiments at different aging times.

In the following, a validation metric is introduced to provide an indicator of the ability of the constitutive model to predict the real behavior of a component part made of Zamak. Since a value of the quantity of interest is measured over time for different processes instead of having one unique value for one experiment that is repeated several times, we decided to adapt the metric proposed in [83] to this case. There are n_{exp} different experiments with n_p^i data points for the i-experiment. The experimental value of a quantity of interest is represented as y_e and the result of the simulation as y_m (response of the model). The maximum relative error E is used now as an error measure, which is defined as the maximum relative error of all the experiments

$$E = \max|\epsilon_i|, \qquad \epsilon_i = \frac{y_{mj}^i - y_{ej}^i}{y_{e\max}^i}. \tag{99}$$

Here, an experiment is denoted by i and a point of the experiment by j. The maximum value of the experiment i is represented by $y_{e\max}^i$. The experiment with the maximum relative error is denoted with the index E. Similarly as proposed in [83], the confidence interval (CI) for this error is a normalized measure by the maximum experimental value evaluated at the point where the maximum relative error metric occurs

$$\left|\frac{\text{CI}}{y_{e\,\max}^E}\right| = \frac{t_{0.05,\nu}}{\sqrt{n_p^E}}\left|\frac{s_{\text{E}}}{y_{e\,\max}^E}\right|, \qquad \text{with} \qquad s_E = \left(\frac{1}{n_p^E - 1}\sum_{j=1}^{n_p^E}(y_{mj}^E - \bar{y}_e^E)^2\right). \tag{100}$$

Here, $t_{0.05,\nu}$ is the t-distribution for 90% confidence, with $\nu = n_p - 1$, and the mean value of the experimental points of an experiment i is written as $\bar{y}_e^i$. The value $y_{e\,\max}^E$ has the goal to normalize the confidence interval in the same way as the error E to make them comparable. The model is developed for non-cyclic quasi-static processes up to a maximum strain of approximately 10 % with Zamak 5. Processes at different strain rates, temperatures, and aging times are included in the validation with influence of torsion and tension/compression. Thus, by applying the validation metric from Equations (99) and (100) to the measurements, the values of Table 10 are obtained.

Table 10. Relative error and confidence interval for every experiment.

	Exp. 1	**Exp.2**	**Exp. 3**	**Exp. 4**	**Exp. 5**	**Exp. 6**	**Exp. 7**
E in −	0.2067	0.2626	0.1816	0.3133	0.0574	0.0364	0.1007
CI in −	0.0473	0.0224	0.0053	0.0053	0.0119	0.0113	0.0122

The maximum deviation equal to $E = 31.33\%$ with a confidence interval of 0.53% takes place in the fourth experiment and simulation (component part at 70 °C). Therefore, the simulation is able to predict the experiments with a maximum relative error of 31.33 % for deformations of at least 5 %. This relative error is, in general, smaller for lower deformations and it is also connected to other factors such as the thickness of the specimen and other microstructural imperfections such as micro-voids, see [30].

6. Conclusions

The provided material model finally provides a comprehensive model for the simulation of components made of the zinc die casting alloymaterial Zamak 5, which is used for large strain applications, temperature ranges in automotive applications, and for the consideration of different aging conditions. Additionally, an implementation in the commercial finite element program Abaqus is presented to interested investigators. The material model implies rate-dependent mechanical processes, temperature, and aging dependence. In addition to the new development of the model, the presentation details how the material parameters occurring in it can be determined as thoroughly as possible from a variety of experiments. The evaluation of the correlation matrix is used for this purpose.

The validation of the model (material model and model for computation) is carried out using a complex component made of Zamak. The force-displacement curves for the fully aged component of the finite element simulations agree very well with the experimental results up to the point of failure of the component. To characterize the validation more precisely, a validation metric that was developed in the context of fluid mechanical simulations is transferred to the solid mechanics problem at hand. Using displacement data derived from full-field data of digital image correlation measurements, the quantified deviation in a tensile-torsion test of 70 °C leads to approx. 30 % with a low confidence interval. This shows that the quantification of simulation results from finite element simulations is very possible. In addition, a validation measure for practical use is presented to enable users to quantify the simulation results in comparison to experimental data.

Author Contributions: Software development, evaluation, experimenation, writing, writing—original draft preparation, M.A.M.P.; funding aquisition, resources, supervision, project administration, review and editing, S.H. All authors have read and agreed to the published version of the manuscript.

Funding: This research was funded by the Germany Research Foundation (DFG) grant number DFG HA2024-18/1.

Institutional Review Board Statement: Not applicable.

Informed Consent Statement: Not applicable.

Data Availability Statement: The original contributions presented in the study are included in the article, further inquiries can be directed to the corresponding author.

Acknowledgments: We would like to thank the team of Alexander Lion from the Institute of Mechanics of the Bundeswehr University Munich the for the shrinkage measurements and Bernd Weidenfeller for the cooperation in the measurements of the thermal diffusivity and specific heat capacity.

Conflicts of Interest: The authors declare no conflicts of interest.

Appendix A. Transformations of Strains, Stresses and Their Time Derivatives

The transformations between the strains, strain rates and stresses in the different configurations is shown in Figures A1–A3.

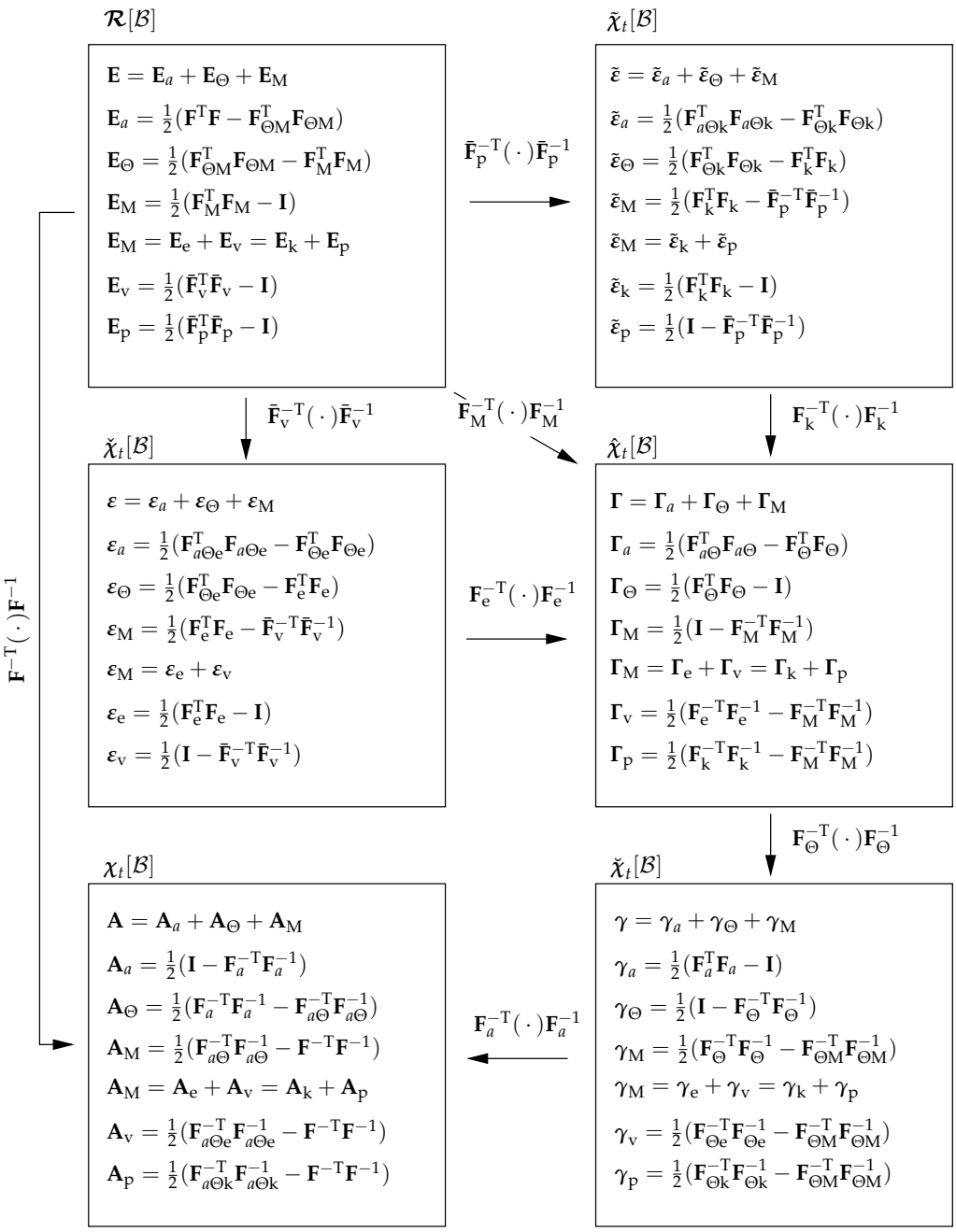

Figure A1. Transformation of the strains in the different configurations.

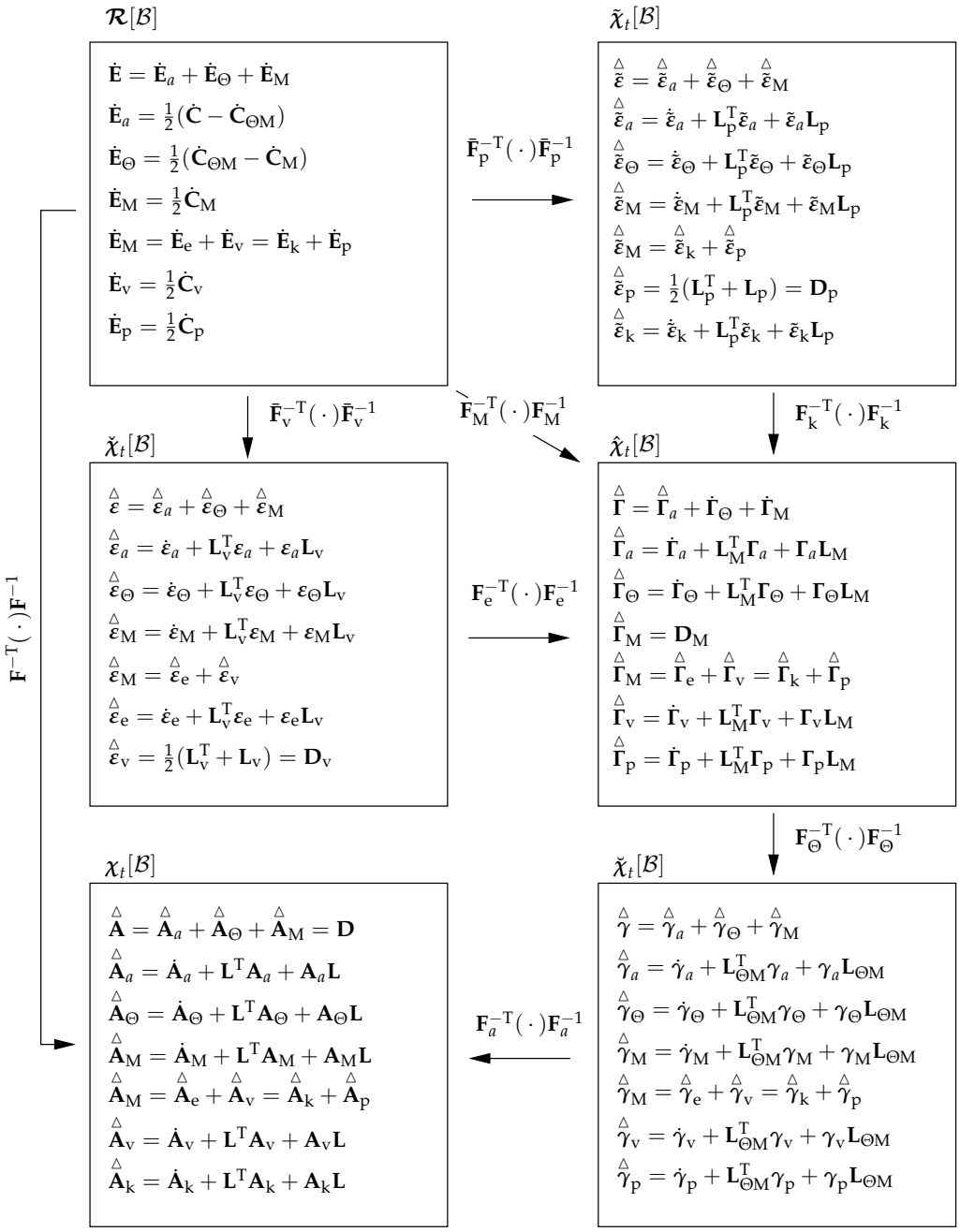

Figure A2. Transformations of the strain rates in the different configurations.

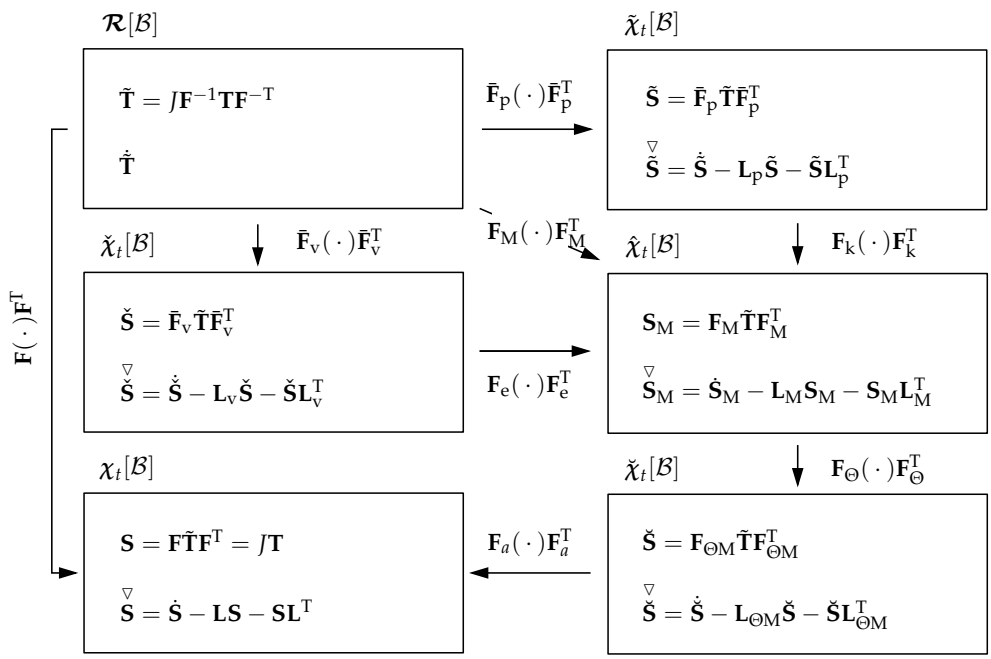

Figure A3. Transformation of the stress and stress rates in the different configurations.

Appendix B. Stress Power and Resulting Stress Measures

In order to ensure the thermodynamical consistence of the model, the Clausius-Duhem inequality is evaluated, see [48]. To this end, an expression for the stress power in dependence of the model variables is determined. The stress power formulated with quantities relative to the reference configuration reads

$$\tilde{\mathbf{T}} \cdot \dot{\mathbf{E}} = \tilde{\mathbf{T}} \cdot \dot{\mathbf{E}}_\mathrm{M} + \tilde{\mathbf{T}} \cdot \dot{\mathbf{E}}_\Theta + \tilde{\mathbf{T}} \cdot \dot{\mathbf{E}}_a, \tag{A1}$$

where the decomposition (11) is inserted. Considering the invariance of the stress power with the configurational change, we can express the term $\tilde{\mathbf{T}} \cdot \dot{\mathbf{E}}_\mathrm{M}$ by

$$\tilde{\mathbf{T}} \cdot \dot{\mathbf{E}}_\mathrm{M} = \tilde{\mathbf{T}} \cdot \mathbf{F}_\mathrm{M}^\mathrm{T}\overset{\triangle}{\mathbf{\Gamma}}_\mathrm{M}\mathbf{F}_\mathrm{M} = \mathbf{F}_\mathrm{M}\tilde{\mathbf{T}}\mathbf{F}_\mathrm{M}^\mathrm{T} \cdot \overset{\triangle}{\mathbf{\Gamma}}_\mathrm{M} = \mathbf{S}_\mathrm{M} \cdot \overset{\triangle}{\mathbf{\Gamma}}_\mathrm{M}, \tag{A2}$$

with $\mathbf{S}_\mathrm{M} = \mathbf{F}_\mathrm{M}\tilde{\mathbf{T}}\mathbf{F}_\mathrm{M}^\mathrm{T}$ being the stress tensor relative to the mechanical configuration $\hat{\chi}_t$, see Figure A3. Analogously, the term of the thermal part $\tilde{\mathbf{T}} \cdot \dot{\mathbf{E}}_\Theta$ is equal to

$$\tilde{\mathbf{T}} \cdot \dot{\mathbf{E}}_\Theta = \tilde{\mathbf{T}} \cdot \mathbf{F}_\mathrm{M}^\mathrm{T}\overset{\triangle}{\mathbf{\Gamma}}_\Theta\mathbf{F}_\mathrm{M} = \mathbf{F}_\mathrm{M}\tilde{\mathbf{T}}\mathbf{F}_\mathrm{M}^\mathrm{T} \cdot \overset{\triangle}{\mathbf{\Gamma}}_\Theta = \mathbf{S}_\mathrm{M} \cdot \overset{\triangle}{\mathbf{\Gamma}}_\Theta. \tag{A3}$$

Inserting the covariant Oldroyd rate

$$\overset{\triangle}{\mathbf{\Gamma}}_\Theta = \dot{\mathbf{\Gamma}}_\Theta + \mathbf{L}_\mathrm{M}^\mathrm{T}\mathbf{\Gamma}_\Theta + \mathbf{\Gamma}_\Theta\mathbf{L}_\mathrm{M} = \varphi_\Theta\frac{\partial\varphi_\Theta}{\partial\Theta}\dot{\Theta}\mathbf{I} + (\varphi_\Theta^2 - 1)\overset{\triangle}{\mathbf{\Gamma}}_\mathrm{M} \tag{A4}$$

of the thermal strain $\mathbf{\Gamma}_\Theta = 1/2(\mathbf{F}_\Theta^T\mathbf{F}_\Theta - \mathbf{I}) = (\varphi_\Theta^2 - 1)/2\mathbf{I}$ into the thermal stress power, the resulting relation can be expressed by scalar quantities of the temperature and tensorial quantities relative to the mechanical configuration

$$\tilde{\mathbf{T}} \cdot \dot{\mathbf{E}}_\Theta = \varphi_\Theta\frac{\partial\varphi_\Theta}{\partial\Theta}\dot{\Theta}(\mathrm{tr}\,\mathbf{S}_\mathrm{M}) + (\varphi_\Theta^2 - 1)\mathbf{S}_\mathrm{M} \cdot \overset{\triangle}{\mathbf{\Gamma}}_\mathrm{M}. \tag{A5}$$

The last term to be evaluated is the aging contribution $\tilde{\mathbf{T}} \cdot \dot{\mathbf{E}}_a$

$$\tilde{\mathbf{T}} \cdot \dot{\mathbf{E}}_a = \tilde{\mathbf{T}} \cdot \mathbf{F}_{\Theta\mathrm{M}}^\mathrm{T}\overset{\triangle}{\gamma}_a\mathbf{F}_{\Theta\mathrm{M}} = \mathbf{F}_{\Theta\mathrm{M}}\tilde{\mathbf{T}}\mathbf{F}_{\Theta\mathrm{M}}^\mathrm{T} \cdot \overset{\triangle}{\gamma}_a = \check{\mathbf{S}} \cdot \overset{\triangle}{\gamma}_a, \tag{A6}$$

with $\check{\mathbf{S}} = \mathbf{F}_{\Theta\mathrm{M}}\tilde{\mathbf{T}}\mathbf{F}_{\Theta\mathrm{M}}^{\mathrm{T}}$ being the stress tensor relative to the thermal configuration. The covariant Oldroyd rate $\overset{\triangle}{\gamma}_a$ is equal to

$$\overset{\triangle}{\gamma}_a = \dot{\gamma}_a + \mathbf{L}_{\Theta\mathrm{M}}^{\mathrm{T}}\gamma_a + \gamma_a\mathbf{L}_{\Theta\mathrm{M}}. \tag{A7}$$

The spatial velocity "gradient" $\mathbf{L}_{\Theta\mathrm{M}}$ can be decomposed into the sum of the thermal $\mathbf{L}_\Theta = \dot{\mathbf{F}}_\Theta\mathbf{F}_\Theta^{-1}$ and mechanical $\mathbf{L}_\mathrm{M} = \dot{\mathbf{F}}_\mathrm{M}\mathbf{F}_\mathrm{M}^{-1}$ parts,

$$\mathbf{L}_{\Theta\mathrm{M}} = \mathbf{L}_\Theta + \mathbf{L}_\mathrm{M}, \qquad \mathbf{L}_\Theta = \frac{1}{\varphi_\Theta}\frac{\partial\varphi_\Theta}{\partial\Theta}\dot{\Theta}\mathbf{I} \tag{A8}$$

where we consider $\mathbf{F}_{\Theta\mathrm{M}} = \varphi_\Theta\mathbf{F}_\mathrm{M}$, and $\mathbf{F}_\Theta = \varphi_\Theta\mathbf{I}$. Making use of $\overset{\triangle}{\mathbf{\Gamma}}_\mathrm{M} = \frac{1}{2}(\mathbf{L}_\mathrm{M}^{\mathrm{T}} + \mathbf{L}_\mathrm{M})$ and Equation (A8), one obtains

$$\overset{\triangle}{\gamma}_a = \varphi_a\frac{\partial\varphi_a}{\partial a}\dot{a}\mathbf{I} + \frac{1}{\varphi_\Theta}\frac{\partial\varphi_\Theta}{\partial\Theta}\dot{\Theta}(\varphi_a^2 - 1)\mathbf{I} + (\varphi_a^2 - 1)\overset{\triangle}{\mathbf{\Gamma}}_\mathrm{M}. \tag{A9}$$

Inserting this expression into Equation (A6) leads to

$$\tilde{\mathbf{T}}\cdot\dot{\mathbf{E}}_a = \left(\varphi_a\frac{\partial\varphi_a}{\partial a}\dot{a} + \frac{1}{\varphi_\Theta}\frac{\partial\varphi_\Theta}{\partial\Theta}\dot{\Theta}(\varphi_a^2 - 1)\right)\varphi_\Theta^2\,\mathrm{tr}\,\mathbf{S}_\mathrm{M} + (\varphi_a^2 - 1)\varphi_\Theta^2\mathbf{S}_\mathrm{M}\cdot\overset{\triangle}{\mathbf{\Gamma}}_\mathrm{M}, \tag{A10}$$

where $\check{\mathbf{S}} = \mathbf{F}_\Theta^{\mathrm{T}}\mathbf{S}_\mathrm{M}\mathbf{F}_\Theta = \varphi_\Theta^2\mathbf{S}_\mathrm{M}$ is drawn on. The insertion of expressions (A2), (A5) and (A10) into Equation (A1) yields

$$\tilde{\mathbf{T}}\cdot\dot{\mathbf{E}} = \varphi_\Theta^2\varphi_a^2\mathbf{S}_\mathrm{M}\cdot\overset{\triangle}{\mathbf{\Gamma}}_\mathrm{M} + \varphi_a^2\varphi_\Theta\frac{\partial\varphi_\Theta}{\partial\Theta}(\mathrm{tr}\,\mathbf{S}_\mathrm{M})\dot{\Theta} + \varphi_a\varphi_\Theta^2\frac{\partial\varphi_a}{\partial a}(\mathrm{tr}\,\mathbf{S}_\mathrm{M})\dot{a} \tag{A11}$$

for the stress power. Here, all terms are related to the intermediate mechanical configuration.

Appendix C. Thermodynamical Consistence

The specific free energy ψ depends on the mechanical strain $\mathbf{E}_\mathrm{M}$ in this model, the elastic strain ε_e, the strain variable related to the plastic element $\tilde{\varepsilon}_\mathrm{k}$, a softening variable k, the temperature Θ, and the aging variable a

$$\psi = \hat{\psi}(\mathbf{E}_\mathrm{M}, \varepsilon_\mathrm{e}, \tilde{\varepsilon}_\mathrm{k}, k, \Theta, a). \tag{A12}$$

We assume an additive decomposition of the total specific free energy into an elastic part $\psi_\mathrm{eq}^\mathrm{e}$, a plastic (hysteretic) part $\psi_\mathrm{eq}^\mathrm{h}$, an overstress part ψ_ov, a thermal ψ_Θ, and an aging part ψ_a

$$\psi = \psi_\mathrm{eq}^\mathrm{e}(\mathbf{E}_\mathrm{M}) + \psi_\mathrm{eq}^\mathrm{h}(\tilde{\varepsilon}_\mathrm{k}, \Theta) + \psi_\mathrm{ov}(\varepsilon_\mathrm{e}, k) + \psi_\Theta(\Theta) + \psi_a(a). \tag{A13}$$

The time derivative of the free energy is equal to

$$\dot{\psi} = \frac{\partial\psi}{\partial\mathbf{E}_\mathrm{M}}\cdot\dot{\mathbf{E}}_\mathrm{M} + \frac{\partial\psi}{\partial\tilde{\varepsilon}_\mathrm{k}}\cdot\dot{\tilde{\varepsilon}}_\mathrm{k} + \frac{\partial\psi}{\partial\varepsilon_\mathrm{e}}\cdot\dot{\varepsilon}_\mathrm{e} + \frac{\partial\psi}{\partial k}\dot{k} + \frac{\partial\psi}{\partial\Theta}\dot{\Theta} + \frac{\partial\psi}{\partial a}\dot{a}. \tag{A14}$$

This has to be considered within the Clausius-Duhem inequality, see [48],

$$\frac{1}{\rho_\mathrm{R}}\tilde{\mathbf{T}}\cdot\dot{\mathbf{E}} - \dot{\psi} - s\dot{\Theta} - \frac{1}{\rho_\mathrm{R}\Theta}\vec{q}_R\cdot\vec{g}_R \geq 0. \tag{A15}$$

By inserting the stress power (A11) and the computed time derivative of the specific free energy (A14) into the Clausius-Duhem inequality (A15), we arrive at

$$\frac{1}{\rho_\mathrm{R}}\left(\varphi_\Theta^2\varphi_a^2\mathbf{S}_\mathrm{M}\cdot\overset{\triangle}{\boldsymbol{\Gamma}}_\mathrm{M}+\varphi_a^2\varphi_\Theta\frac{\partial\varphi_\Theta}{\partial\Theta}(\mathrm{tr}\,\mathbf{S}_\mathrm{M})\dot{\Theta}+\varphi_a\varphi_\Theta^2\frac{\partial\varphi_a}{\partial a}(\mathrm{tr}\,\mathbf{S}_\mathrm{M})\dot{a}\right)-\frac{\partial\psi}{\partial\mathbf{E}_\mathrm{M}}\cdot\dot{\mathbf{E}}_\mathrm{M}$$
$$-\frac{\partial\psi}{\partial\boldsymbol{\varepsilon}_\mathrm{e}}\cdot\dot{\boldsymbol{\varepsilon}}_\mathrm{e}-\frac{\partial\psi}{\partial\tilde{\boldsymbol{\varepsilon}}_\mathrm{k}}\cdot\dot{\tilde{\boldsymbol{\varepsilon}}}_\mathrm{k}-\frac{\partial\psi}{\partial\Theta}\dot{\Theta}-\frac{\partial\psi}{\partial k}\dot{k}-\frac{\partial\psi}{\partial a}\dot{a}-s\dot{\Theta}-\frac{1}{\rho_\mathrm{R}\Theta}\vec{q}_R\cdot\vec{g}_R\geq 0. \tag{A16}$$

The term $\partial\psi/\partial\mathbf{E}_\mathrm{M}\cdot\dot{\mathbf{E}}_\mathrm{M}$ can be expressed by

$$\frac{\partial\psi}{\partial\mathbf{E}_\mathrm{M}}\cdot\dot{\mathbf{E}}_\mathrm{M}=\mathbf{F}_\mathrm{M}\frac{\partial\psi}{\partial\mathbf{E}_\mathrm{M}}\mathbf{F}_\mathrm{M}^\mathrm{T}\cdot\overset{\triangle}{\boldsymbol{\Gamma}}_\mathrm{M} \tag{A17}$$

and the total stress in the mechanical configuration $\hat{\chi}_t$ can be decomposed into the elastic, plastic, and overstress part

$$\mathbf{S}_\mathrm{M}=\mathbf{S}_\mathrm{Meq}+\mathbf{S}_\mathrm{Mov}=\mathbf{S}_\mathrm{Meq}^\mathrm{e}+\mathbf{S}_\mathrm{Meq}^\mathrm{h}+\mathbf{S}_\mathrm{Mov}. \tag{A18}$$

With the expressions (A17) and (A18) as well as by rearranging the terms, inequality (A16) can be expressed by

$$\left(\frac{\varphi_\Theta^2\varphi_a^2}{\rho_\mathrm{R}}\mathbf{S}_\mathrm{Meq}^\mathrm{e}-\mathbf{F}_\mathrm{M}\frac{\partial\psi}{\partial\mathbf{E}_\mathrm{M}}\mathbf{F}_\mathrm{M}^\mathrm{T}\right)\cdot\overset{\triangle}{\boldsymbol{\Gamma}}_\mathrm{M}+\frac{\varphi_\Theta^2\varphi_a^2}{\rho_\mathrm{R}}\left(\mathbf{S}_\mathrm{Meq}^\mathrm{h}+\mathbf{S}_\mathrm{Mov}\right)\cdot\overset{\triangle}{\boldsymbol{\Gamma}}_\mathrm{M}$$
$$-\frac{\partial\psi}{\partial\boldsymbol{\varepsilon}_\mathrm{e}}\cdot\dot{\boldsymbol{\varepsilon}}_\mathrm{e}-\frac{\partial\psi}{\partial\tilde{\boldsymbol{\varepsilon}}_\mathrm{k}}\cdot\dot{\tilde{\boldsymbol{\varepsilon}}}_\mathrm{k}-\frac{\partial\psi}{\partial k}\dot{k}+\left(\frac{\varphi_\Theta\varphi_a^2}{\rho_\mathrm{R}}\frac{\partial\varphi_\Theta}{\partial\Theta}(\mathrm{tr}\,\mathbf{S}_\mathrm{M})-\frac{\partial\psi}{\partial\Theta}-s\right)\dot{\Theta}$$
$$+\left(\varphi_a\varphi_\Theta^2\frac{\partial\varphi_a}{\partial a}(\mathrm{tr}\,\mathbf{S}_\mathrm{M})-\frac{\partial\psi}{\partial a}\right)\dot{a}-\frac{1}{\rho_\mathrm{R}\Theta}\vec{q}_R\cdot\vec{g}_R\geq 0. \tag{A19}$$

A sufficient condition to fulfill this inequality assumes that the elastic stress $\mathbf{S}_\mathrm{Meq}^\mathrm{e}$ and the entropy s are given by

$$\mathbf{S}_\mathrm{Meq}^\mathrm{e}=\frac{\rho_\mathrm{R}}{\varphi_\Theta^2\varphi_a^2}\mathbf{F}_\mathrm{M}\frac{\partial\psi}{\partial\mathbf{E}_\mathrm{M}}\mathbf{F}_\mathrm{M}^\mathrm{T}, \tag{A20}$$

$$s=\frac{\varphi_\Theta\varphi_a^2}{\rho_\mathrm{R}}\frac{\partial\varphi_\Theta}{\partial\Theta}(\mathrm{tr}\,\mathbf{S}_\mathrm{M})-\frac{\partial\psi}{\partial\Theta}. \tag{A21}$$

Next, the remaining terms of the Clausius-Duhem inequality (A19) have to be discussed. To this end, inequality (A19) is decomposed in the following parts for the different contributions

$$\frac{\varphi_\Theta^2\varphi_a^2}{\rho_\mathrm{R}}\mathbf{S}_\mathrm{Meq}^\mathrm{h}\cdot\overset{\triangle}{\boldsymbol{\Gamma}}_\mathrm{M}-\frac{\partial\psi}{\partial\tilde{\boldsymbol{\varepsilon}}_\mathrm{k}}\cdot\dot{\tilde{\boldsymbol{\varepsilon}}}_\mathrm{k}\geq 0 \qquad \text{plastic element} \tag{A22}$$

$$\frac{\varphi_\Theta^2\varphi_a^2}{\rho_\mathrm{R}}\mathbf{S}_\mathrm{Mov}\cdot\overset{\triangle}{\boldsymbol{\Gamma}}_\mathrm{M}-\frac{\partial\psi}{\partial\boldsymbol{\varepsilon}_\mathrm{e}}\cdot\dot{\boldsymbol{\varepsilon}}_\mathrm{e}\geq 0 \qquad \text{Maxwell-element} \tag{A23}$$

$$-\frac{\partial\psi}{\partial k}\dot{k}\geq 0 \qquad \text{softening} \tag{A24}$$

$$\left(\varphi_a\varphi_\Theta^2\frac{\partial\varphi_a}{\partial a}(\mathrm{tr}\,\mathbf{S}_\mathrm{M})-\frac{\partial\psi}{\partial a}\right)\dot{a}\geq 0 \qquad \text{aging} \tag{A25}$$

$$-\frac{1}{\rho_\mathrm{R}\Theta}\vec{q}_R\cdot\vec{g}_R\geq 0 \qquad \text{thermal conduction} \tag{A26}$$

which are discussed subsequently.

Appendix C.1. Maxwell-Element

To fulfill inequality (A23), we proceed as follows. The covariant Oldroyd derivative of the mechanical strain is decomposed into the sum of the elastic part $\overset{\triangle}{\boldsymbol{\Gamma}}_{\mathrm{e}}$ and the viscous part $\overset{\triangle}{\boldsymbol{\Gamma}}_{\mathrm{v}}$. The term $\mathbf{S}_{\mathrm{Mov}} \cdot \overset{\triangle}{\boldsymbol{\Gamma}}_{\mathrm{M}}$ is now expressed relative to the viscous intermediate configuration $\check{\chi}_t$,

$$\mathbf{S}_{\mathrm{Mov}} \cdot \overset{\triangle}{\boldsymbol{\Gamma}}_{\mathrm{M}} = \check{\mathbf{S}}_{\mathrm{ov}} \cdot \overset{\triangle}{\boldsymbol{\varepsilon}}_{\mathrm{M}} = \check{\mathbf{S}}_{\mathrm{ov}} \cdot (\overset{\triangle}{\boldsymbol{\varepsilon}}_{\mathrm{e}} + \overset{\triangle}{\boldsymbol{\varepsilon}}_{\mathrm{v}}). \tag{A27}$$

Additionally, the Oldroyd derivative

$$\overset{\triangle}{\boldsymbol{\varepsilon}}_{\mathrm{e}} = \dot{\boldsymbol{\varepsilon}}_{\mathrm{e}} + \mathbf{L}_{\mathrm{v}}^{\mathrm{T}} \boldsymbol{\varepsilon}_{\mathrm{e}} + \boldsymbol{\varepsilon}_{\mathrm{e}} \mathbf{L}_{\mathrm{v}} \tag{A28}$$

is considered, see Figure A2. Inserting Equation (A27) and (A28) into Equation (A23) leads to

$$\left(\frac{\varphi_{\Theta}^2 \varphi_a^2}{\rho_{\mathrm{R}}} \check{\mathbf{S}}_{\mathrm{ov}} - \frac{\partial \psi}{\partial \boldsymbol{\varepsilon}_{\mathrm{e}}} \right) \cdot \overset{\triangle}{\boldsymbol{\varepsilon}}_{\mathrm{e}} + \frac{\varphi_{\Theta}^2 \varphi_a^2}{\rho_{\mathrm{R}}} \check{\mathbf{S}}_{\mathrm{ov}} \cdot \overset{\triangle}{\boldsymbol{\varepsilon}}_{\mathrm{v}} + \frac{\partial \psi}{\partial \boldsymbol{\varepsilon}_{\mathrm{e}}} \cdot (\mathbf{L}_{\mathrm{v}}^{\mathrm{T}} \boldsymbol{\varepsilon}_{\mathrm{e}} + \boldsymbol{\varepsilon}_{\mathrm{e}} \mathbf{L}_{\mathrm{v}}) \geq 0. \tag{A29}$$

From this expression, we have a sufficient condition for the term of the overstress with the following definition

$$\check{\mathbf{S}}_{\mathrm{ov}} = \frac{\rho_{\mathrm{R}}}{\varphi_{\Theta}^2 \varphi_a^2} \frac{\partial \psi}{\partial \boldsymbol{\varepsilon}_{\mathrm{e}}}. \tag{A30}$$

With definition (A30), the remaining term of Equation (A29) can be simplified to

$$\frac{\varphi_{\Theta}^2 \varphi_a^2}{\rho_{\mathrm{R}}} \check{\mathbf{S}}_{\mathrm{ov}} \cdot \overset{\triangle}{\boldsymbol{\varepsilon}}_{\mathrm{v}} + \frac{\partial \psi}{\partial \boldsymbol{\varepsilon}_{\mathrm{e}}} \cdot (\mathbf{L}_{\mathrm{v}}^{\mathrm{T}} \boldsymbol{\varepsilon}_{\mathrm{e}} + \boldsymbol{\varepsilon}_{\mathrm{e}} \mathbf{L}_{\mathrm{v}}) = \frac{\varphi_{\Theta}^2 \varphi_a^2}{\rho_{\mathrm{R}}} \mathbf{C}_{\mathrm{e}} \check{\mathbf{S}}_{\mathrm{ov}} \cdot \overset{\triangle}{\boldsymbol{\varepsilon}}_{\mathrm{v}}, \tag{A31}$$

with $\mathbf{C}_{\mathrm{e}} = \mathbf{F}_{\mathrm{e}}^{\mathrm{T}} \mathbf{F}_{\mathrm{e}}$, as well as making use of the symmetry of the strain tensor $\boldsymbol{\varepsilon}_{\mathrm{e}} = (\mathbf{C}_{\mathrm{e}} - \mathbf{I})/2$, the definition of $\overset{\triangle}{\boldsymbol{\varepsilon}}_{\mathrm{v}} = (\mathbf{L}_{\mathrm{v}}^{\mathrm{T}} + \mathbf{L}_{\mathrm{v}})/2$ and the isotropy of the "elasticity relation" $\partial \psi / \partial \boldsymbol{\varepsilon}_{\mathrm{e}}$, see also ([54], p. 45). In this way, the following expression is obtained for the Maxwell-element,

$$\frac{\varphi_{\Theta}^2 \varphi_a^2}{\rho_{\mathrm{R}}} \mathbf{C}_{\mathrm{e}} \check{\mathbf{S}}_{\mathrm{ov}} \cdot \overset{\triangle}{\boldsymbol{\varepsilon}}_{\mathrm{v}} \geq 0. \tag{A32}$$

Appendix C.2. Plastic Element

Next, inequality (A22) has to be fulfilled. The considerations made for this element are analogous to the Maxwell-element. The term $\mathbf{S}_{\mathrm{Meq}}^{\mathrm{h}} \cdot \overset{\triangle}{\boldsymbol{\Gamma}}_{\mathrm{M}}$ is expressed with quantities relative to the plastic intermediate configuration $\tilde{\chi}_t$

$$\mathbf{S}_{\mathrm{Meq}}^{\mathrm{h}} \cdot \overset{\triangle}{\boldsymbol{\Gamma}}_{\mathrm{M}} = \tilde{\mathbf{S}}_{\mathrm{eq}}^{\mathrm{h}} \cdot \overset{\triangle}{\tilde{\boldsymbol{\varepsilon}}}_{\mathrm{M}} = \tilde{\mathbf{S}}_{\mathrm{eq}}^{\mathrm{h}} \cdot (\overset{\triangle}{\tilde{\boldsymbol{\varepsilon}}}_{\mathrm{k}} + \overset{\triangle}{\tilde{\boldsymbol{\varepsilon}}}_{\mathrm{p}}). \tag{A33}$$

The Oldroyd derivative $\overset{\triangle}{\tilde{\boldsymbol{\varepsilon}}}_{\mathrm{k}}$ reads

$$\overset{\triangle}{\tilde{\boldsymbol{\varepsilon}}}_{\mathrm{k}} = \dot{\tilde{\boldsymbol{\varepsilon}}}_{\mathrm{k}} + \mathbf{L}_{\mathrm{p}}^{\mathrm{T}} \tilde{\boldsymbol{\varepsilon}}_{\mathrm{k}} + \tilde{\boldsymbol{\varepsilon}}_{\mathrm{k}} \mathbf{L}_{\mathrm{p}}, \tag{A34}$$

see Figure A2. Inserting Equation (A33) and (A34) into Equation (A22) yields

$$\left(\frac{\varphi_{\Theta}^2 \varphi_a^2}{\rho_{\mathrm{R}}} \tilde{\mathbf{S}}_{\mathrm{eq}}^{\mathrm{h}} - \frac{\partial \psi}{\partial \tilde{\boldsymbol{\varepsilon}}_{\mathrm{k}}} \right) \cdot \overset{\triangle}{\tilde{\boldsymbol{\varepsilon}}}_{\mathrm{k}} + \frac{\varphi_{\Theta}^2 \varphi_a^2}{\rho_{\mathrm{R}}} \tilde{\mathbf{S}}_{\mathrm{eq}}^{\mathrm{h}} \cdot \overset{\triangle}{\tilde{\boldsymbol{\varepsilon}}}_{\mathrm{p}} + \frac{\partial \psi}{\partial \tilde{\boldsymbol{\varepsilon}}_{\mathrm{k}}} \cdot (\mathbf{L}_{\mathrm{p}}^{\mathrm{T}} \tilde{\boldsymbol{\varepsilon}}_{\mathrm{k}} + \tilde{\boldsymbol{\varepsilon}}_{\mathrm{k}} \mathbf{L}_{\mathrm{p}}) \geq 0. \tag{A35}$$

First, we assume from the first term, with definition (31), the term (A35) can be simplified to

$$\frac{\varphi_\Theta^2\varphi_a^2}{\rho_\mathrm{R}}\tilde{\mathbf{S}}_\mathrm{eq}^\mathrm{h}\cdot\overset{\triangle}{\tilde{\varepsilon}}_\mathrm{p}+\frac{\partial\psi}{\partial\tilde{\varepsilon}_\mathrm{k}}\cdot(\mathbf{L}_\mathrm{p}^\mathrm{T}\tilde{\varepsilon}_\mathrm{k}+\tilde{\varepsilon}_\mathrm{k}\mathbf{L}_\mathrm{p})=\frac{\varphi_\Theta^2\varphi_a^2}{\rho_\mathrm{R}}\mathbf{C}_\mathrm{k}\tilde{\mathbf{S}}_\mathrm{eq}^\mathrm{h}\cdot\overset{\triangle}{\tilde{\varepsilon}}_\mathrm{p}, \tag{A36}$$

with $\mathbf{C}_\mathrm{k}=\mathbf{F}_\mathrm{k}^\mathrm{T}\mathbf{F}_\mathrm{k}$, as well as using the symmetry of the strain tensor $\tilde{\varepsilon}_\mathrm{k}=(\mathbf{C}_\mathrm{k}-\mathbf{I})/2$, the definition of $\overset{\triangle}{\tilde{\varepsilon}}_\mathrm{p}=(\mathbf{L}_\mathrm{p}^\mathrm{T}+\mathbf{L}_\mathrm{p})/2$ and the isotropy of the "elasticity relation" $\partial\psi/\partial\tilde{\varepsilon}_\mathrm{k}$. Then, the term of the Clausius-Duhem inequality related to the plastic element

$$\frac{\varphi_\Theta^2\varphi_a^2}{\rho_\mathrm{R}}\mathbf{C}_\mathrm{k}\tilde{\mathbf{S}}_\mathrm{eq}^\mathrm{h}\cdot\overset{\triangle}{\tilde{\varepsilon}}_\mathrm{p}\geq 0. \tag{A37}$$

In the following, we evaluate the Clausius-Duhem inequality (A19) by inserting expressions (A32) and (A37) leading to

$$\begin{aligned}&\frac{\varphi_\Theta^2\varphi_a^2}{\rho_\mathrm{R}}\mathbf{C}_\mathrm{k}\tilde{\mathbf{S}}_\mathrm{eq}^\mathrm{h}\cdot\overset{\triangle}{\tilde{\varepsilon}}_\mathrm{p}+\frac{\varphi_\Theta^2\varphi_a^2}{\rho_\mathrm{R}}\mathbf{C}_\mathrm{e}\check{\mathbf{S}}_\mathrm{ov}\cdot\overset{\triangle}{\varepsilon}_\mathrm{v}-\frac{\partial\psi}{\partial k}\dot{k}\\&+\left(\varphi_a\varphi_\Theta^2\frac{\partial\varphi_a}{\partial a}(\mathrm{tr}\,\mathbf{S}_\mathrm{M})-\frac{\partial\psi}{\partial a}\right)\dot{a}-\frac{1}{\rho_\mathrm{R}\Theta}\vec{q}_R\cdot\vec{g}_R\geq 0.\end{aligned} \tag{A38}$$

Thus, the Clausius-Duhem inequality is fulfilled in a sufficient manner if the following relations hold:

$$\overset{\triangle}{\tilde{\varepsilon}}_\mathrm{p}=\beta_\mathbf{Y}\dot{s}_\mathrm{M}\mathbf{C}_\mathrm{k}\tilde{\mathbf{S}}_\mathrm{eq}^\mathrm{h},\qquad\beta_\mathbf{Y},\dot{s}_\mathrm{M}>0, \tag{A39}$$

$$\overset{\triangle}{\varepsilon}_\mathrm{v}=\frac{1}{\hat{\eta}}\mathbf{C}_\mathrm{e}\check{\mathbf{S}}_\mathrm{ov},\qquad\hat{\eta}>0, \tag{A40}$$

$$\dot{k}\geq 0,\qquad\frac{\partial\psi}{\partial k}\leq 0, \tag{A41}$$

$$\dot{a}=\beta_g\left(\varphi_a\frac{\partial\varphi_a}{\partial a}(\mathrm{tr}\,\check{\mathbf{S}})-\frac{\partial\psi}{\partial a}\right),\qquad\beta_g>0, \tag{A42}$$

$$\vec{q}_R=-\boldsymbol{\kappa}_\Theta^\mathrm{R}\mathrm{Grad}\,\Theta,\qquad\text{and}\qquad\vec{g}_R=\mathrm{Grad}\,\Theta \tag{A43}$$

In Equation (42), the term $\boldsymbol{\kappa}_\Theta^\mathrm{R}$ represents the thermal conductivity tensor.

Equations (38) and (39) fulfill the condition of plastic incompressibility (since $\det\bar{\mathbf{F}}_\mathrm{p}=1$ and $\det\bar{\mathbf{F}}_\mathrm{v}=1$), which can be shown considering the time derivatives

$$\frac{\mathrm{d}}{\mathrm{d}t}(\det\bar{\mathbf{F}}_\mathrm{p})=(\det\bar{\mathbf{F}}_\mathrm{p})(\mathrm{tr}\,\mathbf{L}_\mathrm{p})=(\det\bar{\mathbf{F}}_\mathrm{p})(\mathrm{tr}\,\mathbf{D}_\mathrm{p})=0\rightarrow\mathrm{tr}\,\mathbf{D}_\mathrm{p}=\mathrm{tr}\,\overset{\triangle}{\tilde{\varepsilon}}_\mathrm{p}=0, \tag{A44}$$

$$\frac{\mathrm{d}}{\mathrm{d}t}(\det\bar{\mathbf{F}}_\mathrm{v})=(\det\bar{\mathbf{F}}_\mathrm{v})(\mathrm{tr}\,\mathbf{L}_\mathrm{v})=(\det\bar{\mathbf{F}}_\mathrm{v})(\mathrm{tr}\,\mathbf{D}_\mathrm{v})=0\rightarrow\mathrm{tr}\,\mathbf{D}_\mathrm{v}=\mathrm{tr}\,\overset{\triangle}{\varepsilon}_\mathrm{v}=0. \tag{A45}$$

Appendix D. Choice of Free Energies

In the following, the different components of the specific free energy in Equation (A13) are defined.

Appendix D.1. Spring Element

The elastic component $\psi_\mathrm{eq}^\mathrm{e}(\mathbf{E}_\mathrm{M})$ is modeled using nearly incompressible formulation. It is decomposed into a volumetric and an isochoric part

$$\rho_\mathrm{R}\psi_\mathrm{eq}^\mathrm{e}(\mathbf{E}_\mathrm{M})=U(J_\mathrm{M})+\bar{\omega}(\bar{\mathbf{C}}_\mathrm{M}). \tag{A46}$$

The volume changing part $U(J_\mathrm{M})$ is chosen according to [64,84] and depends on the determinant of the mechanical deformation gradient $J_\mathrm{M} := \det \mathbf{F}_\mathrm{M}$

$$U(J_\mathrm{M}) = \frac{K}{50}(J_\mathrm{M}^5 + J_\mathrm{M}^{-5} - 2). \tag{A47}$$

This function fulfills the condition of convexity, and provides a physical material response extreme cases for tension and compression. The isochoric part $\bar{\omega}(\bar{\mathbf{C}}_\mathrm{M})$ is modeled using a Neo-Hookean ansatz. It depends on the unimodular mechanical right Cauchy-Green tensor $\bar{\mathbf{C}}_\mathrm{M} = \bar{\mathbf{C}}$—which is equal to the total unimodular Cauchy-Green tensor in the model proposed here—considering that the aging and the thermal part are purely volumetric,

$$\bar{\omega}(\bar{\mathbf{C}}_\mathrm{M}) = c_{10}(I_{\bar{\mathbf{C}}_\mathrm{M}} - 3), \qquad \bar{\mathbf{C}}_\mathrm{M} = (\det \mathbf{C}_\mathrm{M})^{-1/3}\mathbf{C}_\mathrm{M}. \tag{A48}$$

This selection of the free energy $\psi^\mathrm{e}_\mathrm{eq}$ results in the following expression for the elastic equilibrium stress considering Equation (29)

$$\begin{aligned}\mathbf{S}^\mathrm{e}_\mathrm{Meq} &= \frac{\rho_\mathrm{R}}{\varphi_\Theta^2\varphi_a^2}\mathbf{F}_\mathrm{M}\frac{\partial\psi}{\partial\mathbf{E}_\mathrm{M}}\mathbf{F}_\mathrm{M}^\mathrm{T} = \frac{2\rho_\mathrm{R}}{\varphi_\Theta^2\varphi_a^2}\mathbf{F}_\mathrm{M}\frac{\partial\psi}{\partial\mathbf{C}_\mathrm{M}}\mathbf{F}_\mathrm{M}^\mathrm{T}\\ &= 2(\varphi_\Theta\varphi_a)^{-2}\mathbf{F}_\mathrm{M}\left(\frac{\mathrm{d}U}{\mathrm{d}\mathbf{C}_\mathrm{M}} + \frac{\mathrm{d}\omega(\bar{\mathbf{C}}_\mathrm{M})}{\mathrm{d}\mathbf{C}_\mathrm{M}}\right)\mathbf{F}_\mathrm{M}^\mathrm{T}.\end{aligned} \tag{A49}$$

The partial derivatives of the free energy (A46) are equal to

$$\frac{\mathrm{d}U(J_\mathrm{M})}{\mathrm{d}\mathbf{C}_\mathrm{M}} = \frac{K}{20}(J_\mathrm{M}^5 - J_\mathrm{M}^{-5})\mathbf{C}_\mathrm{M}^{-1}, \tag{A50}$$

$$\frac{\mathrm{d}\omega(\bar{\mathbf{C}}_\mathrm{M})}{\mathrm{d}\mathbf{C}_\mathrm{M}} = c_{10}J_\mathrm{M}^{-2/3}\mathbf{C}_\mathrm{M}^{-1}\mathbf{C}_\mathrm{M}^\mathrm{D}. \tag{A51}$$

Inserting Equations (A50) and (A51) into Equation (A49), one obtains

$$\mathbf{S}^\mathrm{e}_\mathrm{Meq} = 2(\varphi_\Theta\varphi_a)^{-2}\mathbf{F}_\mathrm{M}\left(\frac{K}{20}(J_\mathrm{M}^5 - J_\mathrm{M}^{-5})\mathbf{C}_\mathrm{M}^{-1} + c_{10}J_\mathrm{M}^{-2/3}\mathbf{C}_\mathrm{M}^{-1}\mathbf{C}_\mathrm{M}^\mathrm{D}\right)\mathbf{F}_\mathrm{M}^\mathrm{T} \tag{A52}$$

$$= (\varphi_\Theta\varphi_a)^{-2}\frac{K}{10}(J_\mathrm{M}^5 - J_\mathrm{M}^{-5})\mathbf{I} + (\varphi_\Theta\varphi_a)^{-2}2c_{10}\bar{\mathbf{B}}_\mathrm{M}^\mathrm{D}. \tag{A53}$$

The stress is pulled back into the reference configuration

$$\tilde{\mathbf{T}}^\mathrm{e}_\mathrm{eq} = \mathbf{F}_\mathrm{M}^{-1}\mathbf{S}^\mathrm{e}_\mathrm{Meq}\mathbf{F}_\mathrm{M}^{-\mathrm{T}} = (\varphi_\Theta\varphi_a)^{-2}\left(\frac{K}{10}(J_\mathrm{M}^5 - J_\mathrm{M}^{-5})\mathbf{C}_\mathrm{M}^{-1} + 2c_{10}J_\mathrm{M}^{-2/3}\mathbf{C}_\mathrm{M}^{-1}\mathbf{C}_\mathrm{M}^\mathrm{D}\right), \tag{A54}$$

Making use of the relations

$$\mathbf{F}_\mathrm{M} = (\varphi_a\varphi_\Theta)^{-1}\mathbf{F}, \qquad J_\mathrm{M} = (\varphi_a\varphi_\Theta)^{-3}J, \qquad J = \det\mathbf{F} \tag{A55}$$

$$\mathbf{C}_\mathrm{M} = \mathbf{F}_\mathrm{M}^\mathrm{T}\mathbf{F}_\mathrm{M} = (\varphi_a\varphi_\Theta)^{-2}\mathbf{C}, \qquad \mathbf{C}_\mathrm{M}^{-1} = \mathbf{F}_\mathrm{M}^{-1}\mathbf{F}_\mathrm{M}^{-\mathrm{T}} = (\varphi_a\varphi_\Theta)^2\mathbf{C}^{-1}, \tag{A56}$$

the elastic equilibrium stress part can be decomposed into two components

$$\tilde{\mathbf{T}}^\mathrm{e}_\mathrm{vol} = \frac{K}{10}\left(J_\mathrm{M}^5 - J_\mathrm{M}^{-5}\right)\mathbf{C}^{-1}, \qquad J_\mathrm{M} = \frac{J}{(\varphi_a\varphi_\Theta)^3}, \tag{A57}$$

$$\tilde{\mathbf{T}}^\mathrm{e}_\mathrm{iso} = 2c_{10}J^{-2/3}\mathbf{C}^{-1}\mathbf{C}^\mathrm{D}. \tag{A58}$$

Both stress tensors are symmetric. These tensors can be expressed by tensors operating on the current configuration with the push-forward operation $\mathbf{S}^{\mathrm{e}}_{\mathrm{vol}} = \mathbf{F}\tilde{\mathbf{T}}^{\mathrm{e}}_{\mathrm{vol}}\mathbf{F}^{\mathrm{T}}$ and $\mathbf{S}^{\mathrm{e}}_{\mathrm{iso}} = \mathbf{F}\tilde{\mathbf{T}}^{\mathrm{e}}_{\mathrm{iso}}\mathbf{F}^{\mathrm{T}}$

$$\mathbf{S}^{\mathrm{e}}_{\mathrm{vol}} = \frac{K}{10}\left(J_{\mathrm{M}}^{5} - J_{\mathrm{M}}^{-5}\right)\mathbf{I}, \tag{A59}$$

$$\mathbf{S}^{\mathrm{e}}_{\mathrm{iso}} = 2c_{10}\bar{\mathbf{B}}^{\mathrm{D}}_{\mathrm{M}}. \tag{A60}$$

These two stress tensors correspond to a purely hydrostatic stress $\mathbf{S}^{\mathrm{e}}_{\mathrm{vol}}$ related to the volume-changing energy function $U(J_{\mathrm{M}})$, and a deviatoric stress $\mathbf{S}^{\mathrm{e}}_{\mathrm{iso}}$ related to the Neo-Hookean ansatz $\omega(\bar{\mathbf{C}}_{\mathrm{M}})$.

Appendix D.2. Plastic Element and Maxwell-Element

The Maxwell and the plastic element are treated similarly since both have a similar behavior with the difference that the Maxwell-element is rate-dependent and the plastic element rate-independent. The Maxwell-element can be modeled with a Neo-Hooke ansatz

$$\bar{\psi}_{\mathrm{ov}}(\boldsymbol{\varepsilon}_{\mathrm{e}}) = \bar{\omega}_{\mathrm{ov}}(\bar{\mathbf{C}}_{\mathrm{e}}(\mathbf{C}_{\mathrm{e}})), \tag{A61}$$

see [52]. A small modification is included to this ansatz for the modeling of the softening in the case of the overstress and the temperature for the plastic element.

Expressions for the stresses $\tilde{\mathbf{S}}^{\mathrm{h}}_{\mathrm{eq}}$ and $\check{\mathbf{S}}_{\mathrm{ov}}$ can be computed considering Equations (25), (26), (30) and (31), in an analogous way to Equation (A51), obtaining

$$\tilde{\mathbf{S}}^{\mathrm{h}}_{\mathrm{eq}} = \frac{\rho_{\mathrm{R}}}{\varphi_{\Theta}^{2}\varphi_{a}^{2}}\frac{\partial\psi^{\mathrm{h}}_{\mathrm{eq}}}{\partial\tilde{\boldsymbol{\varepsilon}}_{\mathrm{k}}} = 2\mu_{\mathrm{eq}}(\varphi_{\Theta}\varphi_{a})^{-2}\mathbf{C}_{\mathrm{k}}^{-1}\bar{\mathbf{C}}^{\mathrm{D}}_{\mathrm{k}}, \tag{A62}$$

$$\check{\mathbf{S}}_{\mathrm{ov}} = \frac{\rho_{\mathrm{R}}}{\varphi_{\Theta}^{2}\varphi_{a}^{2}}\frac{\partial\psi_{\mathrm{ov}}}{\partial\boldsymbol{\varepsilon}_{\mathrm{e}}} = 2\mu_{\mathrm{ov}}(\varphi_{\Theta}\varphi_{a})^{-2}\mathbf{C}_{\mathrm{e}}^{-1}\bar{\mathbf{C}}^{\mathrm{D}}_{\mathrm{e}}. \tag{A63}$$

With a pull-back operation, the plastic stress and the overstress can be expressed with the second Piola-Kirchhoff-type stress relative to the reference configuration $\tilde{\mathbf{T}}^{\mathrm{h}}_{\mathrm{eq}} = \bar{\mathbf{F}}_{\mathrm{p}}^{-1}\mathbf{S}^{\mathrm{h}}_{\mathrm{Meq}}\bar{\mathbf{F}}_{\mathrm{p}}^{-\mathrm{T}}$ and $\tilde{\mathbf{T}}_{\mathrm{ov}} = \bar{\mathbf{F}}_{\mathrm{v}}^{-1}\check{\mathbf{S}}_{\mathrm{ov}}\bar{\mathbf{F}}_{\mathrm{v}}^{-\mathrm{T}}$ leading to

$$\tilde{\mathbf{T}}^{\mathrm{h}}_{\mathrm{eq}} = 2\mu_{\mathrm{eq}}(\varphi_{\Theta}\varphi_{a})^{-2}\bar{\mathbf{F}}_{\mathrm{p}}^{-1}\mathbf{C}_{\mathrm{k}}^{-1}\bar{\mathbf{C}}^{\mathrm{D}}_{\mathrm{k}}\bar{\mathbf{F}}_{\mathrm{p}}^{-\mathrm{T}} = 2\mu_{\mathrm{eq}}J^{-2/3}\mathbf{C}^{-1}(\mathbf{C}\bar{\mathbf{C}}_{\mathrm{p}}^{-1})^{\mathrm{D}}, \tag{A64}$$

$$\tilde{\mathbf{T}}_{\mathrm{ov}} = 2\mu_{\mathrm{ov}}(\varphi_{\Theta}\varphi_{a})^{-2}\bar{\mathbf{F}}_{\mathrm{v}}^{-1}\mathbf{C}_{\mathrm{e}}^{-1}\bar{\mathbf{C}}^{\mathrm{D}}_{\mathrm{e}}\bar{\mathbf{F}}_{\mathrm{v}}^{-\mathrm{T}} = 2\mu_{\mathrm{ov}}J^{-2/3}\mathbf{C}^{-1}(\mathbf{C}\bar{\mathbf{C}}_{\mathrm{v}}^{-1})^{\mathrm{D}}. \tag{A65}$$

Expressing these tensors with quantities of the current configuration, $\mathbf{S}^{\mathrm{h}}_{\mathrm{eq}} = \mathbf{F}\tilde{\mathbf{T}}^{\mathrm{h}}_{\mathrm{eq}}\mathbf{F}^{\mathrm{T}}$ and $\mathbf{S}_{\mathrm{ov}} = \mathbf{F}\tilde{\mathbf{T}}_{\mathrm{ov}}\mathbf{F}^{\mathrm{T}}$, one can see that the plastic stress part $\mathbf{S}^{\mathrm{h}}_{\mathrm{eq}}$ and the overstress $\mathbf{S}_{\mathrm{ov}}$ in the current configuration are purely deviatoric

$$\mathbf{S}^{\mathrm{h}}_{\mathrm{eq}} = 2\mu_{\mathrm{eq}}\bar{\mathbf{B}}^{\mathrm{D}}_{\mathrm{k}}, \tag{A66}$$

$$\mathbf{S}_{\mathrm{ov}} = 2\mu_{\mathrm{ov}}\bar{\mathbf{B}}^{\mathrm{D}}_{\mathrm{e}}, \tag{A67}$$

which shows that $\mathbf{S}^{\mathrm{e}}_{\mathrm{vol}}$ is the only volumetric component of the stress in the current configuration. Moreover, $\mathbf{S}^{\mathrm{e}}_{\mathrm{vol}}$ is also the only component connected to elastic volumetric processes, see Equation (A59).

Appendix D.3. Aging

The aging component of the specific free energy ψ_a is defined with a linear relation by

$$\rho_{\mathrm{R}}\psi_{a}(a) = C_1 - C_2 a, \tag{A68}$$

with C_1 and C_2 are material parameters.

Appendix E. Heat Conduction Equation and Thermal Properties

The heat conduction equation describes the temperature evolution of a material body during a thermo-mechanical loading process, see [48]. It is derived from the local form of the balance of energy in case that the internal energy is expressed in dependence of the Helmholtz free energy and specific entropy $e = \psi + s\Theta$

$$\dot{\psi} + s\dot{\Theta} + \Theta\dot{s} = -\frac{1}{\rho_{\mathrm{R}}}\mathrm{Div}\,\vec{q}_R + \frac{1}{\rho_{\mathrm{R}}}\tilde{\mathbf{T}} \cdot \dot{\mathbf{E}} + r. \tag{A69}$$

It can be abbreviated by

$$\Theta\dot{s} = -\frac{1}{\rho_{\mathrm{R}}}\mathrm{Div}\,\vec{q}_R + \delta + r. \tag{A70}$$

with the term $\vec{q}_R$ representing the Piola-Kirchhoff heat flux, $\delta = \tilde{\mathbf{T}} \cdot \dot{\mathbf{E}}/\rho_{\mathrm{R}} - \dot{\psi} - s\dot{\Theta}$ displaying the internal inelastic dissipation and r a volumetric heat source. The time derivative of the entropy (A21) is computed applying the chain rule

$$\dot{s} = \frac{\partial s}{\partial \mathbf{E}_{\mathrm{M}}} \cdot \dot{\mathbf{E}}_{\mathrm{M}} + \frac{\partial s}{\partial \Theta}\dot{\Theta} + \frac{\partial s}{\partial \tilde{\varepsilon}_{\mathrm{k}}} \cdot \dot{\tilde{\varepsilon}}_{\mathrm{k}} + \frac{\partial s}{\partial a}\dot{a}. \tag{A71}$$

Inserting Equation (A71) into Equation (A70) leads to

$$\Theta\frac{\partial s}{\partial \Theta}\dot{\Theta} = -\frac{1}{\rho_{\mathrm{R}}}\mathrm{Div}\,\vec{q}_R + \delta + r - \Theta\left(\frac{\partial s}{\partial \mathbf{E}_{\mathrm{M}}} \cdot \dot{\mathbf{E}}_{\mathrm{M}} + \frac{\partial s}{\partial \tilde{\varepsilon}_{\mathrm{k}}} \cdot \dot{\tilde{\varepsilon}}_{\mathrm{k}} + \frac{\partial s}{\partial a}\dot{a}\right). \tag{A72}$$

The heat production due to internal dissipation ω is obtained by

$$\omega = \delta - \Theta\left(\frac{\partial s}{\partial \mathbf{E}_{\mathrm{M}}} \cdot \dot{\mathbf{E}}_{\mathrm{M}} + \frac{\partial s}{\partial \tilde{\varepsilon}_{\mathrm{k}}} \cdot \dot{\tilde{\varepsilon}}_{\mathrm{k}} + \frac{\partial s}{\partial a}\dot{a}\right). \tag{A73}$$

Using the definition of the heat capacity at a constant deformation from [48],

$$c_{\mathrm{p}} = \Theta\frac{\partial s}{\partial \Theta}, \tag{A74}$$

the heat conduction equation can be written as

$$c_{\mathrm{p}}\dot{\Theta} = -\frac{1}{\rho_{\mathrm{R}}}\mathrm{Div}\,\vec{q}_R + \omega + r. \tag{A75}$$

A common approach for the specific heat capacity, see [54,55,85,86], is

$$c_{\mathrm{p}} \approx \Theta\frac{\partial^2 \psi_\Theta}{\partial \Theta^2}. \tag{A76}$$

The experimental results in [33] show a linear behavior of the specific heat capacity in the application range of the alloy. Thus, the expression proposed by [65] is chosen for the thermal part of the free energy ψ_Θ, which allows to obtain a linear dependence of the specific heat capacity with the temperature.

Moreover, a constitutive equation for the heat flux has to be found. Fourier's law provides an expression for the heat flux in the current configuration

$$\vec{q} = -\kappa_\Theta \mathrm{grad}\,\Theta. \tag{A77}$$

Using the relations $\vec{q}_R = (\det \mathbf{F})\mathbf{F}^{-1}\vec{q}$, and $\mathrm{grad}\,\Theta = \mathbf{F}^{-\mathrm{T}}\mathrm{Grad}\,\Theta$ one obtains

$$\vec{q}_R = -\boldsymbol{\kappa}_\Theta^{\mathrm{R}}\mathrm{Grad}\,\Theta = -\kappa_\Theta(\det \mathbf{F})\mathbf{C}^{-1}\mathrm{Grad}\,\Theta. \tag{A78}$$

The thermal conductivity of the material is represented by the second order tensor $\boldsymbol{\kappa}_{\Theta}^{\mathrm{R}}$.

References

1. Zinc Die Casting Alloys—Mechanical Properties. The International Zinc Association. 2018. Available online: https://www.zinc.org (accessed on 1 April 2018).
2. Leis, W.; Kallien, L.H. Ageing of Zink Alloys. *Int. Foundry Res.* **2011**, *64*, 2–23.
3. Martinez Page, M.A.; Hartmann, S. Experimental characterization, material modeling, identification and finite element simulation of the thermo-mechanical behavior of a zinc die-casting alloy. *Int. J. Plast.* **2018**, *101*, 74–105. [CrossRef]
4. Martinez Page, M.; Hartmann, S. Modeling of aging effects in a zinc die casting alloy. *Tech. Mech.* **2018**, *38*, 55–72.
5. Gebhard, E. Die Zinkecke des Dreistoffsystems Zink-Aluminium-Kupfer. *Z. Met.* **1940**, *32*, 78–85. [CrossRef]
6. Gebhard, E. Über den β-Zerfall in aluminiumhaltigen Zinklegierungen und den Einfluss kleiner Beimengungen auf die Zerfallsgeschwindigkeit. *Z. Met.* **1941**, *33*, 328–332.
7. Gebhard, E. Über den Aufbau und die Volumenänderung der Zink-Kupfer-Aluminium-Legierungen. *Z. Met.* **1942**, *34*, 208–215.
8. Johnen, H. *Zink-Taschenbuch*, 3rd ed.; Metall-Verlag: Berlin/Heidelberg, Germany, 1981.
9. Murray, J. The Al-Zn (Aluminium-Zinc) system. *B Alloy Phase Diagrams* **1983**, *4*, 55–73. [CrossRef]
10. Hänsel, G. Zinklegierungen; Zusammensetzung und Eigenschaften. *Metall* **1988**, *42*, 871–874.
11. Zhu, Y.; Man, H.; Lee, W. Exothermic reaction in eutectoid Zn–Al based alloys. *Mater. Sci. Eng. A* **1999**, *268*, 147–153. [CrossRef]
12. Zhu, Y. Phase transformations of eutectoid Zn-Al alloys. *J. Mater. Sci.* **2001**, *36*, 3973–3980. [CrossRef]
13. Zhu, Y. General rule of phase decomposition in Zn-Al based alloys (II)— On effects of external stresses on phase transformations—. *Mater. Trans.* **2004**, *45*, 3083–3097. [CrossRef]
14. Zhu, Y.; Hinojosa, J.; Yue, T.; Lee, W. Structural evolution in a continuously cast eutectoid Zn–Al-based alloy. *Mater. Charact.* **2002**, *48*, 315–322. [CrossRef]
15. Zhu, Y.; Lee, W.; To, S. Ageing characteristics of Zn-Al based alloy ($ZnAl_7Cu_3$). *J. Mater. Sci.* **2003**, *38*, 1945–1952. [CrossRef]
16. Zhu, Y.; Man, H.; Dorantes-Rosales, H.; Lee, W. Ageing characteristics of furnace cooled eutectoid Zn-Al based alloys. *J. Mater. Sci.* **2003**, *38*, 2925–2934. [CrossRef]
17. Jareño, E.D.; Castro, M.J.; Maldonado, S.I.; Hernández, F.A. The effects of Cu and cooling rate on the fraction and distribution of epsilon phase in Zn-4Al-(3-5.6)Cu alloys. *J. Alloys Compd.* **2010**, *490*, 524–530. [CrossRef]
18. Liu, Y.; Li, H.y.; Jiang, H.f.; Lu, X.c. Effects of heat treatment on microstructure and mechanical properties of ZA27 alloy. *Trans. Nonferrous Met. Soc. China* **2013**, *23*, 642–649. [CrossRef]
19. Savaskan, T.; Pasa Hekimoglu, A. Microstructure and mechanical properties of Zn-15Al-based ternary and quaternary alloys. *Mater. Sci. Eng. A* **2014**, *603*, 52–57. [CrossRef]
20. Pola, A.; Gelfi, M.; La Vecchia, G.M.; Montesano, L. On the aging of a hyper-eutectic Zn-Al alloy. *La Metall. Ital.* **2015**, *4*, 37–41.
21. Wu, Z.; Sandlöbes, S.; Wu, L.; Hu, W.; Korte-Kerzel, S. Mechanical behaviour of Zn–Al–Cu–Mg alloys: Deformation mechanisms of as-cast microstructures. *Mater. Sci. Eng.* **2016**, *651*, 675–687. [CrossRef]
22. Führ, L.; Ludwig, G.A.; Martins, M.; Vecchia, F.; Rieder, E.; Malfatti, C.; Oliveira, C. Effects of Mould Temperature in Squeeze Casting of Zamak 5. *Mater. Sci. For.* **2014**, *775*, 729–732. [CrossRef]
23. Cao, L.; Liao, D.; Sun, F.; Chen, T.; Teng, Z.; Tang, Y. Prediction of gas entrapment defects during zinc alloy high-pressure die casting based on gas-liquid multiphase flow model. *Int. J. Adv. Manuf. Technol.* **2018**, *94*, 807–815. [CrossRef]
24. Zhu, Y.H.; Orozco, E. Effects of tensile stress on microstructural change of eutectoid Zn-Al alloy. *Metall. Mater. Trans. A* **1995**, *26*, 2611–2615. [CrossRef]
25. Zhang, J.; Yu, Q.; Jiang, Y.; Li, Q. An experimental study of cyclic deformation of extruded AZ61A magnesium alloy. *Int. J. Plast.* **2011**, *27*, 768–787. [CrossRef]
26. McDowell, D.L. A nonlinear kinematic hardening theory for cyclic thermoplasticity and thermoviscoplasticity. *Int. J. Plast.* **1992**, *8*, 695–728. [CrossRef]
27. Rusinek, A.; Rodriguez-Martinez, J.A.; Arias, A. A thermo-viscoplastic constitutive model for FCC metals with application to OFHC copper. *Int. J. Mech. Sci.* **2010**, *52*, 120–135. [CrossRef]
28. Li, X.; Guo, G.; Xiao, J.; Song, N.; Li, D. Constitutive modeling and the effects of strain-rate and temperature on the formability of Ti-6Al-4V alloy sheet. *Mater. Des.* **2014**, *55*, 325–334. [CrossRef]
29. Lin, Y.C.; Chen, X.M.; Wen, D.X.; Chen, M.S. A novel unified dislocation density-based model for hot deformation behavior of a nickel-based superalloy under dynamic recrystallization conditions. *Appl. Phys. A* **2016**, *122*, 805. [CrossRef]
30. Martinez Page, M.A.; Ruf, M.; Hartmann, S. Numerical modeling of the thickness dependence of zinc die-cast materials. *Comput. Mech.* **2018**, *62*, 655–667. [CrossRef]
31. Krempl, E. Viscoplasticity based on total strain. The modelling of creep with special considerations on initial strain and aging. *J. Eng. Mater. Technol.* **1979**, *101*, 380–386. [CrossRef]
32. Chaboche, J. A review of some plasticity and viscoplasticity constitutive theories. *Int. J. Plast.* **2008**, *24*, 1642–1693. [CrossRef]
33. Martinez Page, M.A.; Weidenfeller, B.; Hartmann, S. Influence of temperature and aging on the thermal diffusivity, thermal conductivity and heat capacity of a zinc die casting alloy. *J. Alloys Compd.* **2019**, *786*, 1060–1067. [CrossRef]
34. Johlitz, M.; Lion, A. Chemo-thermomechanical ageing of elastomers based on multiphase continuum mechanics. *Contin. Mech. Thermodyn.* **2013**, *25*, 605–624. [CrossRef]

35. Marquis, D.; Lemaitre, J. Constitutive equations for the coupling between elasto-plasticity damage and aging. *Rev. Phys. Appliquée* **1988**, *23*, 615–624. [CrossRef]
36. Lemaitre, J.; Chaboche, J.L. *Mechanics of Solid Materials*; Cambridge University Press: Cambridge, UK, 1990.
37. Lion, A.; Johlitz, M. On the representation of chemical ageing of rubber in continuum mechanics. *Int. J. Solids Struct.* **2012**, *49*, 1227–1240. [CrossRef]
38. Johlitz, M. On the Representation of Ageing Phenomena. *J. Adhes.* **2012**, *88*, 620–648. [CrossRef]
39. Johlitz, M.; Diercks, N.; Lion, A. Thermo-oxidative ageing of elastomers: A modelling approach based on a finite strain theory. *Int. J. Plast.* **2014**, *63*, 138–151. [CrossRef]
40. Dippel, B.; Johlitz, M.; Lion, A. Ageing of polymer bonds: A coupled chemomechanical modelling approach. *Contin. Mech. Thermodyn.* **2014**, *26*, 247–257. [CrossRef]
41. Marquis, D.; Costa Mattos, H. Modeling of plasticity and aging as coupled phenomena. *Int. J. Plast.* **1991**, *7*, 865–877. [CrossRef]
42. Diebels, S.; Geringer, A. Modelling Inhomogeneous Mechanical Properties in Adhesive Bonds. *J. Adhes.* **2012**, *88*, 924–940. [CrossRef]
43. Meschke, G. Consideration of aging of shotcrete in the context of a 3D viscoplastic material model. *Int. J. Numer. Methods Eng.* **1996**, *39*, 3123–3143. [CrossRef]
44. Bazant, Z.P.; Huet, C. Thermodynamic functions for ageing viscoelasicity: Integral form wihout internal variables. *Int. J. Solids Struct.* **1999**, *36*, 3993–4016. [CrossRef]
45. Carol, I.; Bazant, Z. Viscoplasticity with aging caused by solidification of nonaging constituent. *J. Eng. Mech.* **1993**, *119*, 2252–2269. [CrossRef]
46. Lubliner, J. *Plasticity Theory*; Macmillan Publishing Company: New York, NY, USA, 1990.
47. Lubarda, V.A. *Elastoplasticity Theory*; CRC Press: Boca Raton, FL, USA, 2001.
48. Haupt, P. *Continuum Mechanics and Theory of Materials*, 2nd ed.; Springer: Berlin/Heidelberg, Germany, 2002.
49. Lion, A. Constitutive modelling in finite thermoviscoplasticity: A physical approach based on nonlinear rheological models. *Int. J. Plast.* **2000**, *16*, 469–494. [CrossRef]
50. Hartmann, S. *Comparison of the Multiplicative Decompositions* $\mathbf{F} = \mathbf{F}_\Theta \mathbf{F}_m$ *and* $\mathbf{F} = \mathbf{F}_m \mathbf{F}_\Theta$ *in Finite Strain Thermo-Elasticity*; Technical Report Series Fac3-12-01; Faculty of Mathematics/Computer Sciences and Mechanical Engineering, Clausthal University of Technology (Germany): Clausthal-Zellerfeld, Germany, 2012.
51. Miehe, C. *Zur Numerischen Behandlung Thermomechanischer Prozesse*; Report No. F88/6; Institut für Baumechanik und Numerische Mechanik, University of Hannover: Hannover, Germany, 1988.
52. Lion, A. *Thermomechanik von Elastomeren. Experimente und Materialtheorie*; Report No. 1/2000; Habilitation, Institute of Mechanics, University of Kassel: Kassel, Germany, 2000.
53. Reese, S. *Thermomechanische Modellierung gummiartiger Polymer-Strukturen*; Report No. F01/4; Habilitation, Institut für Baumechanik und Numerische Mechanik, Universität Hannover: Hannover, Germany, 2001.
54. Hamkar, A.W. Eine Iterationsfreie Finite-Elemente Methode im Rahmen der Finiten Thermoviskoelastizität. Report No. 1/2013. Ph.D. Thesis, Institute of Applied Mechanics, Clausthal University of Technology, Clausthal-Zellerfeld, Germany, 2013.
55. Quint, K.J. Thermomechanically Coupled Processes for Functionally Graded Materials: Experiments, Modelling, and Finite Element Analysis Using High-Order DIRK-Methods. Report No. 2/2012. Ph.D. Thesis, Institute of Applied Mechanics, Clausthal University of Technology, Clausthal-Zellerfeld, Germany, 2012.
56. Martinez Page, M.A. Thermo-Mechanical Behavior of a Zinc Die Casting Alloy Considering Natural Aging. Report No. 1/2019. Ph.D. Thesis, Institute of Applied Mechanics, Clausthal University of Technology, Clausthal-Zellerfeld, Germany, 2019.
57. Kallien, L.H.; Busse, M. *Ursachen und Möglichkeiten zur Minimierung der Alterungsvorgänge bei Zinkdruckgusslegierungen;* Technical Report; Hochschule Aalen and IFAM Bremen: Aalen, Germany, 2009.
58. Krempl, E.; McMahon, J.; Yao, D. Viscoplasticity based on overstress with a differential growth law for the equilibrium stress. *Mech. Mater.* **1986**, *5*, 35–48. [CrossRef]
59. Krempl, E. Models of viscoplasticity - some comments on equilibrium (back) stress and drag stress. *Acta Mech.* **1987**, *69*, 25–42. [CrossRef]
60. Stitcti, M.; Krempl, E. A stability analysis of the uniaxial viscoplasticity theory based on overstress. *Comput. Mech.* **1989**, *4*, 401–408.
61. Haupt, P.; Lion, A. Experimental identification and mathematical modelling of viscoplastic material behavior. *J. Contin. Mech. Thermodyn.* **1995**, *7*, 73–96. [CrossRef]
62. Flory, P.J. Thermodynamic relations for high elastic materials. *Trans. Faraday Soc.* **1961**, *57*, 829–838. [CrossRef]
63. Tsakmakis, C.; Willuweit, A. A comparative study of kinematic hardening rules at finite deformations. *Int. J. Non-Linear Mech.* **2004**, *39*, 539–554. [CrossRef]
64. Hartmann, S.; Neff, P. Polyconvexity of generalized polynomial-type hyperelastic strain energy functions for near-incompressibility. *Int. J. Solids Struct.* **2003**, *40*, 2767–2791. [CrossRef]
65. Heimes, T. *Finite Thermoinelastizität*; Number 709 in Fortschrittsberichte, Reihe 5, Grund- und Werkstoffe/Kunststoffe; VDI-Verlag: Düsseldorf, Germany, 2005.
66. Deschamps, A.; Livet, F.; Bréchet, Y. Influence of predeformation on ageing in an Al–Zn–Mg alloy—I. Microstructure evolution and mechanical properties. *Acta Mater.* **1998**, *47*, 281–292. [CrossRef]

67. Cerri, E.; Leo, P. Influence of severe plastic deformation on aging of Al–Mg–Si alloys. *Mater. Sci. Eng. A* **2005**, *410–411*, 226–229. [CrossRef]
68. Lion, A.; Dippel, B.; Liebl, C. Thermomechanical material modelling based on a hybrid free energy density depending on pressure, isochoric deformation and temperature. *Int. J. Solids Struct.* **2014**, *51*, 729–739. [CrossRef]
69. Krämer, S.; Rothe, S.; Hartmann, S. Homogeneous stress-strain states computed by 3D-stress algorithms of FE-codes: Application to material parameter identification. *Eng. Comput.* **2015**, *31*, 141–159. [CrossRef]
70. Beck, J.V.; Arnold, K.J. *Parameter Estimation in Engineering and Science*; John Wiley & Sons: New York, NY, USA, 1977.
71. Schiesser, W.E. *The Numerical Method of Lines: Integration of Partial Differential Equations*; Academic Press: Cambridge, MA, USA, 1991.
72. Hartmann, S.; Rothe, S. A Rigorous Application of the Method of Vertical Lines to Coupled Systems in Finite Element Analysis. In *Recent Developments in the Numerics of Nonlinear Hyperbolic Conservation Laws*; Notes on Numerical Fluid Mechanics and Multidisciplinary Design; Ansorge, R., Bijl, H., Meister, A., Sonar, T., Eds.; Springer: Berlin/Heidelberg, Germany, 2013; Volume 120, pp. 161–175.
73. Netz, T.; Hamkar, A.W.; Hartmann, S. High-order quasi-static finite element computations in space and time with application to finite strain viscoelasticity. *Comput. Math. Appl.* **2013**, *66*, 441–459. [CrossRef]
74. Rothe, S.; Erbts, P.; Düster, A.; Hartmann, S. Monolithic and partitioned coupling schemes for thermo-viscoplasticity. *Comput. Methods Appl. Mech. Eng.* **2015**, *293*, 375–410. [CrossRef]
75. Quint, K.J.; Hartmann, S.; Rothe, S.; Saba, N.; Steinhoff, K. Experimental validation of high-order time-integration for non-linear heat transfer problems. *Comput. Mech.* **2011**, *48*, 81–96. [CrossRef]
76. Hartmann, S. A remark on the application of the Newton-Raphson method in non-linear finite element analysis. *Comput. Mech.* **2005**, *36*, 100–116. [CrossRef]
77. Rabbat, N.B.G.; Sangiovanni-Vincentelli, A.L.; Hsieh, H.Y. A Multilevel Newton Algorithm with Macromodeling and Latency for the Analysis of Large-Scale Nonlinear Circuits in the Time Domain. *IEEE Trans. Circuits Syst.* **1979**, *26*, 733–740. [CrossRef]
78. Korelc, J. Multi-language and Multi-environment Generation of Nonlinear Finite Element Codes. *Eng. Comput.* **2002**, *18*, 312–327. [CrossRef]
79. Korelc, J. Automation of primal and sensitivity analysis of transient coupled problems. *Comput. Mech.* **2009**, *44*, 631–649. [CrossRef]
80. Rabinowicz, E. The nature of the static and kinetic coefficients of friction. *J. Appl. Phisics* **1951**, *22*, 1373–1379. [CrossRef]
81. Dileep, P.K.; Hartmann, S.; Hua, W.; Palkowski, H.; Fischer, T.; Ziegmann, G. Parameter estimation and its influence on layered metal-composite-metal plates. *Acta Mech.* **2022**, *233*, 2891–2929. [CrossRef]
82. Dileep, P.K.; Hartmann, S.; Javadi, M.; Palkowski, H.; Fischer, T.; Ziegmann, G. Uncertainty estimation using Gaussian error propagation in metal forming process simulation. *PAMM Proc. Appl. Math. Mech.* **2022**, *22*, e202200073. [CrossRef]
83. Oberkampf, W.L.; Trucano, T.G. Verification and validation in computational fluid dynamics. *Prog. Aerosp. Sci.* **2002**, *38*, 209–272. [CrossRef]
84. Hartmann, S. *Finite-Elemente Berechnung Inelastischer Kontinua. Interpretation als Algebro-Differentialgleichungssysteme*; Report No. 1/2003; Habilitation, University of Kassel, Institute of Mechanics: Kassel, Germany, 2003.
85. Jansohn, W. *Formulierung und Integration von Stoffgesetzen zur Berechnung großer Deformationen in der Thermoplastizität und -Viskoplastizität*; Technical Report FZKA 6002; Forschungszentrum Karlsruhe: Karlsruhe Germany, 1997.
86. Rothe, S. Electro-Thermo-Mechanical Modeling of Field Assisted Sintering Technology: Experiments, Constitutive Modeling and Finite Element Analysis. Report No. 1/2015. Ph.D. Thesis, Institute of Applied Mechanics, Clausthal University of Technology, Clausthal-Zellerfeld, Germany, 2015.

Disclaimer/Publisher's Note: The statements, opinions and data contained in all publications are solely those of the individual author(s) and contributor(s) and not of MDPI and/or the editor(s). MDPI and/or the editor(s) disclaim responsibility for any injury to people or property resulting from any ideas, methods, instructions or products referred to in the content.